Title
Achieving Novel Magnetic States in Perovskite Oxides through Heteroepitaxy

Author
Mehta, Virat

Publication Date
2012

Peer reviewed|Thesis/dissertation

Achieving Novel Magnetic States in Perovskite Oxides through Heteroepitaxy
A Dissertation submitted to the Faculty of the Graduate School of the University of California, Berkeley

Virat Vasav Mehta

In partial fulfillment of the requirements for the degree of
Doctor of Philosophy in

The College of Engineering-
Department of Materials Science and Engineering

And a Designated Emphasis
In

Nanoscale Science and Engineering

In the Graduate Division of the
University of California, Berkeley

Committee in charge:
Professor Yuri Suzuki, Chair
Professor Oscar Dubon
Professor Joel Moore

Spring 2012

Achieving Novel Magnetic States in Perovskite Oxides through Heteroepitaxy

Abstract
Achieving Novel Magnetic States in Perovskite Oxides Through Heteroepitaxy

By Virat Vasav Mehta

Doctor of Philosophy in
The College of Engineering-
Department of Materials Science and Engineering
And a Designated Emphasis in
Nanoscale Science and Engineering

University of California, Berkeley
Professor Yuri Suzuki, Chair

This dissertation is focused on controlling the spin state and long-range magnetic order in cobaltites by heteroepitaxial thin-film growth. I explore the growth of two different cobaltite materials, $LaCoO_3$ and $PrCoO_3$, on lattice-mismatched substrates to determine the role of epitaxial strain in giving rise to long-range magnetic order. This magnetic order is not found in the bulk cobaltite material and warrants the detailed investigations carried out in this work. I investigate changes in structure and stoichiometry that influence the electronic structure and the long-range magnetic order in these materials.

In the $LaCoO_3$ system, I explore the changes in structure in the films under tensile strain and compressive strain by growth on $SrTiO_3$, $LaSrAlTaO_3$, and $LaAlO_3$ substrates and film growth between 8 nm -133 nm thick. Substrate-dependent oxygen vacancy ordering in the films is found using microstructural characterization, presumably related to the amount of stress in each of the films. By carrying out a study of the effects on the film structure from the oxygen growth pressure, I find an overall increase in the out-of-plane lattice parameter with lower oxygen growth pressures.

These structural and stoichiometry changes in the $LaCoO_3$ films to trends appear to be related to the stabilization of long-range magnetic order. Highest moment is found in the films in tension (which also have the most defects) on $SrTiO_3$ and $LaSrAlTaO_3$ substrates and the lowest moment is found in films in compression on $LaAlO_3$. Element-specific X-ray absorption techniques reveal contributions from Co in different spin and valence states. I show how strain affects the electronic structure and distribution of these different states and relate these observations to trends observed in the magnetism. Strained films in tension have the highest amount of high spin Co^{3+} and high spin Co^{2+}, while relaxed films appear to have mostly low spin Co^{3+} at 25 K. I present some scenarios to explain how these different Co ions combine to give rise to long-range ferromagnetic order in $LaCoO_3$ films.

In the $PrCoO_3$ system, I explore whether long-range magnetic order can be observed using heteroepitaxial synthesis similar to the efforts in the $LaCoO_3$ thin film system despite $PrCoO_3$ having a more stable low spin state configuration in the bulk. The PCO films in tension are ferromagnetic, similar to the $LaCoO_3$ system. Thus, epitaxial strain dominates the effects of chemical pressure which stabilize a low spin state. The strained films have more high spin Co^{3+}. The implication of Co sublattice ordering on the ordering of the Pr sublattice is explored using X-ray magnetic circular dichroism. A rare ordering of the Pr ions anti-parallel to the orientation of the moments on the Co sublattice appears to occur in this system. These studies demonstrate the power of heteroepitaxial synthesis to give rise to new magnetic functionality in perovskite oxide systems.

For Kanubhai, Savitaben, Madhukantbhai, and Kavitaben

Table of Contents

Acknowledgments

First and foremost, I would like to thank my advisor, Professor Yuri Suzuki, for making the work in this dissertation possible. Without the incredible number of tools and resources she has made available to me in the lab, none of this work could have been accomplished. She has also provided access to an esteemed network of collaborators that were easy to reach out to in order to help answer some of the more pressing questions in this research and push new projects forward. She has created a generous space for independent exploration of new materials and exciting new research ideas in her laboratory, while still providing a sense of direction and encouragement to the aspiring researcher.

I would also like to thank the U.S. Department of Energy for graciously funding my work throughout my tenure at Berkeley. Aside from a nanotech researcher fellowship I received in my first two terms here, the funding provided by the U.S. Department of Energy under the Office of Basic Energy Sciences, Materials Sciences Division, and Scientific User Facilities Division have been critical to the completion of this work.

I would also like to show my appreciation to the members of my dissertation committee for their patience and diligence in providing me with valuable timely guidance with this dissertation.

I am also grateful to the numerous collaborators I have had the pleasure of working with throughout my years at Berkeley. Even in the instances that didn't result in a publication, the techniques I learned and the various approaches I encountered have help to make me more well-rounded and adept at experimental work. I especially would like to the thank: Dr. Jeff Kortright at Lawrence Berkeley National Laboratory and Dr. Frank (Bud) Bridges at UC Santa Cruz for their collaborations that taught me a great deal about beamline science and the necessary care needed when analyzing beamline data, Dr. Elke Arneholz at the Advanced Light Source who has worked with me throughout the years and always been supportive of our lab, Dr. Maria Varela who has taught me a great deal about the values and limits of electron microscopy, and Professor Chris Leighton at the University of Minnesota who has served as a knowledgeable resource on all science related to the cobaltites.

I would also like to the many former lab members that have molded my habits and taught me the best ways to approach research. I especially want to thank Rajesh Chopdekar and Marco Liberati who served as mentors and role-models throughout my graduate experience. They taught me the importance of being unabashed when it comes to asking questions and to take a participatory role in the operation and upkeep of laboratory equipment. The hands on approach to research that they pushed is incredibly valuable for an experimentalist and I appreciate their efforts to try to develop these habits in me. Thanks to Joanna Bettinger for teaching me to put the priorities of the lab and our labmates first. To Brittany Nelson-Cheeseman for her infectious enthusiasm to new scientific ideas and for pushing me to talk to more scientists that resulted in new collaborations. To Franklin Wong also for his enthusiasm and for always being a positive force in the lab. He is always ready to discuss scientific ideas and help hash out new solutions to open questions. He always pushes those around him to excel.

I also am grateful for the current and future lab members I have had the pleasure of working with during this work. Special thanks to Jodi Iwata who has greatly enriched the experience. Her enthusiasm and humility have always made the lab a welcoming place to do research. Thanks also to Alex Grutter for his cheery outlook, and to Urusa Alaan for her industriousness and humor. Thanks to all of you and good luck!

I also would like to thank Rachel Rose for her patience and friendship during my graduate career and for her help with finding grammatical errors in this dissertation. She was always there to lift my spirits, keep me motivated, and celebrate my successes. I am eternally grateful to my brothers, Vishal and Vishes, with whom I have had the chance to engage in deeply philosophical and challenging discussions throughout this process. They have always been an inspiring force in changing my outlook when it was most needed. I also extend thanks to all my family members who have been incredibly supportive, especially to my family in California who have always provided me with a home away from home in case I were to need anything.

Finally, I would like to thank my mother and father for their continual support and belief in me. The ways that they have contributed to the completion of this work is beyond words. But nevertheless, I want to thank them for teaching me the value of education and perseverance, and for always reminding me that “where there is a will, there is a way.”

Chapter 1: Designing new routes towards novel magnetic functionality

Abstract

In this chapter the driving forces behind this body of research are presented. A general background regarding the physics of complex perovskite oxides is given to establish their relevance to the investigation of novel functionality. Specifically, we discuss the concepts of spin states and crystal field splitting in transition metal oxides. The use of thin film growth techniques to study these phenomena is also introduced. Background regarding cobaltite oxides is given to show the various routes by which we can control the possible spin states in this material. At the end of this chapter, an overview of the topics to be covered in the remaining chapters is given.

Chapter 1: Designing new routes towards novel magnetic functionality

1.1. Research in multifunctional spintronic materials

In our current information and computer technology fueled era, there is a growing demand for new materials that exhibit a versatile mix of magnetic, electronic, and structural properties. The current technologies, in trying to satisfy Moore's Law, are designed to approach fundamental nanoscale size limits in order to meet the increasing demand for high-capacity, fast-paced data storage and processing applications. The results include an increase in world-wide electricity consumption [1] and detrimental environmental impacts in the form of waste heat and resource depletion. To decrease negative environmental effects, scientists and engineers have begun to seek out new multifunctional materials able to lower power consumption while still extending the capabilities of current technology.

Spintronics [2], one highly touted avenue still in its early stages, takes advantage of multifunctional materials that exploit both the spin and charge of the electron to create new possibilities for current technology. By taking advantage of the nonvolatile electron spin to perform logic and data storage operations, we could reduce energy consumption from information technology sources. At the same time exploiting the spin to perform these operations would result in faster processing times. Many new technologies relying on spintronics are already being incorporated into current devices including giant magneto-resistance/tunneling magneto-resistance read heads, spin valves, spin transistors, sensors, MRAM, and quantum computation. However, increasing the reach of this new technology into more devices and more applications relies heavily on the development of multifunctional materials in which spin can be easily controlled via external sources such as an applied electric field, applied magnetic field, or electromagnetic radiation. From a scientific perspective, a greater understanding of the complex interactions among a material's charge, spin, and orbital degrees of freedom is fundamental to engineering new multifunctional materials and devices.

1.2. Development of novel functionality in complex oxides perovskites

The unique properties of complex oxides make them ideal candidates for the investigation and further development of multifunctionality. These materials are known to exhibit a vast array of properties including high-T_c superconductivity, colossal magneto-resistance, metal-insulator transitions, piezoelectricity, multiferroic behavior, spin-state transition, and other correlated electron phenomena that rely on the complex interactions between charge, spin, and lattice (orbitals) degrees of freedom. Many of these complex oxides have rich phase diagrams that often show that access to these various properties requires only a small amount of chemical doping, temperature change, or structural distortion. Research focusing on these systems will enhance our understanding of the complex electron-electron interactions that give rise to these properties and demonstrate

their potential use in spintronic applications [3]. In order to appreciate why these systems are ideal for studying correlated electron behavior, it is important to describe the relationship between the physical and electronic structure, as well as the relationship between the electronic structure and magnetic properties of these materials. In the upcoming sections we will give a brief description of the general properties of these complex perovskite oxides based on information gathered from a variety of sources.

1.2.1. Physical structure of perovskites

Perovskite oxides represent a class of materials characterized by the chemical formula ABO_3, where A is typically a rare-earth metal or alkaline earth metal cation, B is typically a transition metal cation, and O represents an oxygen anion (Figure 1). The structure of these materials varies, but, in general, can be characterized by an octahedron of oxygen anions surrounding the transition metal cation that collectively sit inside of a simple cubic cage of rare-earth/alkaline-earth metal cations. The result is a 12-fold coordinated A-site and 6-fold coordinated B-site, with both cations sharing their coordination with the oxygen anions. Since in most perovskite oxides the interesting electronic interactions take place between the oxygen octahedral cage and the transition metal, it may be more useful to think of the perovskite structure as a network of corner-sharing octahedral complexes.

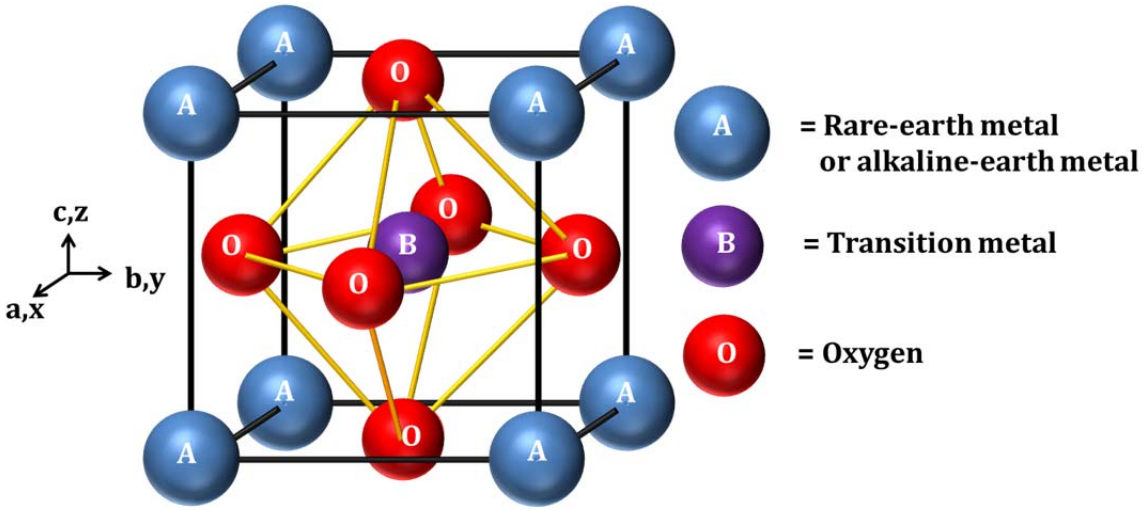

Figure 1 Cubic perovskite unit cell showing positions of A-site, B-site, and oxygen ions in the lattice. A-site corresponds to the rare-earth metal or alkaline earth metal ion. The B-site corresponds to a transition metal cation. (*Image courtesy A. Grutter*)

Perovskites are known to sustain large changes from the inclusion of different elemental species by changing bond-lengths or octahedral tilts within the crystal. Deviations of the perovskite structure from the cubic case (t =1) are easily calculated by the tolerance factor [6, 7], $t \equiv \frac{(A-O)}{\sqrt{2}(B-O)}$, where (A-O) and (B-O) refer to

the sum of the A-site/B-site cation and oxygen anion radii. Typically for $t > 1$ we find hexagonal perovskites, which we will not consider here. For $t < 1$ the structure adjusts by decreasing the B-O-B bond angle from 180°. This is seen from the coordinated tilting of the corner-sharing octahedra in a lattice. The symmetry of the lattice may change based on the cubic axis about which the octahedra rotate. For example, for rotations about [111] axis we get rhombohedral symmetry, and for rotations about [110] we get orthorhombic symmetry. The rotation is greater for smaller values of *t*. Exploring how the electronic structure may change for various lattice changes is one of the goals of this dissertation, and so it is necessary to provide a qualitative description of the electronic structure of perovskites.

1.2.2. Electronic structure of perovskites

The bonding in these oxides is best thought of as ionic, although the bonds between the cations and the oxygen anions often adopt some covalent character showing strong hybridization between cation and anion orbitals. Thus, for a qualitative understanding of the perovskite electronic structure closest to the Fermi level (valence and conduction band energy levels), it is useful to think about the cations and anions in this system in terms of a molecular orbital picture in the linear combination of atomic orbitals approximation [8, 9, 10]. This approach incorporates valence bond theory and group theory considerations and provides an intuitive understanding of how the electronic structure is affected by changes in symmetry associated with distortions and coordinated rotations of these transition metal-oxygen octahedra.

In this ionic framework we consider the bonding and anti-bonding interactions between *s*-, *p*-, and *d*- orbitals of the A-site or B-site atomic orbitals and the oxygen atomic orbitals. Figure 2 shows examples of the stronger σ-bonding and weaker π-bonding interactions that can take place between interacting orbitals. We have also shown examples of non-bonding interactions which do not contribute energy levels to the overall electronic structure. The lobes of the atomic orbital wavefunctions are drawn with phases (indicated by "+" and "–") appropriate for the angular momentum of each orbital (s, p, d). When two overlapping lobes are in phase the result is constructive interference of the atomic orbital wavefunctions and a bonding interaction. When these phases are opposite the result is destructive interference of the interacting orbitals and an antibonding interaction. The nonbonding examples show the interactions that are symmetry-forbidden, and result in no net interference or bonding interaction.

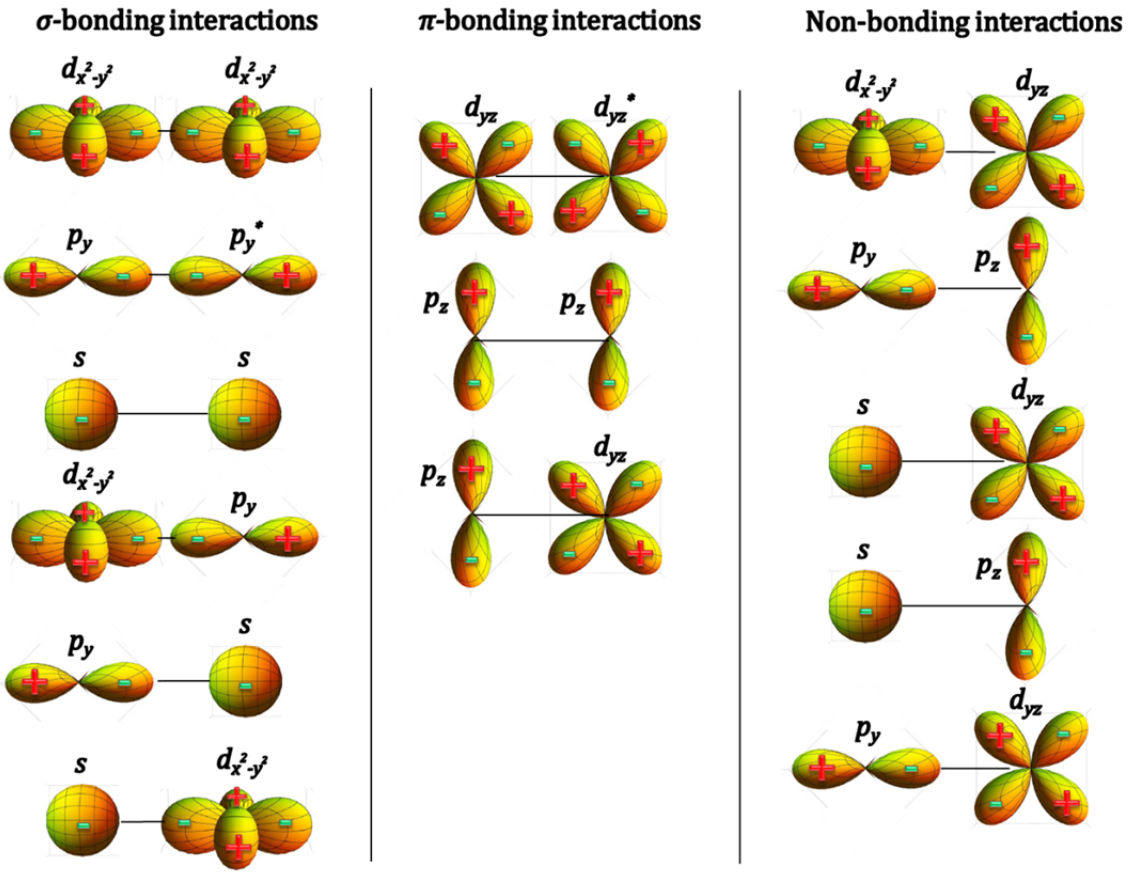

Figure 2 Schematic showing orbital interactions for possible σ-bonding, π-bonding, and non-bonding interactions between *s*-, *p*-, and *d*-orbitals in a molecular orbital description that uses the linear combination of atomic orbitals.

Fortunately, the A-site *4f* orbitals (if they are occupied) are highly localized and are typically not heavily involved in the bonding interaction with the oxygen anion, so we have not considered them here. Instead the *s*- and *p*- orbitals of the cations are heavily involved in the bonding (and antibonding) interactions with the oxygen *s*- and *p*- orbitals and thus make up the low-lying (bonding orbitals) core levels of the electronic structure and the unoccupied high-lying (antibonding orbitals) levels well above the Fermi level. The weaker bonding interactions of the transition metal 3*d* orbital with the oxygen 2*s* and 2*p* orbitals are the origin for most of the electronic structure nearest to the Fermi level. Because the majority of the contribution to these states comes from the transition metal 3*d*-orbital, these states are often depicted with the same symmetry as the transition metal 3*d*-orbitals and are labeled as the two-fold degenerate e_g^* and three-fold degenerate t_{2g} levels. The e_g^* levels are made up of the more strongly interacting σ-antibonding molecular orbitals and the t_{2g} are made up of the weaker π- antibonding molecular orbitals. The energy spacing between these two sets of degenerate levels is called the crystal-field splitting energy (Δ_{CF}).

Using these considerations, we can carefully construct the molecular orbitals that make up the perovskite oxide. By only considering the transition metal atomic orbitals in σ- bonding to the O_6 octahedra which form a set of molecular orbitals, Burdett *et al.* [11] has constructed an energy level diagram that contains most of the relevant details for the perovskite electronic structure. A more precise depiction might consider π- bonding interactions as well. Figure 3 shows an adaptation of this construction [11] illustrating a molecular orbital diagram for a general MO_6 cluster. The energy levels may shift up or down based on the choice of transition metal and rare-earth/alkaline-earth metal cation, which could influence the Fermi level and the relative contribution from the different elements' atomic orbitals to the molecular orbitals in the diagram.

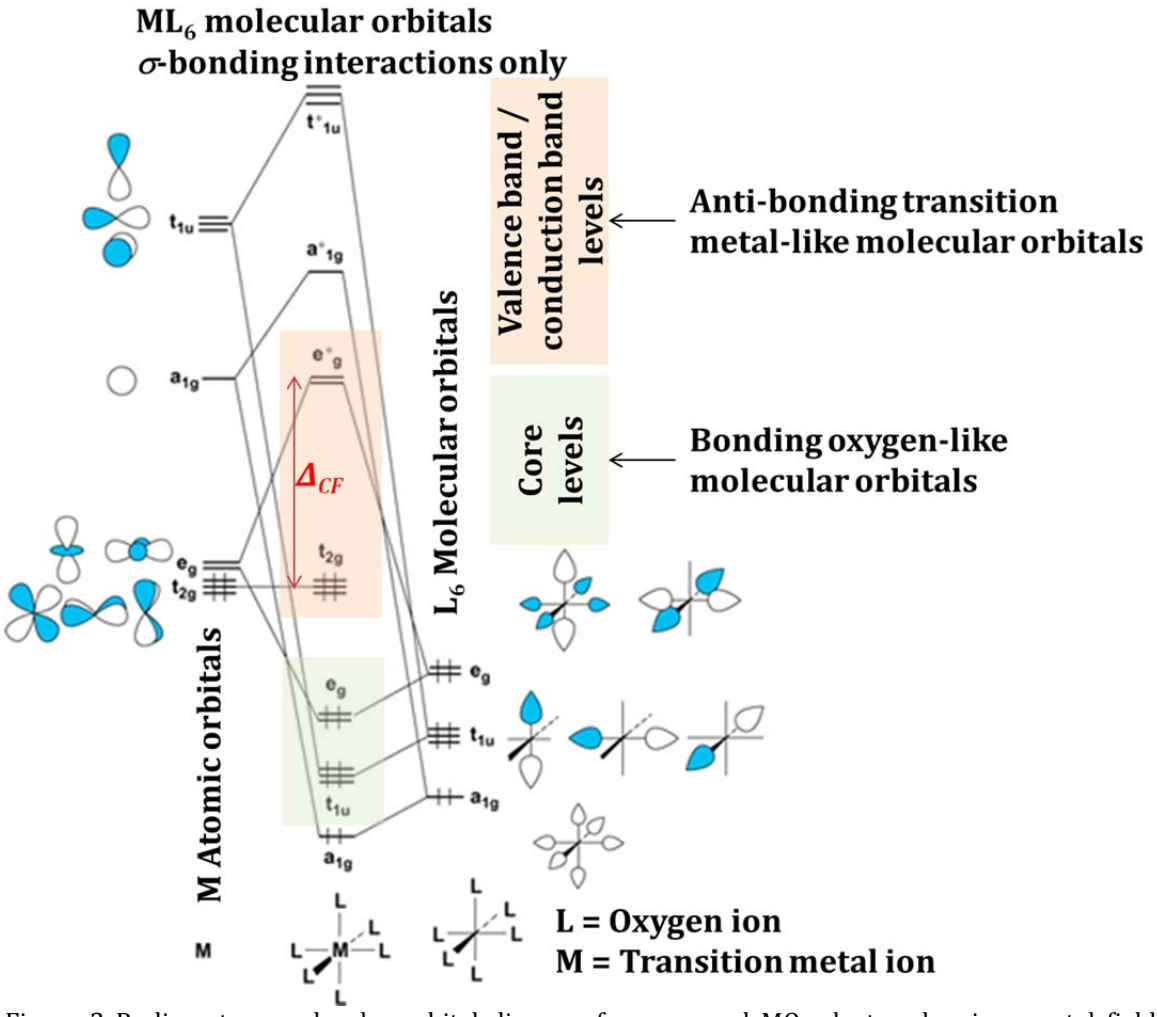

Figure 3 Rudimentary molecular orbital diagram for a general MO_6 cluster showing crystal field splitting between transition metal-like antibonding t_{2g} and e_g states (red). From [11].

Although this description portrays the perovskite electronic structure as being composed of discrete atomic-like energy levels, a real crystal lattice is better described using band theory, where the discrete levels are replaced with electronic

bands that have some energy bandwidth. However, since our description is based in the group theoretical approach, it proves useful when considering how the electronic structure is affected under changes of symmetry or bond-length from volume changes, lattice distortions, or octahedral rotations. This description helps to establish the strong link between the structure of the perovskite unit cell and the overall electronic structure.

Figure 4 shows the qualitative change in crystal field splitting energy that might occur from a fictional isotropic lattice contraction. The bond-lengths in the compressed structure are decreased and the result is an increase in the crystal field splitting. The reason for this change is explained by the change in the strength of the bonding interaction under such a compression. The transition metal orbitals pointed along the x, y, and z ($d_{x2\text{-}y2}$ and d_{z2}) directions have a much stronger bonding interaction with the oxygen anions, and as a result the e_g^* orbitals have a higher energy (become more anti-bonding). Similarly the t_{2g} orbitals also have a higher energy, though the increase is much smaller since the bonding interaction is already much weaker for these orbitals.

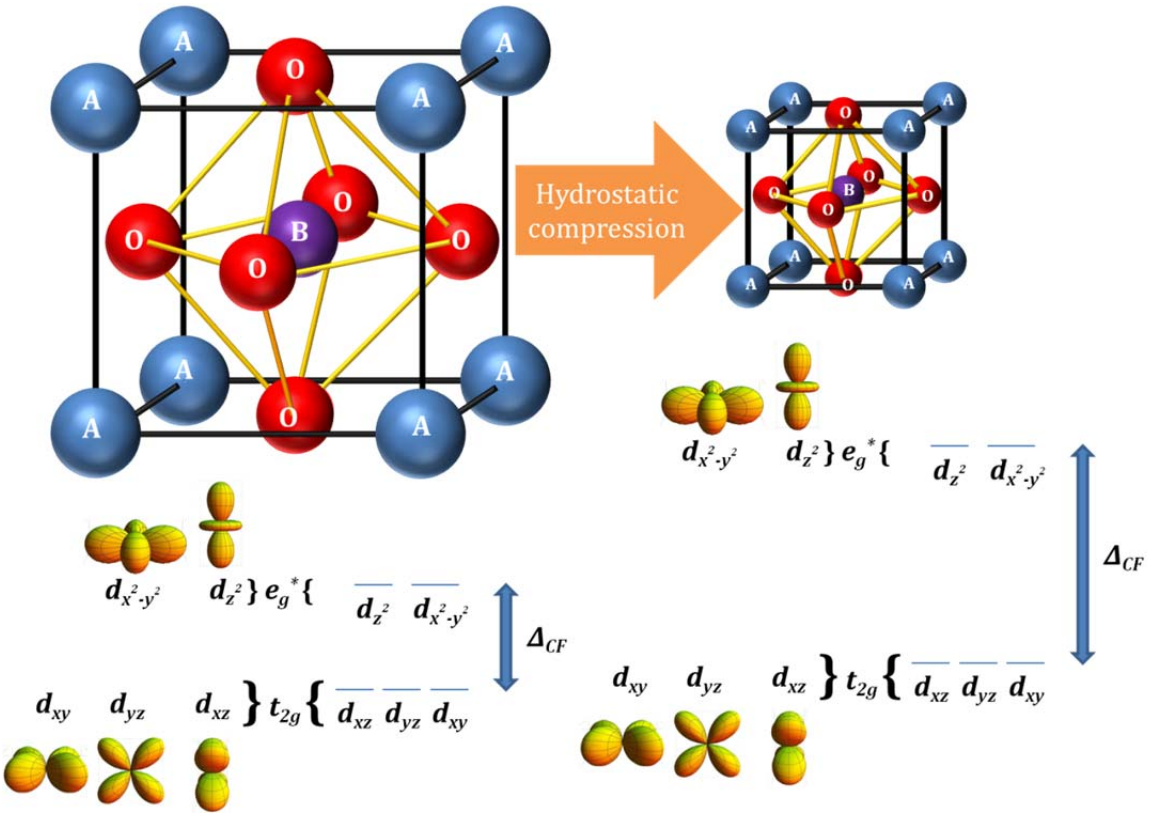

Figure 4 The effect on the electron energy levels nearest the Fermi level under the action of a hydrostatic compression on the perovskite lattice

We can continue exploring this example by considering these lattice effects in the presence of electrons occupying these energy levels. This will help illustrate the concept of spin states in transition metal oxides, which are highly relevant in this

dissertation. First, we consider the ground state electron configuration in an atomic d-orbital. We follow Hund's rules which state [12]: (i) the electron configuration (term symbol) with the lowest energy has maximum multiplicity (2S+1, total spin); (ii) Within maximum multiplicity, the electron configuration with maximum L (total angular momentum) has the lowest energy; and (iii) for atoms with a more than half-filled shell the value with a highest J (L+S) has the lowest energy. The most important of these rules is the first, which governs the Aufbau principle stating that unoccupied orbitals will be filled before occupied orbitals when filling electrons in a degenerate set of orbitals. Hence, for five degenerate *d*-orbitals, the filling of ten electrons results in S= ½, 1, 3/2, 2, 5/2, 2, 3/2, 1, ½, and then 0.

The electron filling is straightforward when all the orbitals in a shell are degenerate. However, when the transition metal is bonded to the octahedral oxygen cage, the *d*-orbital degeneracy is split by the crystal field energy into the degenerate e_g^* and t_{2g} subshells. To understand how the electrons fill this non-degenerate set of levels, we can think of the principles governing electron filling as an intra-atomic exchange (Δ_{ex}) energy cost that is paid when spins are paired on a given orbital [4]. Figure 5 shows a schematic example for the filling of six 3*d* electrons bonded in the perovskite structure. The presence of electrons in these levels creates a competition between the Δ_{ex}, which drives the alignment of all the spins in both e_g^* and t_{2g} subshells, and Δ_{CF}, which drives the filling of t_{2g} levels before filling e_g^* levels. In the figure there is an additional energy cost, $\Delta_{ex,}$ for populating spin-up electrons compared to spin-down electrons in the *d*-orbitals.

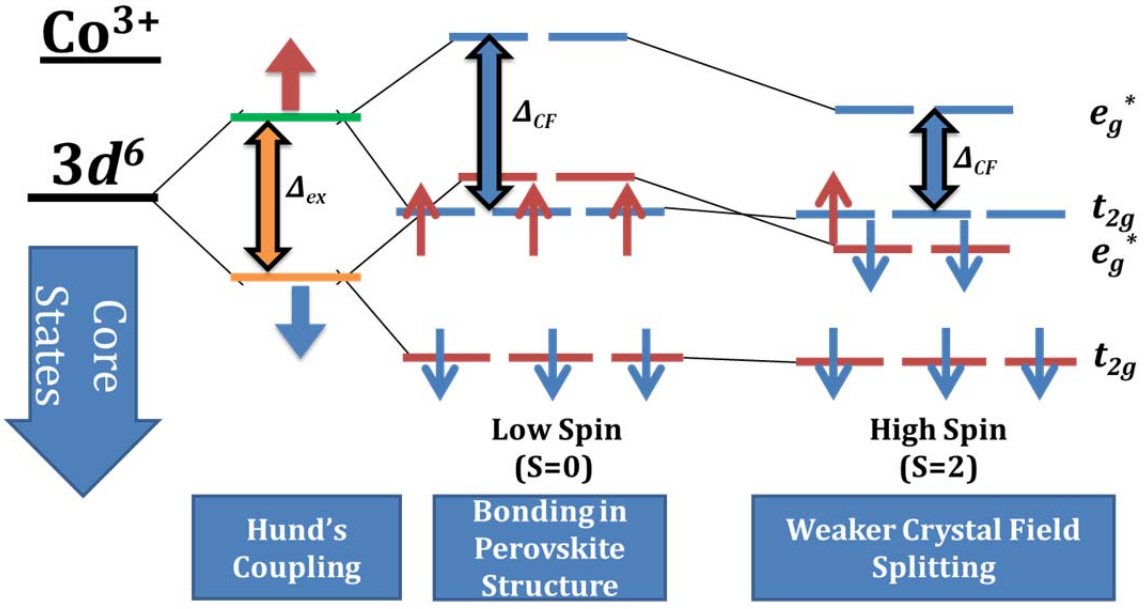

Figure 5 Schematic illustration of the electronic configuration under different crystal field splitting energies for Co^{3+} with 6 *d*-orbital electrons. Also shown is the intra-atomic exchange splitting for spin-up and spin-down levels of the electronic structure. By considering the relative strength of the crystal field and the Hund's coupling, different spin states are possible in the perovskite structure.

Now let us revisit the example of the lattice contraction described above. In this kind of lattice change, we might observe a dramatic change in the spin configuration from a high spin state to a low spin state. In the high spin state the crystal field splitting energy is lower than the driving force for Hund's coupling and so the Hund's rules are obeyed over the full *d*-orbital. For this case we follow the rules for filling used in the five-fold degenerate *d*-orbital case and get the same net spin moment on the ion as shown above. In the low spin state, the lattice contraction has increased the crystal field splitting energy such that the system rather pays the intra-atomic exchange energy (Δ_{ex}) cost and completely fills the t_{2g} shell with spin-up *and* spin-down electrons before occupying the higher e_g levels. In this configuration, the highest net moment that the ion adopts is S=3/2. Thus, based on the relative strengths of the Δ_{CF} and Δ_{ex} we can observe a large difference in the net spin moment of the ion.

From the examples above, we can see how small lattice changes might alter the electronic structure of a material. If these levels were partially filled with electrons, as they would be in most transition metal perovskites, the changes in crystal field could have profound effects on various magnetic and electronic properties of the material such as spin state and bandgap. If the pressure were applied anisotropically, it is possible that the lattice might change through a combination of changes in bond length and bond angles. To understand the changes in electronic structure under these anisotropic conditions, we would have to consider both anisotropic bond-length changes and anisotropic bond-angle changes [13]. While we can qualitatively treat anisotropic bond-length changes using similar arguments that were used in the previous example, without knowing specifically how the bond-angles and bond-lengths change we cannot conclude anything further about the electronic structure under these hypothetical anisotropic lattice changes.

1.2.3. Magnetic exchange in perovskites

The long-range magnetic order in oxides occurs through indirect exchange mechanisms such as superexchange (SE) [14] in most ionic insulators and double exchange (DE) [15] in materials that exhibit more conductive behavior. These mechanisms are called indirect (instead of *direct*) because they couple next-to-nearest neighbor cations often through an intermediary non-magnetic nearest-neighbor anion. Both superexchange and double exchange rely on an electron transfer process (real and resulting in metallicity in the case of DE; virtual and resulting in localized electrons in the case of SE) that conserves spin angular momentum and mediates the spin-spin interactions between cations carrying a net spin.

The type and strength of the magnetism that arises from superexchange are governed by the Goodenough-Kanamori [12] rules. These rules govern the spin-spin interaction between half-filled and half-filled, half-filled and filled, and half-filled and empty orbitals on next-to-nearest neighbor cations. Examples of superexchange possibilities for these cases are shown in Figure 6 between two d_{x2-y2}-orbitals and an intermediate p_y-orbital. The qualitative general principle is that the symmetry-

allowed overlapping orbitals between the cations and the intermediate anion have excited states in which an electron from one ion spends some time in the orbital of the neighboring ion, i.e. the bonds are not perfectly ionic. The electron transfer in superexchange is considered *virtual* because we consider the lowest energy excited states (the states involving electron transfer) in order to determine the ground state magnetic configuration. In each scenario of Figure 6 two excited states are shown: (a) charge transfer from the anion to the cation; (b) two charge transfers--one to the anion and one from the anion. The lowest energy excited state is (b), the one that leaves the anion filled and nonmagnetic. Hund's rules governing the net spin for each cation creates an energy penalty associated with the transfer of a spin-down electron to a cation with majority spin-up states. Also, the Pauli Exclusion Principle forbids the transfer of a spin-up electron to an orbital already occupied with a spin-up electron. Thus, as shown in case (2) in Figure 6, even between an empty cation orbital and a half-filled orbital ferromagnetic exchange is possible if the orbitals below the empty level in the cation are half-filled with spins parallel to the neighboring cation. Depending on the strength of the bonding interaction (σ or π) between the overlapping orbitals, different ferromagnetic and antiferromagnetic superexchange interactions can compete to affect the overall strength and type of magnetic interaction of the oxide. The strength is also governed by the magnitude of the net moment on the cations and the cation-anion-cation bond angle. Superexchange most often occurs in antiferromagnets and insulating ferromagnets.

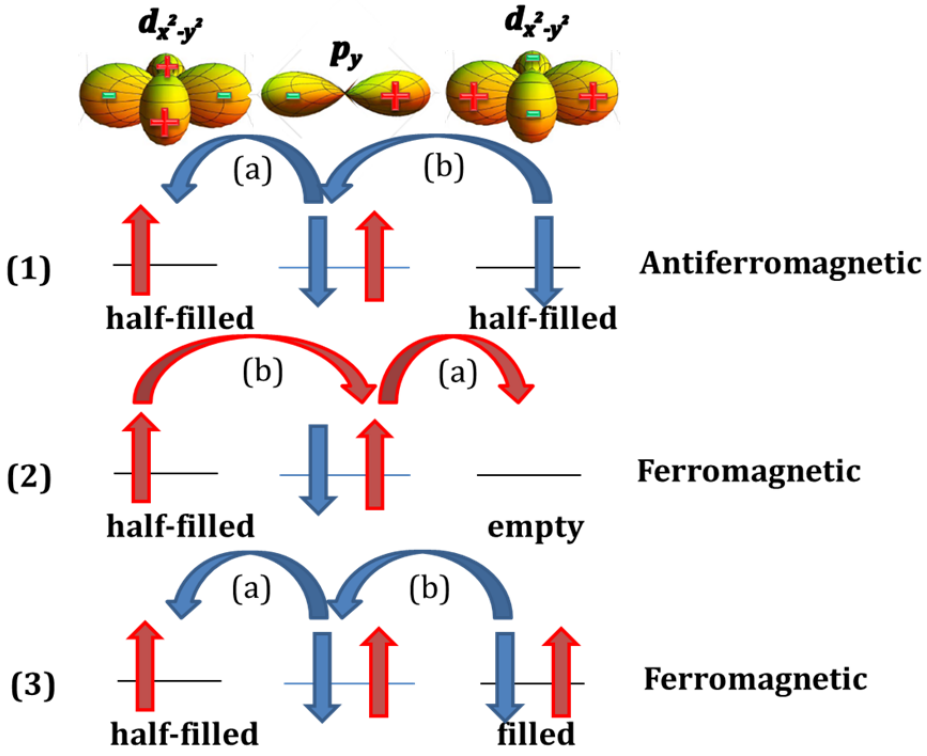

Figure 6 A few scenarios for superexchange interaction involving excited state electron transfers from transition metal d_{x2-y2} orbitals and oxygen p_y orbitals that usually result in antiferromagnetism

(1). In some scenarios (2, 3) between a partially filled orbital and an empty of filled orbital ferromagnetism can occur.

Scenarios do exist in which ferromagnetism via superexchange is possible, though they tend to be weaker and often dominated by competing antiferromagnetic interactions in oxides. They also typically occur in systems that show static orbital ordering or lattice-coordinated Jahn-Teller distortions, in which the *d*-orbital degeneracy between neighboring sites alternates. In the event of such orbital-lattice effects, insulating ferromagnetism has been known to occur.

In double exchange the electron transfer is real (not virtual) as the excited states are low enough in energy that they tend to occur easily [4]. In double exchange the electron transfers from next-to-nearest neighbor cations via the symmetry-allowed orbital on the intermediate anion. Since these cations tend to have different orbital occupations (different number of valence electrons) and the electrons are itinerant, electron transfers from the anion to the available state in the neighboring cation orbital as well. This results in the coincidence of ferromagnetism and conductive behavior in these types of materials. This type of exchange is usually found in mixed-valent conducting ferromagnets.

These examples give just a flavor of the types of indirect exchange mechanisms possible in magnetic oxides. We have left out theories for 90° superexchange between orthogonal non-overlapping orbitals which result in ferromagnetism and are more relevant to a discussion of spinels. With this qualitative understanding of exchange in oxides we can understand how magnetism in transition metal oxides is a highly correlated electron phenomenon. In these materials all the electrons play an important role and interact with the other electrons to generate fascinating functional behavior.

Hopefully, the preceding discussion has highlighted the value in the investigation of transition metal oxide perovskites. Small changes in lattice appear to be intimately related to the changes in the electronic and magnetic behavior in these materials. The unique versatility of perovksites motivates structural and chemical investigations which often result in numerous emergent properties. There is also value in the fact that the underlying mechanisms for the various behaviors can oftentimes be intuitively explained based on an understanding of the physical structure (and symmetry) and its effect on electronic interactions between the different ions in the material. By studying these systems we can hope to gain better understanding and control over spin and electron degrees of freedom to engineer useful spintronic devices.

1.3. Investigation of complex oxides using hetero-epitaxy

In this dissertation, we will use thin film epitaxy to affect changes in the perovskite structure. The advances in growth and characterization techniques in recent years have led to the increasing use of epitaxial synthesis of bilayer heterostructures and superlattices to study novel material phenomena. Modern

growth techniques combined with in-situ monitoring tools such as reflection high-energy electron diffraction (RHEED), secondary ion mass spectroscopy (SIMS), or X-ray techniques allow for atomic layer precision in the growth of materials and a high degree of chemical control of each constituent layer. Material engineering through hetero-epitaxy has thus been revisited as a viable means for developing new functionality in materials, especially in designing nanoscale functional properties in oxides which rely on strong spin-orbit coupling, or changes in electronic behavior induced by minute structural and chemical modifications.

There are two main routes in which hetero-epitaxy has been demonstrated to be a useful materials engineering tool: (i) generating novel interfacial phenomena; and (ii) generating novel ground states using epitaxial strain. The first route uses the idea of establishing electronic control by bringing a material in close proximity to another material to create a new interface. One often cited example of this is the recent discovery of a highly-confined, conducting two-dimensional electron gas formed at the interface between insulating $LaAlO_3$ and $SrTiO_3$ [16]. In this system, it is thought that a "polar catastrophe" develops, whereby the electric field at the surface of the ionic $LaAlO_3$ layers diverges. It is only resolved by the contribution of ½ an electron across the interface from the $LaAlO_3$ side to the final TiO_2 layer in $SrTiO_3$. The details of the explanation of this interface are still under intense investigation, but it is sufficient to say that this is an exciting new approach to discovering the latent properties in oxide materials [17]. Interface engineering is a valuable tool that has had great success in uncovering new properties that are not existent in the parent materials, but it will not be considered in this dissertation.

The second route entails manipulating a material's bulk equilibrium structure through coherent epitaxial growth on a lattice-mismatched substrate. As we have already alluded, this route can result in unexpected changes in the electronic behavior of a material, especially in complex oxides where orbital (lattice) degrees of freedom are strongly coupled to charge and spin degrees of freedom of the electrons. A recent example of this method is illustrated by the use of epitaxial strain on insulating $LaTiO_3$ to achieve metallic transport behavior [18]. This material is a Mott insulator with a small charge gap of 0.1 eV in the bulk. Through a suppression of the orthorhombic distortion from epitaxial growth on $SrTiO_3$, the bandwidth near the Fermi level is broadened and the t_{2g} level splitting is reduced, thus giving rise to metallicity in thin film form. The result demonstrates how epitaxial strain can induce a change in the electronic transport behavior [19]. In this dissertation, we focus on a similar approach to achieve new *magnetic* properties through structural modifications of perovskite cobaltites.

There have been some previous attempts to tune magnetic properties in oxides using heteroepitaxy. These rely on the use of strain to affect the sign and strength of spin-orbit coupling and magnetocrystalline anisotropy or the use of complementary nonmagnetic multilayers to generate magnetism at an interface. In this work we present an alternative approach that focuses on tuning the local moment on an ion via the spin state to generate a magnetic response which was absent prior to the subjection to strain. By experimenting with control over the local spin state, we can aim to control both the magnitude and presence of long-range

magnetic order in these materials, thus giving rise to a unique form of magnetic functionality.

1.4. Exploitation of spin state transitions in cobaltites

The cobaltites are a unique class of materials that can assume a range of different spin state configurations at different temperatures. In particular, these changes in spin state in the bulk have given rise to anomalies in magnetic susceptibility and electron transport [20, 21]. As we have suggested above, by finding a route to access these spin states independent of temperature, we can hope to create new functionality for oxide-based electronics through the manipulation of magnetic moment and electronic behavior of a material. One well studied example of these compounds, $LaCoO_3$, undergoes a spin state transition at low temperature. There is a consensus that above 25 K some Co ions in $LaCoO_3$ begin to transition to some higher spin state from a low spin state (LS, S=0). There is still considerable debate as to whether the high spin (HS, S=2) or intermediate spin state (IS, S=1) of Co is more stable at higher temperatures. Figure 7 shows the possible spin states for Co suggested for this material. Because of the strong competition between crystal field splitting energy (Δ_{CF}) and Hund's coupling (Δ_{ex}) in this system, the LS, IS, and HS states have been shown to be close in energy [22, 23] and are, therefore, easily accessible with temperature. In any case, bulk cobaltites do not show any long-range magnetic ordering or indication of substantial HS or IS Co population at low temperatures. However, this material holds tremendous promise for our purposes, as it has the potential to show a dramatic change in the magnitude of the (spin-only) magnetic moment from no net moment (S=0) to 4 μ_B/Co (S=2).

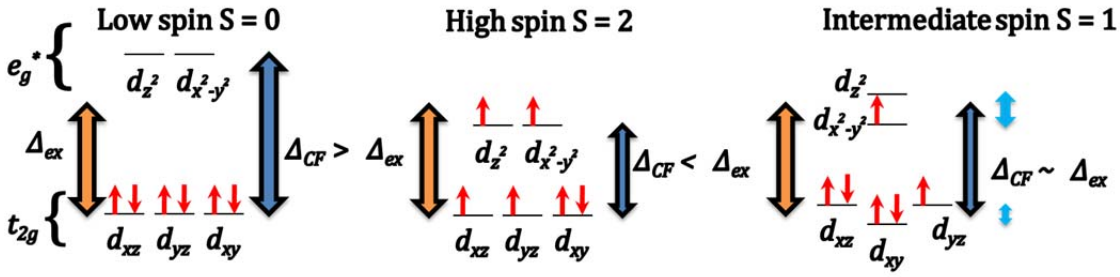

Figure 7 Possible spin state configurations for $LaCoO_3$. Low spin, high spin, and intermediate spin electron configurations have all been proposed. The $LaCoO_3$ system adopts an evolving mixture of these spin states with increasing temperature.

Numerous efforts have been made to control the spin state through other external parameters aside from temperature. The most likely routes to this control must focus on manipulating the crystal field through modifications of the Co-O bond length and Co-O-Co bond angle. Previous efforts to enhance the stability of the low spin, low temperature state using hydrostatic pressure have been successful [24, 25, 26]. Hydrostatic pressure increases crystal field splitting energy due to the increase

in orbital overlap that competes with the Hund's coupling energy. This increase in crystal field splitting stabilizes the low spin state of Co ions in a similar way as the scenario presented earlier in this chapter.

Another approach, which will be explored in greater detail in Chapter 5 of this dissertation, is bandwidth engineering by doping the A-site cation, La, with a smaller rare-earth metal, i.e. Pr, to alter the Co-O-Co bond angles and e_g and t_{2g} bandwidths related to the Co-O orbital overlap [27]. This method of so-called "chemical pressure" uses substitution of isovalent cations in the A-site. This does not typically result in dramatic changes in the Co-O bond-length, but instead a change in the Co-O-Co bond angle, which deviates to smaller angles from 167° [28] (in LCO). The result is an increase in octahedral tilts as the overall symmetry becomes orthorhombic. This change has been closely associated with a reduction in the e_g bandwidth resulting in a more stable low spin state with decreasing A-site cation size. The spin state transition temperature is shifted from ~25 K in LCO to 200 K in PCO, and as high as ~540 K for $LuCoO_3$ (Co-O-Co angle ~146°) [27].

The only well-established success in destabilizing the low spin state and enhancing the stability of a higher spin state in bulk LCO and PCO has been through the use of aliovalent cation substitutions on the A-site to introduce a mixture of valence states for the Co ion. For example in $La_{1-x}Sr_xCoO_3$ and $Pr_{1-x}Sr_xCoO_3$, Sr^{2+} results in the presence of smaller, intermediate spin, intermediate valence, Co ions. With x >0.2 and full percolation of the mixed ion/spin clusters, this mixture of Co valence and spin states results in a metallic e_g electron transport behavior and ferromagnetism [29, 30].

Recently, there has been considerable effort to use epitaxial strain to drive the Co ions in LCO to a higher spin state [31, 32, 33, 34, 35, 36]. While epitaxial films of LCO were found to be ferromagnetic, an actual understanding of the strain-derived Co spin states in these films has not been established. In addition there is controversy in the literature as to whether it is in fact strain [33, 37] or stoichiometric defects [35, 36, 38] induced by the growth which can be cited as the primary cause for apparent changes in the Co spin state, and thus responsible for the observed ferromagnetic order in these films.

The origins of the changes in Co spin state and the ferromagnetism have not been the only sources of controversy in $LaCoO_3$ films. While there is a consensus that films in tension inevitably result in ferromagnetism, during the course of investigations by numerous groups, both ferromagnetic and non-ferromagnetic behavior have been reported for films under biaxial compression. Many authors who have performed substrate dependent investigations observed ferromagnetism in films grown in compression on LAO and SLAO [33, 37]. A transmission electron microscope investigation into films on LAO observed dichroism in the EELS spectra at low temperature related to ferromagnetism [39]. However, Park et al. performed a magnetic force microscopy study showing that while ferromagnetism is likely to be strongly associated with epitaxy in tension, ferromagnetism on LAO (compression) appears to arise mostly from chemical inhomogeneity [35]. In chapter 4 we will report on thickness dependence of ferromagnetic properties for films on LAO, and will show that strained films on LAO are not magnetic while

relaxed films show ferromagnetism. Collectively, these results suggest that both strain and defects can give rise to long-range ferromagnetic order in $LaCoO_3$.

By investigating cobaltites in detail using hetero-epitaxial synthesis on a series of different substrates, we hope to better understand the unexplained ferromagnetism in this system. In addition, by studying the magnetic properties under chemical pressure from the substitution of Pr in the A-site, we have found epitaxial strain dominates over the influence of chemical pressure in governing the spin states present in the PCO film. Remarkably, in this system we have found that the Pr ions show long-range order antiparallel to the Co sublattice in the presence of HS ferromagnetic Co ions.

1.5. Goals of this dissertation

In the chapters to come we will explore the novel ferromagnetic ground states in cobaltite materials accessed through hetero-epitaxial synthesis. In chapter 2, we will review the pulsed-laser deposition growth technique and various characterization techniques that are used throughout this dissertation. In Chapter 3 and 4 films grown on LAO, LSAT and STO substrates of LCO will be explored in detail. Chapter 3 will focus on the structural characterization using X-ray diffraction and scanning tunneling electron microscopy techniques to explore the effects of growth on a lattice-mismatched substrate and the effects of relaxation with increasing thickness of the films. Chapter 4 will connect these details to trends in magnetometry data and the electronic structure properties found from X-ray absorption techniques. In Chapter 5 these characterization tools will be used to investigate strained films of PCO and to explore the Co and Pr sublattice ordering under chemical pressure effects that compete with the epitaxial strain. In chapter 6 we will summarize the results presented in this work, and provide a sense of direction for future exploration of novel phenomena in these materials.

This dissertation explores the effects of using epitaxial strain to engineer novel ordered magnetic behavior through the manipulation of the spin states in cobaltites. This represents a new use of epitaxial strain to control the magnetic behavior of oxides. We show that the ferromagnetism in the films has contributions from both the structural distortions and the defects generated during growth. By exploring the effects from lattice distortions and epitaxial growth in great detail using modern microscopic and spectroscopic tools, we are able to discern the relevant electronic configurations and lattice distortions that make up the ferromagnetism in these films. Finally, we show that this use of epitaxial strain to engineer novel magnetic states is powerful enough that it can be extended to other cobaltites such as $PrCoO_3$, where the high spin state is less accessible. In this rare-earth cobaltite, we demonstrate an emergent novel ferrimagnetism that occurs due to the stabilization of HS state-mediated magnetic order in the Co sublattice. Thus, by manipulating the spin state in the Co ions we are able to induce an anti-parallel long-range ordering of the moments in the otherwise paramagnetic Pr sublattice in $PrCoO_3$. We are only at the beginning stages of the development of complex oxide materials for industrial spintronic applications. Much more work beyond this

dissertation still remains to better our understanding of the profound effects of chemical dopants, oxygen vacancies, phonons, electromagnetic fields, and mechanical stresses on the unique properties displayed by these materials.

Chapter 2: Experimental Techniques

2.1. Sample Fabrication

2.1.1. PLD

2.2. Sample Characterization

2.2.1. Atomic Force Microscope/Microscopy

2.2.2. X-ray Diffraction

2.2.3. Rutherford Back-Scattering

2.2.4. Magnetometry

2.2.5. X-ray Absorption Spectroscopy (XAS)

2.2.5.1. X-ray Magnetic Circular Dichroism

2.2.5.2. X-ray Natural and Magnetic Linear Dichroism

2.2.6. TEM and STEM/EELS

Abstract

In this chapter the techniques used for growth and characterization of oxide films are briefly discussed. A survey of the techniques used in this work and some specific considerations used when carrying out experiments are highlighted. In particular, important precautions for oxide growth using pulsed-laser deposition are addressed. Important precautions necessary to ensure measurement accuracy and proper analysis taken during the post-growth characterization techniques will also be explained.

Chapter 2: Experimental Techniques

2.1. Sample Fabrication

The most important aspect of a thin film investigation is proper attention and care during sample fabrication. While numerous technological advances have made the synthesis of single crystalline thin films with precise atomic layer control relatively routine, diligence is still required at each step. In the first part of this chapter, we will explain the thin film growth technique known as pulsed-laser deposition (PLD) that was used in the course of this investigation. The deposition process of this growth technique as well as the important considerations to bear in mind when carrying out thin film syntheses will be discussed.

2.1.1. Pulsed-Laser Deposition (PLD)

Pulsed-laser deposition (PLD) has become the workhorse for oxide research, due to its ability to create high quality crystalline films quickly and easily from ablation of a stoichiometric pressed ceramic target. However, despite the relative ease with which thin films may be fabricated, numerous complex interactions take place during the growth. A schematic of the PLD system used for these growths is shown in Figure 8. The PLD process is usually thought of as a four stage process [1, 2]: (i) the laser beam interacts with the target and generates a plume; (ii) the plume interacts with the background gas on its way to the substrate; (iii) constituents of the plume stick to the heated substrate; and, finally, (iv) the constituents from the plume nucleate and grow into layers of film material.

The first stage involves the transfer of energy from a high powered laser to a target material (stage 1). This (typically) stoichiometric target is superheated by its ability to absorb the photons from the incident laser, and results in a rapid thermal evaporation and simultaneous ionization of its constituent atoms. The result of this interaction is a highly energetic plume of neutral atoms, ions, electrons, and, in some cases, molecules that interact with the gases in the deposition path and are directed towards a heated substrate (stage 2). The species in the plume then land and stick on the substrate (stage 3) mostly based on the sticking coefficient onto the substrate for the material being deposited. Finally, through the aid of remnant kinetic energy from the plume generation process and added heat from the substrate heater, they diffuse and nucleate into (ideally) highly ordered atomic layers (stage 4). This nucleation and growth is governed by the density of the incident plume species on the substrate, the overall anneal time and temperature, and the properties (thermal diffusivity, thickness, surface energy) of the underlying layers.

At each step in this process, numerous parameters can be tuned to obtain high quality, uniform, stoichiometric growth to investigate novel oxide properties with confidence. The parameters can be separated into those affecting the laser-target interactions and plume-substrate interactions. On the laser-target side, we will consider laser energy (density), spot size, pulse frequency, target density, and target surface morphology. On the plume-substrate side, we will explore the role of

oxygen background pressure, substrate temperature, substrate distance, and substrate preparation.

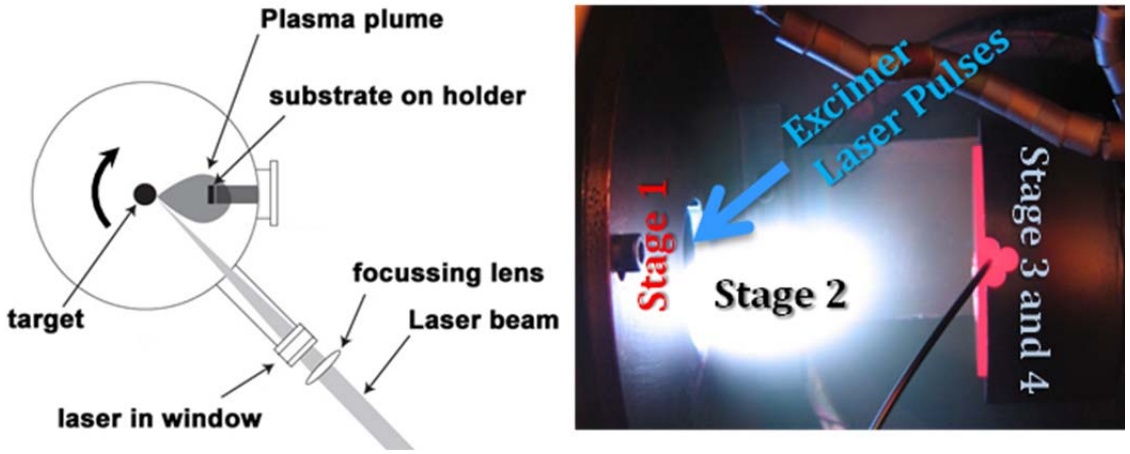

Figure 8 Schematic of a pulsed-laser deposition configuration and an image taken during a high oxygen pressure growth at 700˚C

The first stage in this growth process relies heavily on the various tunable properties of the laser. In fact one of the aspects that makes PLD well suited for oxide film synthesis is the advances in excimer laser technology that provide high energy (and low average power), coherent beams at the suitable wavelengths for absorption by most oxide materials. Excimer lasers are now available at energies from 157 nm (~7.91 eV, F_2 laser) to 351 nm (~3.53 eV, XeF laser). Thus, for the growth of complex oxides, choosing a laser of the appropriate wavelength that is absorbed by the target material is important. It is for this same reason that PLD is virtually impossible for metallic materials. The high reflectivity of these materials in these wavelengths prevents sufficient energy transfer per pulse to the target material. By choosing a KrF excimer laser that emits quick (10-30 ns) 248 nm (5 eV) pulses, we are able to grow with considerable speed and can accommodate a large number of complex oxide materials.

Since the laser wavelength and pulse duration is set by the laser, the most critical controllable parameter of the laser is the *energy density*. The energy density is determined by the spot size and energy delivered by the laser. For a given spot size, the laser energy and consequently the overall energy density delivered to the target require some optimization. The plume generated during the target-laser interaction is created by the rapid vaporization of the target material from thermal ablation and from the strong Coulomb repulsion of ions in the target that have ejected photoelectrons after absorbing the laser energy. Thus, a target will not vaporize enough material to form a plume until a certain energy ablation threshold is reached. This threshold energy density can depend on target density, atomic mass of the target elements, and absorption skin depth of the target. However, it is also important to note that depositing with too high of an energy density can result in a highly ionized plume which can contribute to stoichiometric defects in the film. For most of our complex oxide thin film growth, the energy density values ranges from

0.5 – 2 J/cm^2. Thin film quality and speed of growth can be further optimized by experimenting within this range.

Controlling the *spot size* can also have effects on the quality of the film. A smaller spot size results in larger plume spread [3, 4] and becomes less peaked in the forward direction. This effect is understood in terms of the laws governing gas dynamics where greater plume divergence occurs from the corners of a laser spot. As a result the growth rate is slowed considerably and a larger spatial uniform, albeit slower, plume is delivered to the substrate per pulse. A small spot size, however, introduces inconsistencies in the energy density and plume stoichiometry from pulse to pulse arising from defects, chemical and morphological inhomogeneities in the target, or drift in the laser energy. On the other hand, a larger spot generates a more forward directed plume, faster growth rates, and a more robust energy density, but will lead to more inhomogeneities in directions off of the axis perpendicular to the target surface. For the majority of the growths carried out in this work (except when indicated) the spot size was chosen to be on the larger side ranging from 1.0- 1.2 cm^2.

Another important parameter associated with the laser is the *laser pulse rate* which can be tuned to enable faster or slower growths. This can have dramatic effects on the surface quality of the film. A faster pulse rate can create a pile up of atoms to supersaturate the number of species at the growth interface on the substrate. On the other hand a slower pulse rate can allow more time between pulses for species to diffuse and the surface to recover (with the aid of thermal energy supplied by the substrate heater). In film materials or film orientations that are difficult to grow under thermal equilibrium conditions, a faster pulse rate may be more desirable to prevent the excess exposure to high temperatures. This could help prevent the system from relaxing to its most stable lowest energy state. The choice of pulse rate also may affect the growth mode of the film and could require some optimization to achieve the desired film properties.

In addition to the laser, we have to take into consideration the quality and condition of the target. It is usually desirable to ablate a target with high density since the density can play a significant role in ablation thresholds and efficiency of the plume generation process. The overall surface morphology of the target impinged upon by the laser can affect the stoichiometry and density of clusters in the plume. Typically, a smooth surface is desired; however, over the course of numerous laser-target ablation processes an unavoidable cone-like morphology develops.

To minimize variation and improve reproducibility from run-to-run, we carry out the following. First the target surface is made smooth by sanding the target prior to growth. Then the target is pre-ablated for about 5 minutes under the deposition conditions before exposing the substrate to the target plume. During the actual deposition and during the pre-ablation process, a target rotation system is used to continually move the laser spot to a new position on the target. This establishes a uniform, consistent track over which the laser can ablate the target during the actual film deposition. The pre-ablation step helps to avoid any significant change that might occur in the growth due to the changes in the surface

morphology of the target from the initial ablation (after the sanding step). In this way the plume will ideally adopt a certain degree of uniformity that is maintained throughout the growth process.

Once such a uniform plume is generated by the laser-target ablation process, it is forward directed with neutral atoms, ions, electrons and molecules of energies of several hundreds of eV towards the heated substrate. In a number of oxide growths it is necessary to allow the highly energetic plume to interact with an oxygen gas before reaching the substrate. The ambient oxygen atmosphere can serve two purposes: to slow down and lower the energy at which the plume constituents approach the substrate surface (kinetics), and to enhance the stoichiometry of the film (chemistry) to correct for deficiencies in the target, or ensure full oxygenation of more reductive material systems. However, the addition of this background gas does have some disadvantages. In general, adding the background oxygen will lower the mean free path of the species in the plume resulting in multiple bombardments and possible cluster formation with the oxygen gas. This can result in large clusters forming and depositing on the surface of the film. On the other hand, a complete absence of the background gas, without proper attention to the laser energy density used, can result in an overly energetic (several hundred eV) plume that can ablate material from the surface of the newly forming film. In some instances, higher oxygen pressures must be used to ensure full oxygenation of the film at the expense of increased film roughness.

Some of the issues regarding the mean-free path of the plume species in these ambient pressures can be affected by changing the substrate to target distance. Bringing the substrate closer to the target will increase the number of plume species that impinge on the surface and increase the growth rate. However, bringing the substrate too far into the plume can result in re-ablation of the film deposited on the substrate surface by the energetic plume causing stoichiometric and structural defects. In our study, we held the substrate to target distance at ~7.6 cm to ensure that the plume did not engulf the film.

Finally, the *substrate temperature* must also be optimized. Higher temperatures can result in higher crystallinity, but may cause excess diffusion of atoms in the sample, affecting the stoichiometry or homogeneity in the film and across the substrate/film interface. Increasing the temperature will also drive the growth towards thermal equilibrium, and may be undesirable in the synthesis of some materials that require the kinetic benefits of PLD growth to form stable single-crystalline films. In the end a balance must be struck among the parameters of laser energy density, oxygen background pressure, pulse frequency, substrate distance, and substrate temperature to obtain optimal smooth film growth at reasonable rates.

Many steps can be taken to prepare substrates for sample fabrication, ranging from subjecting the substrates to a comprehensive onslaught of characterization (SQUID, AFM, XRD, etc.) to minor chemical etching, thermal annealing, and general substrate washing. For the growths performed in this work, the procedure was kept simple and the substrates were simply washed using acetone, methanol, and isopropanol in an ultrasonic bath for 5- 15 minutes. Some

samples were subjected to measurements in the atomic force microscope (to determine substrate miscut) and others were subjected to measurements in the SQUID magnetometer to obtain background magnetic response data that could be useful in background subtractions for future film measurements. Of paramount importance is that the substrate surface is free of dust or defects that could adversely affect film properties.

Up to four substrates can be loaded onto the heater using silver paste making sure to confine the position of the substrates to within a 1 cm^2 area in the central region of the heater along the central axis of the plume. When applying the silver paste, great care was taken to ensure just enough was applied to allow for good thermal contact between the substrates and the heater. If too much silver paste is used, there is a risk of paste sticking along the sides of the substrate or even landing on the surface of the substrate. To ensure uniform heating of the substrates, we must apply paste only along the back surface of the substrate. Prior to installing the heater into the chamber, the heater is heated to ~200- 300°C outside of the vacuum chamber to drive off all solvents from the paste. This aids in more rapid pump down of the chamber.

Post-growth processing can be of utmost importance especially in ensuring proper oxygen stoichiometry and microstructure. The details of the sample cooling process or additional post-growth annealing step can be crucial in obtaining highly crystalline, stoichiometric films. In general, for the thin film studies in this dissertation, the films grown in 320 mTorr were cooled in at least 1 Torr of oxygen. When lower growth pressures were used, the sample was cooled in the pressure used during growth. Only in some specific annealing studies, were films annealed in 600- 1000°C for a few hours in a tube furnace exposed to air. If the films are oxygen deficient, this process should be sufficient to diffuse oxygen throughout the samples.

Additionally, great care is needed when handling the samples with tweezers and when removing silver paste. For SQUID measurements, remnant silver paste was gently sanded off the backside using nonmagnetic sand paper. After silver paste removal, the samples were gently rinsed in isopropanol to remove any dust or particles that may scratch the films. Small amounts of impurities in the film or damage to the film can adversely affect measurements, and so the utmost care is taken during these steps.

Using this approach, we synthesized high quality oxide films in order to carry out the investigations presented here. Our high quality single crystalline substrates were typically obtained from Crystec, GmbH. The $LaCoO_3$ target used in this dissertation was obtained from Praxair. The $PrCoO_3$ target used in Chapter 5 was sintered and pressed by Shameek Bose and Dr. Christopher Leighton at the University of Minnesota. It was synthesized by solid state reaction of stoichiometric quantities of Pr_6O_{11} (Sigma-Aldrich, 99.9% purity) and Co $(C_2O_4).2H_20$ (Sigma-Aldrich) powders. The reactants were thoroughly ground and reacted at 1000˚C in air for 7 days, with 2 intermediate grindings. The reacted powder was then cold-pressed into a disk at 16,000 psi and sintered at 1200˚C in air for 96 hours. It was then slow cooled to room temperature at 0.5˚C/min. The phase purity of the target was confirmed by X-ray diffraction prior to use in PLD film synthesis.

2.2. Sample Characterization

Once samples were grown, a range of characterization techniques were performed to ensure high structural quality as well as to determine functional properties of these films. The remainder of this chapter is devoted to describing the various characterization techniques that were used in carrying out the research in the following chapters. While some characterization methods are left out and not all of these methods are used on every grown sample, we introduce many of the methods that were used in the course of this dissertation. Throughout this dissertation, we have focused on the structural and magnetic characterization of complex oxide thin films. We will cover atomic force microscopy (AFM), X-ray diffraction (XRD), Rutherford backscattering spectrometry (RBS), magnetometry, X-ray absorption (XA) techniques, and scanning tunneling electron microscopy (STEM) techniques. RBS was performed after training under Dr. Kin Man Yu at Lawrence Berkeley National Laboratory (LBNL). The XA measurements were performed at the Advance Light Source at Beamlines 6.3.1 and 4.0.2 in collaboration with Dr. Elke Arenholz. The STEM and EELS measurements were performed by Dr. Maria Varela and Dr. Neven Biskup at Oak Ridge National Laboratory.

2.2.1. Atomic Force Microscopy (AFM)

An atomic force microscope (AFM) was used to probe the surface morphology of the films. A silicon cantilever is oscillated at a set frequency as it is rastered over the surface of the sample. As the cantilever encounters features on the film surface, the change in the oscillation frequency is monitored by an optical laser on the cantilever. These frequency changes (changes in phase and amplitude) are then output visually by correspondingly varying pixel contrast to produce an image of the surface of the film. The Digital Instruments Dimension 3100 Scanning Probe Microscope used in this dissertation has a very high vertical resolution of < 1 Å. On the other hand the lateral resolution is < 20 nm. For our purpose of measuring the average surface roughness over the entire sample this is sufficient since smooth films can be characterized by root-mean-squared (RMS) roughness values on the order of a unit cell for our materials (~ 4 Å). Any large islands formed during growth will be obvious from an increase in the RMS roughness value.

This technique provides a good check for the quality of the substrate prior to the growth of the film, as well as for the film after growth. In ideal single crystalline growth the surface would be extremely smooth (< 3 Å) and terraced features evident in the bare substrate (from intentional substrate polishing at a miscut angle) would make their appearance on the surface of the film. Smooth films tend to attract dust and other particulates over time and thus measurement of the surface using an AFM was carried out immediately following growth (and prior to any other characterization technique or sample handling).

2.2.2. X-ray Diffraction (XRD)

X-ray Diffraction (XRD) was used to determine the majority of the structural properties of the film. XRD uses the phenomena of constructive interference from elastically scattered X-rays incident on a sample to provide information regarding the sample's crystal structure [5]. Figure 9 shows two geometries that satisfy Bragg's Law, $n\lambda = 2d\sin\theta$ or $\vec{k'} - \vec{k} = \Delta\vec{k} = \vec{G}$, such that information regarding the interplanar spacing in the crystal lattice could be obtained. By determining the angles at which the Bragg condition is satisfied, we can obtain information about the lattice parameter for films grown on different substrates under various conditions could be taken.

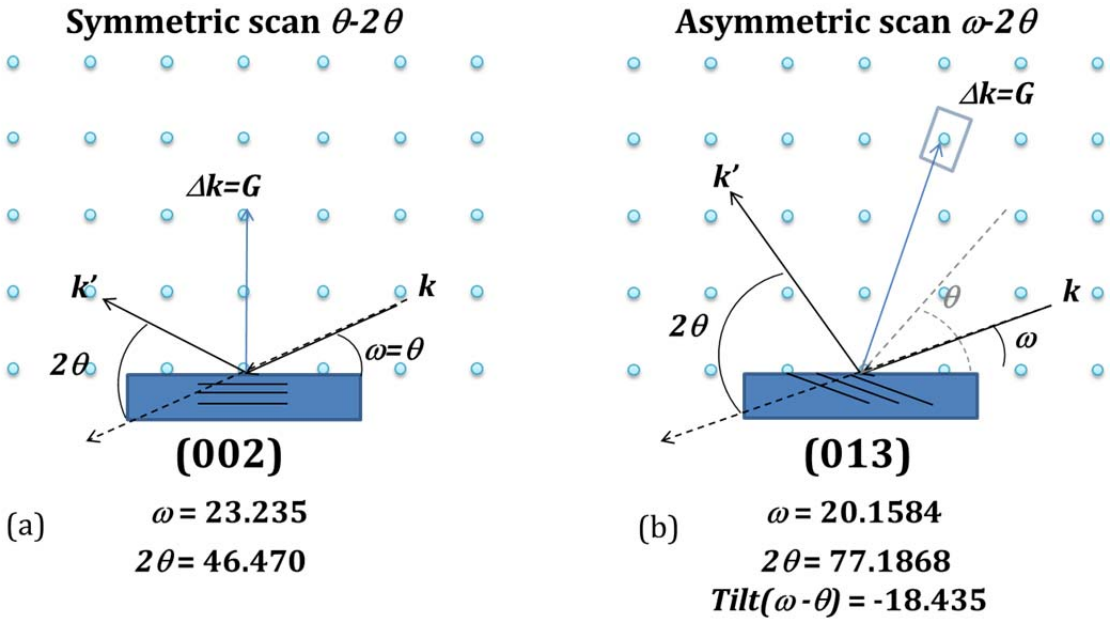

Figure 9 Schematic showing sample orientations relative to incident and diffracted beam for two different types of diffraction scan

In a standard $\theta - 2\theta$ measurement, ω is held constant to $2\theta/2$ while the 2θ value is swept over a large angle range (see Figure 9(a)). In this type of symmetric scan, the out-of-plane lattice parameter of the films could be determined. Additional information regarding the crystalline quality of the films and the mosaic spread of grains in the film is determined by rocking the ω angle about the $2\theta/2$ angle while fixing the detector 2θ value to an out-of-plane peak of the film. The full width at half maximum (FWHM) of the ω scan, or $\Delta\omega$, is regarded as a measure of crystallinity.

To obtain in-plane lattice parameters of the films, we used asymmetric scans (Figure 9(b)) with the scattering vector satisfying the Bragg condition and corresponding to a lattice vector that has in-plane and out-of-plane components [6]. In these asymmetric measurements, ω is equal to $2\theta + \partial_{offset}$ to cause a tilting of the sample so that the scattering vector is no longer normal to the film surface (as it was for the $\theta - 2\theta$ measurement). In order to determine the relationship between

film and substrate peaks, we take a series of $\omega - 2\theta$ scans over a small range in both ω and 2θ. In this way an intensity map can be obtained as a function of ω and 2θ, representing a two-dimensional cut of reciprocal space which can be used to determine the real space lattice spacing between planes along in-plane and out-of-plane directions. This type of two-dimensional scan is called a reciprocal space map (RSM).

The final XRD geometry that will be discussed pertains to the usage of grazing incidence X-ray reflectivity to determine the thickness of individual layers grown in single films and multi-layered structures. To perform a reflectivity measurement, a symmetric scan is measured in the range of 0- 10° using a set of source and detector optics optimized for higher X-ray intensities to determine the angle below which total internal reflection of the X-rays in the film occurs. This angle is related to the refractive index of the film. Strong interference effects are known to occur between boundaries of different refractive index (film and substrate, film and air) that give rise to "fringing" of the low angle diffracted X-ray beam. Using information related to the critical angle of internal reflection and the period between fringes, we can determine the thickness of the film or individual layers in a film. When the sample was between 5 nm and 100 nm thick, the thickness was determined using the X-ray reflectivity technique. For thicker samples RBS was used to more accurately determine film thickness.

All XRD work presented in this dissertation was carried out using a Philips Panalytical four-circle Materials Research Diffractometer (MRD) at LBNL. A Cu *K*-edge line source was used to generate the X-rays. The beam was conditioned with a parabolic mirror and a Ge 220 4-bounce crystal monochromator before impinging on the sample to collimate and monochromate the X-rays to the Cu K_α wavelength of 1.541 Å. For X-ray reflectivity, the monochromator is removed to increase the intensity (at the expense of wavelength resolution) and a set of parallel slits (soller slits) are inserted before the detector to limit the beam divergence and enhance the low scattering angle resolution.

2.2.3. Rutherford Backscattering Spectrometry (RBS)

Rutherford Backscattering Spectrometry (RBS) was used to determine the stoichiometry of the sample and the thickness of samples greater than 100 nm. The technique relies on the energy loss detection of backscattered He^{2+} (2-3 MeV) ions after impinging on the sample [7]. The energy of the detected ion is affected by scattering with atoms at the surface and the interior of the sample. The mass of the atoms in the sample affect the strength of the interaction with the impinging ions. Heavier elements have higher scattering cross-sections and stronger interactions, and as a result, RBS is more sensitive for detecting quantities of heavier elements. At a fixed detection angle the backscattered ion will have a different energy for scattering events with different elements. Ions that penetrate further into a sample also lose more energy before backscattering to the detector. In an RBS spectrum the peak position and intensity is governed by the scattering cross-section of the element scattering the impinging ion. The width, and in the case of buried elements,

relative shift of peak position is determined by the depth of the element scattering the impinging ion. In this dissertation, RBS resolution is worse for lighter elements, such as oxygen, and is only used to determine the relative ratio of heavier elements in the samples and for thickness determination of some samples. The measurements were performed at the Ion Beam Analysis Facility at Lawrence Berkeley National Laboratory with the help of Dr. Kin Man Yu. The analysis was performed using SIMNRA software to fit the spectra [8].

2.2.4. Magnetometry

Measurements of the net magnetic response of the film were performed using magnetometry. Magnetometers can be used to obtain a wealth of information regarding the magnetization with respect to temperature and field. They can also evaluate, to some extent, the anisotropy (angular/ structural) of the magnetic response. Because of the possible contributions to the magnetic response from various sources [9, 10, 11, 12], including the substrate, adhesives, magnetic dust as well as the sample itself, sample mounting procedures, sample handling procedures, and the management of background signal arising from the different substrates need to be carefully monitored.

Samples were mounted in plastic straws in either in-plane (straw parallel to sample plane) or out-of-plane (straw perpendicular to sample plane) configuration. The sample is placed in the straw using tweezers and typically slid to the middle of the straw using wooden cotton swabs to gently move the sample within the straw without scratching or putting undue pressure on the sample. In instances of smaller than 5 mm x 5 mm samples it was necessary to use secondary straws, slit along the length of the straw, to provide extra cushioning between the sample edges and the inner wall of the (uncut) straw. In such instances, the sample is mounted in the slit straw first, and then slid into the uncut straw. When mounting in the out-of-plane configuration it was difficult to mount samples larger than 3 mm x 5 mm. In such instances, we used a series of concentrically mounted partially slit straws with no uncut straw. In all instances the ends were usually taped with Kapton tape to ensure the sample would not be lost during the course of the measurement, and to ensure that the slit straws would not become loose from the assembly. Using this straw method, with minimal use of Kapton tape, string or other mounting devices, was important for minimizing unwanted magnetic impurities that could adversely affect the measurement. Clean straws provided a uniform low signal diamagnetic background that was, in most instances, easily subtracted out

For the measurements presented in this dissertation, the most effective method for comparing the magnetic response of samples relied on careful handling and mounting of the sample combined with a simple linear background subtraction of the substrate signal. This method yields the most consistent results and means for comparing films grown at different times, on different substrates, with different amounts of silver paste. Since there existed a linear region in all measurements presented in this dissertation between +3 T → 5 T and -3 T → -5 T with identical slopes, this average slope was subtracted from the raw signal.

This method presumes no diamagnetic or paramagnetic contribution to the signal exists from the film (if so, such components are subtracted out by the main background subtraction). This method also presumes that any components of the raw signal from the substrate, remnant silver paste, or dust are all diamagnetic. On occasion ferromagnetic impurities from sources outside of the film (contaminated substrates, poor tweezer handling, etc.) may appear in the signal, in which case, it becomes necessary to repeat the entire experiment with new samples. Bare substrates were also measured to confirm that the signal for a clean high quality substrate is diamagnetic and linear.

The film magnetization measurements in this dissertation were made using a Quantum Design Superconducting Quantum Interference Device Magnetometer (SQUID) equipped with a 5 Tesla DC magnet and a cryostat for measurements down to 4.2 K using liquid helium. The DC SQUID head allows for high resolution magnetic flux detection with the ability to measure magnetic signals above $\sim 2\text{x}10^{-7}$ emu.

2.2.5. X-ray Absorption Spectroscopy (XAS)

X-ray absorption (XA) spectroscopy performed in this dissertation measures X-ray absorption in the sample as a function of energy and gives information about the electronic structure of the films. By using an element specific energy range of the incident X-ray, different initial core state electrons (arising from different elements in the sample) are excited to a final state electron configuration [13]. This technique can be used to garner information about the electron configuration, hybridization, and coordination of the electrons in the films. XA intensity is the difference between incident (I_0) and "transmitted" (I_t) X-rays through the sample due to the energy-dependent XA coefficient (μ_x), and is given by $I_0 - I_0 e^{-\mu_x d}$. For very thin samples (surfaces) or for electron escape depths much smaller than the XA length, total electron yield measurements give a difference that is directly proportional to the XA coefficient given by $\sim I_0 \mu_x$. Thus, one can easily observe changes in the XA intensity in total electron yield by detecting changes in the current coming off the sample using a picoammeter, though one should always be wary of saturation effects [14]. These effects are a result of the decreasing X-ray penetration depth as energy is swept through the absorption edge. When this depth decreases to the order of the electron escape depth, (~2-5 nm) distortion of the spectral features can occur making analysis difficult.

In general the X-ray absorption process is a first-order transition induced by an incident electromagnetic radiation between some initial state and final state. Using first-order perturbation theory in the dipole approximation ($\lambda_{X-ray} \gg r_{electron\ orbit}$), we can determine the selection rules for the induced transition by considering $I_{abs} \sim |\langle f|H_{int}|i\rangle|^2 \sim |\langle b|\boldsymbol{\epsilon}\cdot\boldsymbol{r}|a\rangle|^2$ where a and b are the initial and final electronic states, and $\boldsymbol{\epsilon}$ is the unit photon polarization vector and $\boldsymbol{r}$ is the electron position vector. The matrix elements ($|\langle b|\boldsymbol{\epsilon}\cdot\boldsymbol{r}|a\rangle|^2$) for the electron states can be further separated into the radial and angular components while the dot product gives the polarization dependent dipole operator and is related to the polarization

of incident X-rays (horizontal linear, vertical linear, right circular, left circular, etc.). The non-zero matrix elements have been calculated by Stohr [13] and the dipole selection rules can be read off by inspection. The selection rules allow for transitions where $\Delta l = \pm l, \Delta m_l = 0, \pm 1, \Delta s = 0, and\ \Delta m_s = 0$ and so the X-ray absorption spectroscopy can be used to measure the element specific valence shell properties. Specifically, we can use soft X-rays to probe the allowed electron transitions from O *1s*→ *2p* transitions, transition metal *2p*→ *3d* transitions, and rare-earth metal *3d*→ *4f* transitions in our samples.

In order to obtain a spectrum that is independent of sample geometry or polarization direction and sensitive to the total number of holes in the valence band, it is important to take an averaged spectrum over all incidence angles (two in-plane and one out-of-plane) or over all polarizations (right circular, left circular, and linear). If information regarding the sample's structural symmetry is known, we can reduce the number of scans needed. For example, for magnetic tetragonal single crystals with $a = b \neq c$,measurements need to be taken with the E-field both in-plane and out-of-plane if using linearly polarized light or at a constant X-ray incidence angle using both left and right circular polarization (or, equivalently, alternating field and a single polarization). If this is done, the measured spectrum is isotropic and the information it gives is void of any anisotropic magnetic or crystalline effects. In this dissertation, the XA spectra are typically taken as the sum of right and left circularly polarized X-rays (~60% polarized at Beamline 6.3.1 and ~90% polarized at Beamline 4.0.2). The X-rays are absorbed at a grazing 30˚ sample incidence angle or a normal 90˚ sample incidence angle.

2.2.5.1. X-ray Magnetic Circular Dichroism (XMCD)

XMCD probes the element specific magnetism of a material through spin dependent electronic transitions. In order to probe the magnetism, XA spectroscopy is performed with circularly polarized incident X-ray radiation. By using circularly polarized X-rays the absorption process becomes spin dependent since the angular moment of the incident photons can be used to preferentially excite spin-up or spin-down electrons. By measuring the difference in XA spectra with incident left or right circularly polarized X-rays in a constant magnetic field, we can determine information regarding the spin of the holes in the valence band. When the photon angular momentum, $\boldsymbol{L_{ph}}$, is collinear to the sample magnetization, *M*, the XMCD signal is maximized. Alternatively, the difference, or dichroism, can be measured by alternating the applied magnetic field, and hence the magnetization direction, while keeping the photon spin direction (or angular momentum) constant. For all the measurements presented here, the difference of the absorption spectra, often represented by $I^{\uparrow\downarrow} - I^{\uparrow\uparrow}$, is taken in positive and negative fields (the arrows indicate the relative orientation of photon spin and magnetic moments).

The spin dependent X-ray absorption process can be thought of as occurring in two steps. In the first step, the angular momentum of the incident photon is partially transferred through spin-orbit coupling to the spin of the excited photoelectron. For transition metals this electron is excited with opposite spin

polarizations from the $2p_{3/2}$ and $2p_{1/2}$ spin orbit (*l+s* and *l-s*, respectively) split levels. The next step involves detection (absorption) of the spin-polarized photoelectron in the spin-up and spin-down levels of the valence band which are split by the exchange energy. Because the selection rules (see previous section) for the X-ray absorption process does not allow for spin-flip processes, only transitions to levels with the same spin polarization in the valence band as the excited photoelectron are allowed. The majority and minority spins of the valence band contribute opposite signs to the dichroism signal as well. To summarize, the sign of the measured dichroism will be opposite for (i) excitations from different spin-orbit split core levels (the $2p_{3/2}$ and $2p_{1/2}$), (ii) the use right circularly and left circularly polarized X-rays, and (iii) valence band levels filled spin-up electrons and spin-down electrons. Also as a final note, the transfer of photon angular momentum to photoelectron angular momentum has both spin and orbital components. Thus, if the valence band has either a spin or orbital moment it can be detected by the XMCD effect.

For the XMCD spectroscopy used in this dissertation, samples were measured using a 1.5 T (Beamline 6.3.1) or 0.5 T (Beamline 4.0.2) applied magnetic field and circularly polarized X-rays (~60% polarized at Beamline 6.3.1 and ~90% polarized at Beamline 4.0.2). By measuring the sample with X-ray incident along the 90˚ normal angle or at a 30˚ grazing incidence angle to the sample, we can measure element specific information regarding the spin and orbital moment in the sample along the in-plane and out-of-plane directions. In addition, it is possible to measure the element specific magnetization as a function of applied field in the sample by sweeping the magnetic field at a constant X-ray photon energy corresponding to the peak intensity in the dichroism signal.

2.2.5.2. X-ray Natural and Magnetic Linear Dichroism

Dichroism using linearly polarized X-rays, with the X-ray electric field vector pointed along two different crystallographic directions relative to the sample can be used to obtain specific information related to the sample's electronic and magnetic anisotropies. Linear dichroism arises from any non-spherical charge distribution. This distribution can be due to anisotropies in bonding and symmetry of the sample crystal or from a strong spin-orbit coupling which may lead to a deformation (and anisotropy) of the charge density when the material magnetically orders.

To understand the XA process for linearly polarized X-rays, we consider the E-field interaction with the initial state (core) and finals state (valence) electrons. Since the sum of the filled core states results in a spherically symmetric electron density distribution the contribution to the intensity from these initial states is the same for all X-ray E-vector orientations. Thus, the main source for differences in intensity of an XA measurement with linearly polarized light is entirely determined by the spatial distribution (see Figure 10) of the empty valence band orbitals that accept the excited photoelectron (which is excited along the E-vector direction). The XA intensity will be maximum when the E-vector for the linearly polarized X-ray is aligned along the orbital, and it will be zero if the hole density of the valence shell

orbital oriented along the E-vector direction is zero. This effect, absent of any magnetic field contributions to the dichroism, is known as X-ray natural linear dichroism (XNLD). The experimental XNLD set-up used to determine the hole density in the valence band of our samples is shown in Figure 10. By measuring the sample in a 30˚ grazing incident angle, vertical and horizontal linearly polarized X-rays can be used to probe in-plane and (predominantly) out-of-plane hole density, respectively. Under this geometry the difference between vertical and horizontal polarization corresponds to:

$$\begin{aligned} Difference_{grazing\ 30^\circ\ incidence} &= I_{vertical} - I_{horizontal} \\ &= \left(I_{inplane}\right) - \left(I_{out-of-plane}\,(\sin 60)^2 + I_{inplane}\,(\sin 60)^2\right) \\ &= \frac{3}{4} I_{inplane} - \frac{3}{4} I_{out-of-plane} \end{aligned}$$

X-ray magnetic linear dichroism (XMLD) measures the change in the charge anisotropies of the sample induced by exchange and spin-orbit interactions relative to an easy magnetic axis. The effect is induced by uniaxial spin alignment and can be found in both ferromagnets and antiferromagnets below the ordering transition temperature.

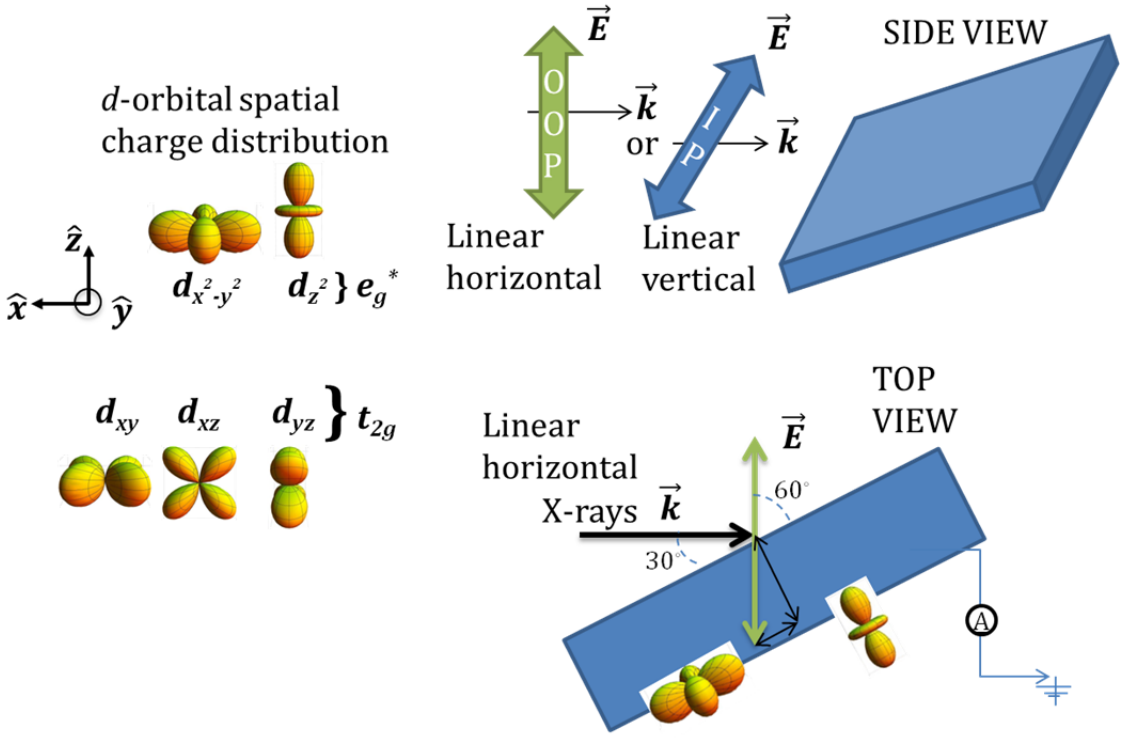

Figure 10 Spatial charge distribution for *d*-orbitals in a cubic octahedral crystal field and geometry of X-ray Linear Dichroism measurement probing spatial charge distribution of valence band holes in grazing incidence

2.2.6. Scanning Tunneling Electron Microscopy/Electron Energy Loss Spectroscopy (STEM/EELS)

Sample microstructure for some samples was probed using Scanning Tunneling Electron Microscopy (STEM) at the electron microscopy center at Oak Ridge National Laboratory (ORNL) in collaboration with Dr. Maria Varela. In this dissertation we employ this microscopy technique to obtain valuable information concerning sample microstructure in cross sectional specimens. In addition, local electronic and chemical information was obtained through Electron Energy Loss Spectroscopy (EELS) in conjunction with STEM.

Conventional transmission electron microscopy (TEM) uses coherently scattered Bragg beams from the electron-beam illuminated sample to produce an image. Because it uses the wavelength of the accelerated electrons (~300 keV), with the proper optics and imaging tools this technique is able to resolve features down to ~1-2 Å. In general, contrast is generated by selecting for the direct beam electrons or the scattered electrons transmitted through the sample [15]. This is done by using an objective aperture to select for electrons coming from the direct beam only (bright field imaging) or the scattered beam only (dark field imaging). The contrast can come from the mass of the atoms, thickness (number of atoms scattering the electrons), or crystalline features in the film (Bragg scattering). High mass and higher density regions in the sample will scatter electrons more strongly than low mass, thinner regions. In bright field imaging, this will cause fewer scattered electrons to make it through the aperture leading to a darker appearance in the image. The reverse is true in dark field imaging mode, since the aperture is placed to select for these higher angle scattering events.

In STEM/EELS an electron beam is rastered (scanned) over a very thin ("electron transparent") sample and a direct beam image is produced (bright field) or a high-angle annular dark-field (HAA-DF) detector is used to preferentially capture a large number of the incoherently scattered beams from the sample to produce a high resolution Z-contrast image [16]. Unlike in conventional TEM, this detector helps to minimize the contrast from coherently scattered Bragg beams from the sample. In this way, the contrast in the image from the sample can be assured to arise from changes in atomic number (Z-contrast) only.

The EELS detector measures the change in the energy of the electrons after scattering with the sample to produce spectra that are produced from following the same dipole selection rules as XA. In EELS the energy loss is also a measure of the electron energy absorption by the sample. The information obtained is similar to XA spectra, the key difference being the use of X-rays or the use of electrons to cause core-valence transitions in the sample. Also in EELS the spectra can be taken from a specific column of atoms in the sample, albeit with lower energy resolution compared to XA spectra.

In performing STEM and EELS measurements, one should always be wary of the imaging of secondary effects from sample preparation or beam induced damage [17]. During sample preparation precaution must be taken to not expose the sample to undesired high temperatures or solvents that could adversely affect the

properties of the electron-transparent TEM sample. These can be introduced during required annealing steps to set adhesives or solvent washing steps to remove excess adhesives. Unwanted properties can also be introduced during the final ion-milling steps, which destructively sputter the film with focused Ar ions in order to obtain a clean and electron-transparent sample.

Beam damage from inelastic collisions used to image the film can typically arise from electron scattering induced bond-breakage, specimen heating from beam exposure and sputtering or atom displacement from the surface of very thin samples. The scattering induced bond-breakage, or radiolysis, in some oxide materials can lead to an anion vacancy paired with a cation interstitial defect by the Knotek-Feibelman mechanism. This mechanism involves the formation of ejected O^+ ions after the Auger emission of oxygen anion electrons due to the decay of a cation electron to a deep core level upon beam irradiation. These can be reduced though not altogether prevented through the use of higher voltages and thinner samples to reduce the chances of electron-electron interactions (sample thickness<mean free path of inelastic electrons) in the film. In insulating materials beam heating can also pose a serious problem, but can be made negligible through the use of thinner samples and higher voltages. In this work, precautions were taken to ensure that samples were thin enough that considerable beam heating did not occur. Sputtering is strongly related to the strength of the bonds in the sample, but with high beam voltages in very thin samples it can occur readily. However, at energies even lower than those needed for sputtering, atoms can still be moved around by the electron beam, especially in the presence of pre-existing vacancies. This makes chemical characterization more difficult. Although high voltage and thin samples can reduce beam heating problems, they can result in damage depending on the source. Thus, in many samples some amount of beam damage is unavoidable. In the images and spectra gathered for this work, we have taken steps to minimize these effects whenever possible.

In summary, STEM can provide much of the same information as conventional TEM, although the images in STEM can be assured to be Z-contrast images. In addition we can simultaneously measure supporting EELS spectra from spatially specific regions in the sample.

In this chapter we have reviewed some of the procedures for growth and characterization used in carrying out our oxide thin film investigations. We have outlined some of the necessary steps that need to be performed to ensure consistent PLD growth from run-to-run. Also, some of the known issues from the characterization techniques (XRD, AFM, RBS, SQUID magnetometry, XA spectroscopy, STEM and EELS that could be a source for inaccuracies and anomalies in our results have been considered so that we can be assured of the data's validity. The atomically precise growth techniques and advanced characterization techniques presented here enable a wide-range of studies, and are well-suited for our endeavors. These techniques are quite powerful and with each new generation of the instruments used for the types of growth and characterization techniques

presented here, we will be able to pave the way for the coming era of new advanced materials with novel functional properties.

Chapter 3: Structural Effects from Epitaxy

3.1. Growth and structural characterization of epitaxially strained $LaCoO_3$ films

3.2. Stabilizing tetragonally-distorted $LaCoO_3$ films using coherent epitaxial strain

3.3. Oxygen vacancy ordering in STEM/EELS

3.4. Oxygen dependence studies

3.5. Summary

Abstract

The goal of this chapter is to demonstrate the structural modifications possible through heteroepitaxy and the effects of stoichiometric deviations from the bulk equilibrium structure. In particular, we show the successful structural manipulation using epitaxy in the LCO system. I demonstrate the degree of control over the LCO structure that is possible via hetero-epitaxy on various substrates by growing films of different thicknesses and under different growth conditions. The microstructural details observed using STEM and EELS attest to the defect related changes that strain can cause in the film. The effects of hetero-epitaxy on the magnetic and electronic structure will be discussed in chapters 4 and 5.

Chapter 3: Structural Effects from Epitaxy

3.1. Growth and structural characterization of epitaxially strained $LaCoO_3$ films

LCO films were grown on STO, LSAT, and LAO substrates under similar conditions in a large range of thicknesses (8 nm - 133 nm thick) using pulsed-laser deposition with a 248 nm KrF laser (~1 J/cm^2) pulsed at 3 Hz. A comparison of the lattice mismatch for these film and substrate materials is given in Figure 11. Films grown on STO and LSAT impart tension in-plane and films on LAO impart compression in-plane. Films on STO have the largest lattice mismatch of ~2.4%.

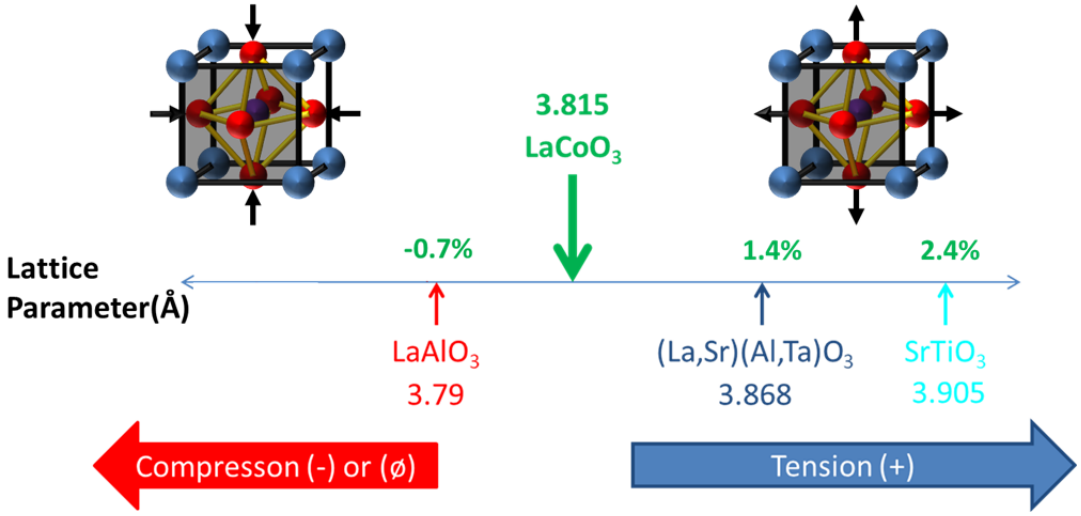

Figure 11 Growth schematic showing different epitaxial strain conditions for $LaCoO_3$ films grown on single crystalline oxide substrates. Percentages shown on the line are the lattice mismatch values between substrate and film lattice parameters.

The films were grown at 700˚C in 320 mTorr of O_2 and cooled in an atmosphere of 1 Torr of O_2. Thicknesses were determined using X-ray reflectivity, and the structure of the films was determined by X-ray diffraction. 15 nm and 75 nm thick samples on LAO, LSAT, and STO substrates were measured at Oak Ridge National Laboratory using high resolution Scanning Tunneling Electron Microscopy (STEM) and Electron Energy Loss Spectroscopy (EELS) to obtained more detailed local structural and chemical information. Finally, a set of films was grown in a range of oxygen growth pressures (10 mTorr-320 mTorr) on LAO, LSAT, and STO to further study the structural effects of non-stoichiometry in the film.

3.2. Stabilizing tetragonally-distorted $LaCoO_3$ films using coherent epitaxial strain

After growth, detailed information on the films' crystallinity and in-plane and out-of-plane lattice parameters were determined using X-ray diffraction. The

crystalline quality was assessed by the ω rocking curve measurements. In Figure 12, the $\Delta\omega$, or full-width half maximum (FWHM), was used to compare 8 nm-133 nm thick films on STO (Figure 12(a)) and LAO (Figure 12(b)) substrates. For films on STO the crystallinity is excellent below 50 nm thick, and AFM confirms smooth surfaces with RMS <0.3 nm. At greater thicknesses on STO the mosaic spread increases considerably, as films tend to crack during cooling, possibly from the thermal expansion mismatch between STO and LCO [1]. The formation of twin boundaries in LAO is well known to occur at the growth temperatures used in this study (700˚C). In the 8 nm sample, two peaks are visible in ω for the LCO film. This is a result of the underlying LAO twin structure. Regardless, the mosaic spread within each twinned grain appears to be relatively low ($\Delta\omega$~0.126˚). The crystallinity worsens at a lower thickness compared to STO (broadening at 30 nm, instead of 50 nm), possibly due to increased formation and migration of twin boundaries in LAO with increased exposure to high temperatures during the longer growth times. The 002 film peak overlaps with the substrate peak in the θ-2θ measurements for LCO films on LAO above 70 nm thick, making an accurate determination of the crystallinity difficult for these thicknesses. In general, the crystalline quality decreases with increasing film thickness.

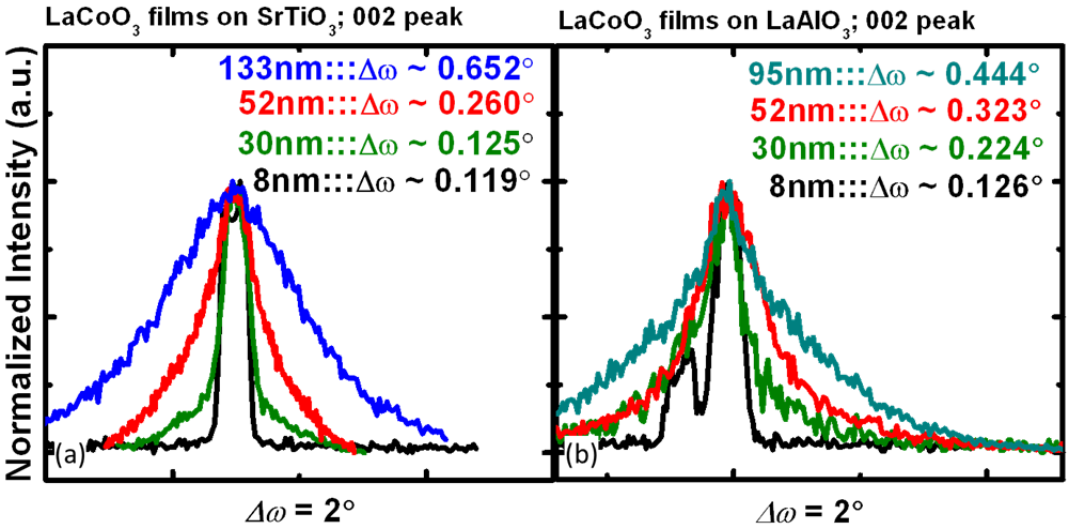

Figure 12 ω rocking curves measured for the 002 film peak to assess the mosaic spread in the films on (a) STO and (b) LAO. The mosaic spread increases with increasing thickness.

The θ-2θ X-ray diffraction measurements on the 002 peak (Figure 13) reveal that structure evolves toward a relaxed bulk-like LCO structure as a function of increasing thickness. The thinnest films (6 nm and 8 nm) show broad, low intensity peaks due to the low number of diffracting planes in these samples (fewer constructive interference scattering events). As a result we have difficulty obtaining accurate lattice parameter values for these thicknesses. The 2θ values (and lattice parameters) in the figure were obtained after fitting a Gaussian to the film peaks and using the Gaussian peak position. The high crystallinity is confirmed in the 15

nm and 33 nm films by the presence of thickness Kiessig oscillations generating satellite peaks on either side of the Bragg peaks. In films 75 nm and thicker the film peaks are obviously broadened indicating that the film structure takes on a range of out-of-plane lattice parameters as the film tends to relax. 15 nm thick films show out-of-plane lattice parameters significantly changed relative to bulk ~3.81 Å. Films on LAO (Figure 13(c)) show a larger out-of-plane lattice parameter ~3.85 Å while films on LSAT (Figure 13b)) and STO (Figure 13(a)) have out-of-plane lattice parameters depressed with respect to bulk LCO with values of ~3.80 Å and ~3.77 Å. Thicker films on LAO and STO show out-of-plane lattice parameters that clearly relax toward bulk LCO. Intriguingly, out-of-plane peaks for thick films on LSAT do not show an obvious shift in 2θ but broaden with increasing thickness, suggesting that even with these higher thicknesses a large portion of the film maintains epitaxial strain.

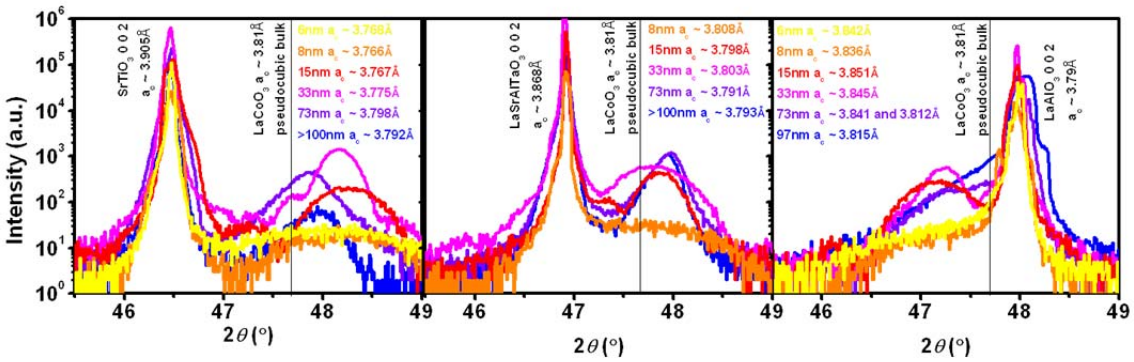

Figure 13 θ-2θ rocking curves around 002 peak showing evolution of out-of-plane lattice parameter as a function of thickness.

To better understand the overall structural changes as a function of thickness on the different substrates, we compared reciprocal space maps (RSMs) taken at the 013 peak for ~15 nm and 95 nm thick films (Figure 14). Thin films on all three substrates have sharp uniform peaks showing an increased (decreased) in-plane and a decreased (increased)out-of-plane lattice parameter on STO and LSAT (LAO) with respect to bulk LCO (Figure 14 green circle), consistent with the θ-2θ measurements in Figure 13. Thick films all show different degrees of partial relaxation of the film peak towards bulk LCO values, with films on LSAT (LAO) appearing least (most) relaxed. This partial relaxation suggests that the appearance of a constant out-of-plane lattice parameter as a function of increasing thickness from the θ-2θ measurements on LSAT is misleading. LSAT films are in fact relaxing, though to a lesser degree compared to STO and LAO films. In addition, all thick films show a severely broadened peak indicating increases in the mosaic spread and lateral correlation length in the film, consistent with our observations from ω scans (Figure 11).

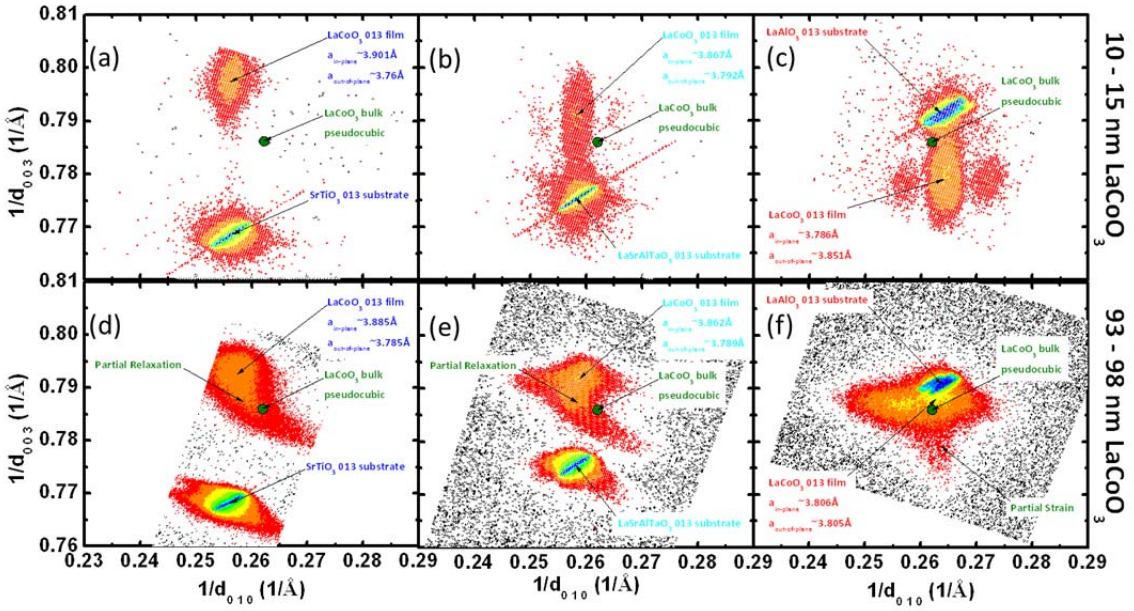

Figure 14 Reciprocal space maps showing 013 peak reflections for the ~15 nm and ~100 nm films grown on STO, LSAT, and LAO.

The in-plane (open squares) and out-of-plane (closed squares) lattice parameters for the 15 nm, coherently strained films on all three substrates are summarized in Figure 15. The ratio of out-of-plane lattice parameter to in-plane lattice parameter (c/a) of the LCO film is calculated for growth on different substrates. As thickness is increased, the LCO films evolve from a tetragonally distorted lattice to one approaching c/a ~1. Thus, through an appropriate choice of substrate and thickness, films can be grown with various aspect ratios. We achieve c/a ~1.014 with coherently strained films in compression on LAO, and c/a ~0.978 and c/a~ 0.968 for the comparable films strained in tension. The crossover from c/a >1 to c/a <1 occurs at 3.82 Å which is slightly higher than the bulk pseudocubic value of LCO ~3.81 Å.

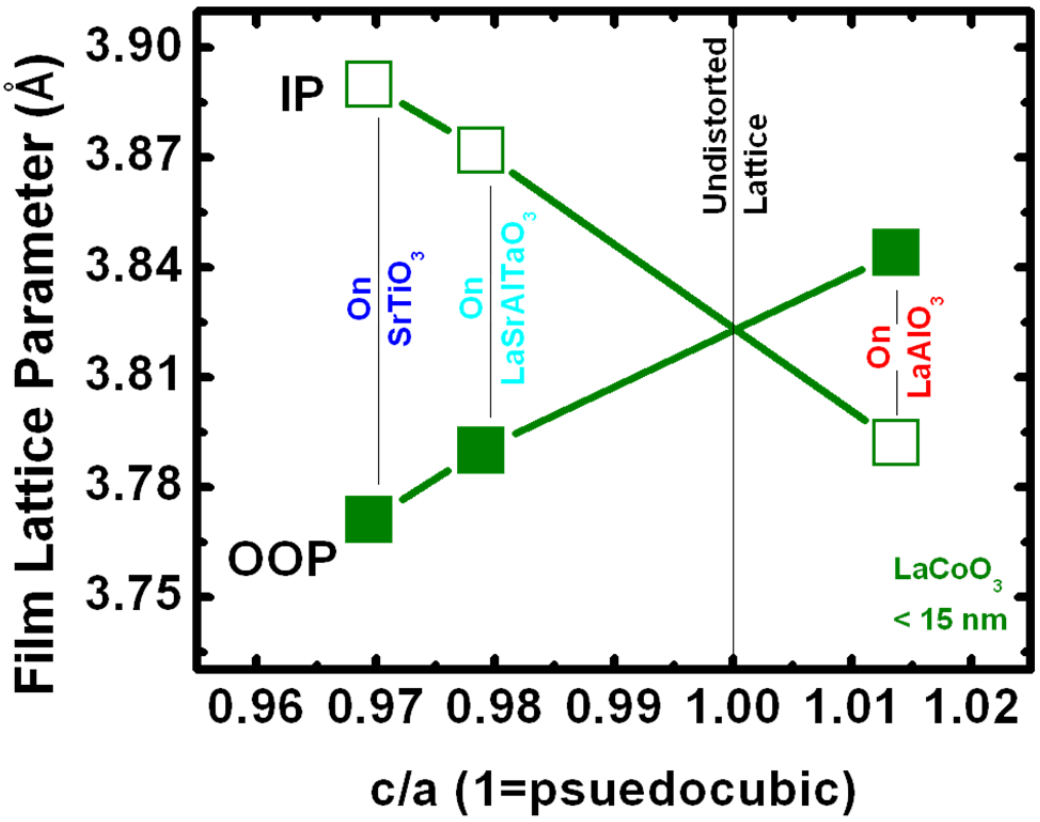

Figure 15 Summary of tetragonal structures stabilized in coherently strained 15 nm thick films.

We also gauged whether the unit cell volume was preserved in these distorted films by comparison to bulk LCO unit cell volume (55.306 Å^3). Table 1 lists average value for in-plane and out-of-plane lattice parameters (obtained from RSMs) for three sets of coherently strained films grown less than 15 nm thick. In the final three columns we assess the volume change, tetragonal distortion, and ratio of volume change to tetragonal distortion using the components of the strain tensor that correspond to these changes in in-plane and out-of-plane lattice parameters. For these calculations we have assumed $\varepsilon_{xx} = \varepsilon_{yy}$, since the films are grown on 001 substrates. We find that films on LSAT and STO which show significant tetragonal distortion ($2\varepsilon_{zz}-\varepsilon_{xx}-\varepsilon_{yy}$, seventh column) also show some degree of volume change ($\varepsilon_{xx}+\varepsilon_{yy}+\varepsilon_{zz}$, sixth column). Films compressively strained on LAO only show a large change in the tetragonal distortion, while the volume changes very little.

The final column in Table 1 gives a quantity that allows us to assess how much the volume changes for a given quantity of tetragonal distortion. Remarkably, we find that despite the smaller tetragonal distortion for films on LSAT compared to STO, the corresponding volume change is the largest. This shows that there is a difference between the modes by which strain is accommodated in films on LSAT compared to films on STO, and suggests that either (i) the octahedral rotations in films on LSAT result in a greater increase in the Co-O-Co bond angles compared to

films on STO or (ii) there is an increased presence of other defects that increase the volume of the average unit cell in these films compared to films on STO.

Table 1 Average structural values determined from X-ray diffraction reciprocal space maps for three different sets of films <15 nm thick. All values aside from the first two columns are calculated values.

Substrate (001)	IP (Å)	OOP (Å)	c/a	V (Å^3)	ΔV or $\varepsilon_{xx}+\varepsilon_{yy}+\varepsilon_{zz}$ (%)	$2\varepsilon_{zz}-\varepsilon_{xx}-\varepsilon_{yy}$ (%)	$\varepsilon_{xx}+\varepsilon_{yy}+\varepsilon_{zz}$(%)/ $2\varepsilon_{zz}-\varepsilon_{xx}-\varepsilon_{yy}$ (%)
STO	3.899	3.767	0.965	57.256	3.53	-7.02	-0.503
LSAT	3.871	3.790	0.979	56.802	2.70	-4.27	-0.632
LAO	3.79	3.845	1.015	55.242	-0.11	2.93	-0.023

3.3. Oxygen vacancy ordering in STEM/EELS

While X-ray diffraction suggests that the epitaxial strain is accommodated in the film through changes in bond-length or coordinated octahedral rotations to expand or contract the lattice in a given direction, scanning tunneling electron microscopy reveals microstructural details that suggest the strain may be accommodated through structurally ordered changes in oxygen stoichiometry (Figure 16). Ordered linear planes of dark contrast were found on 15 nm thick samples on LAO, LSAT, and STO. These dark contrast planes appeared perpendicular to the substrate-film interface in films on LSAT (Figure 16(b)) and STO (Figure 16(c)) and parallel to this interface in films on LAO (Figure 16(a)). Also, the dark contrast planes' occur periodically after every 3-4 bright contrast planes on STO and LAO, and after every 2-3 bright contrast planes on LSAT. Similar dark contrast planes have been observed in other Sr-doped cobaltite films and have been attributed to oxygen vacancies [2, 3, 4], cation vacancies [5], and structural twinning [6, 7].

Figures 16(d, e, f) show the O-K edge EELS line scan spectra taken along the dark (black line) and bright (red line) contrast planes. The spectral differences between bright and dark contrast planes are easily discernible on LAO and STO. By contrast, the spectral differences between dark and bright contrast planes on LSAT are difficult to discern because of the large number of dark contrast planes in this sample and the limited spatial resolution of the EELS line scan. In general, the bright contrast planes have higher O-K edge intensities. Films on LAO and STO show an obvious shoulder peak at ~527 eV. The dark contrast planes also have a higher L_3/L_2 peak intensity ratio at the Co-L edges (Figure 16(g, h, i)). These spectral differences between bright and dark contrast planes suggest that the dark contrast planes are oxygen deficient planes of ordered oxygen vacancies. Thus, LSAT films contain the most vacancies, followed by STO, while LAO has the fewest vacancies.

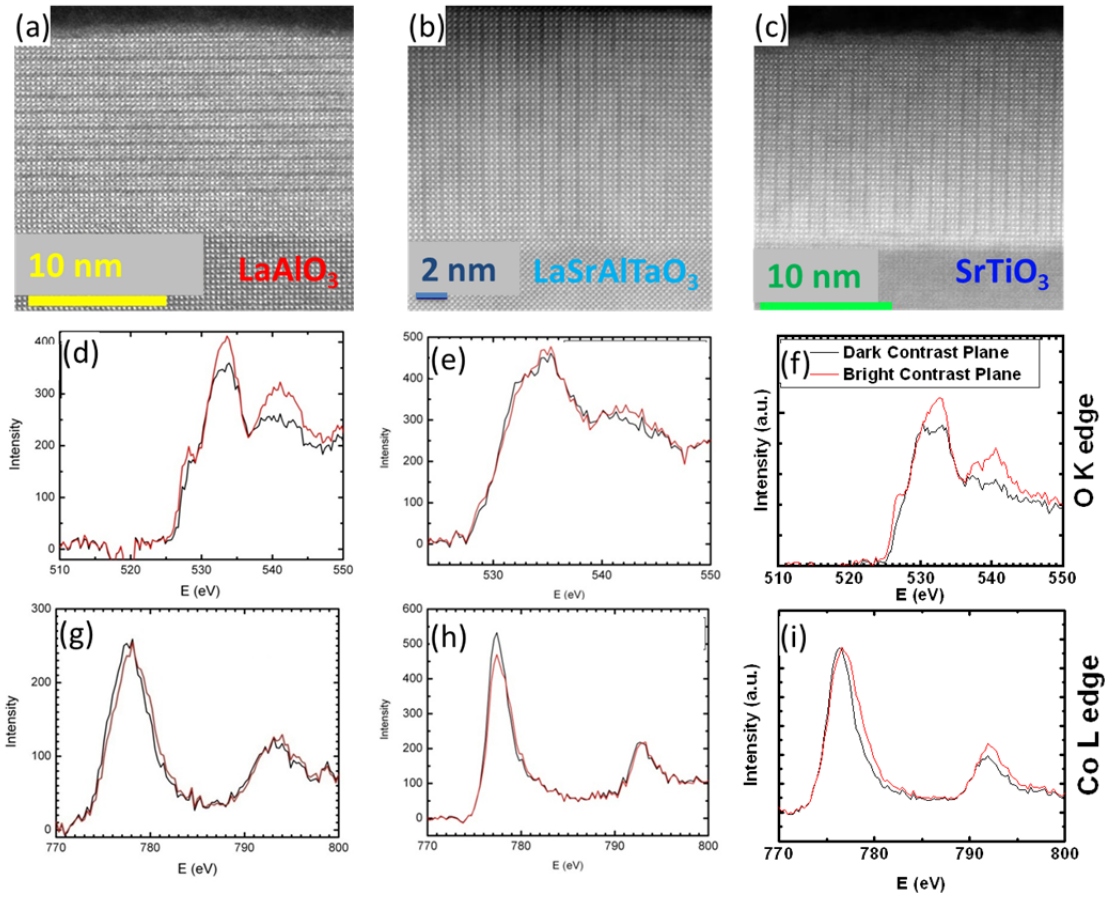

Figure 16 Scanning tunneling electron microscopy images in bright field imaging mode showing periodic dark contrast planes parallel and perpendicular to the substrate-film interface for ~15 nm thick films of $LaCoO_3$. Co-L edge (g, h, i) and O-K edge (d, e, f) EELS spectra from line scans taken along the bright (red) and dark (black) contrast planes in dark field imaging are shown below the corresponding images.

Oxygen vacancies often result in expansion of the lattice [8] and may aid in alleviation of tensile stresses in the film from epitaxial strain [3, 4]. The periodicity and orientation of the vacancy planes indicate that the vacancies are arranged in the film to relieve the stresses from growth on STO, LSAT, and LAO. Thus vacancies fill the elongated directions in the film: in-plane for films on STO and LSAT, out-of-plane for films on LAO.

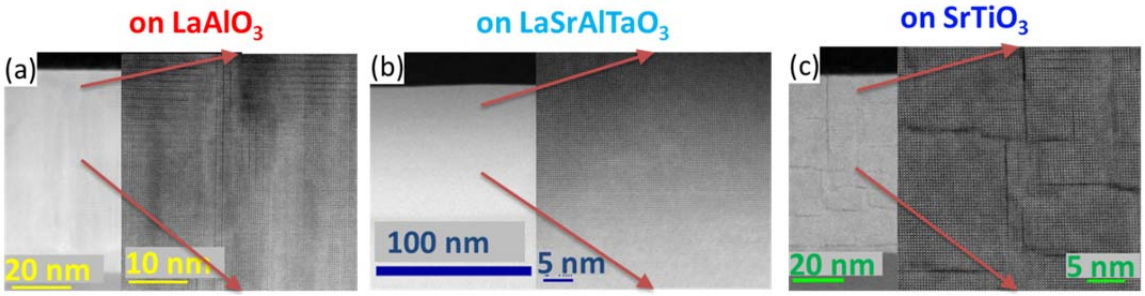

Figure 17 Scanning tunneling electron microscopy images taken in bright field imaging for 75 nm thick films.

The density of dark contrast planes decreases in the thicker LCO films, which also suggests that the oxygen vacancy ordering is strain related. STEM in Figure 17 shows that in addition to a decrease in density of dark contrast vacancy planes, the vacancy plane orientation is more disordered. Vacancy planes oriented along both in-plane and out-of-plane directions can be observed in 75 nm films grown on LAO and STO. By contrast, the 75 nm thick film on LSAT does not show clear evidence of vacancy ordering.

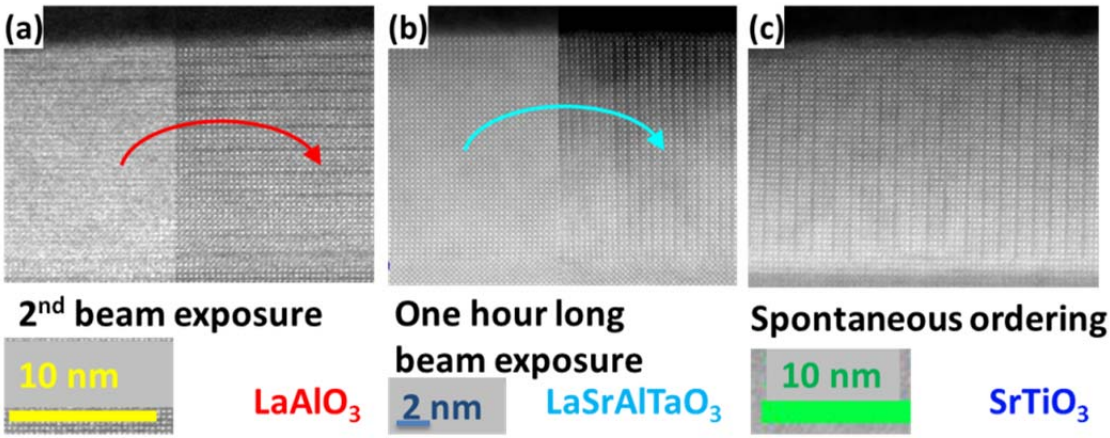

Figure 18 The presence of oxygen vacancy ordered planes after effects from beam exposure in films on LAO, LSAT, and STO.

As a final note, it may be important to mention that observation of these defect planes does not always occur, and appears to be affected by certain unknown variable conditions related to sample prep, sample charging, electron beam exposure, or properties intrinsic to LCO samples. In Figure 18, films on LAO and LSAT show evidence that the defect ordering appears more pronounced after electron beam exposure. This suggests that these stoichiometric defects are always present in the sample, but order under electron beam irradiation. The relative speed with which the defects organize into planes may be related to the mobility of such defects in films grown on LAO, LSAT, and STO. This suggests that these oxygen vacancies migrate easily in films on STO (where the defect planes are almost always

observed without need for increased beam exposure time), and with some difficulty in films on LSAT (where the ordering is only observed after >1 hour of electron beam exposure). This also suggests that these defects are migrating in the sample to regions that are high strain or space-allowing [3, 4], considering the larger radial size associated with these defects (oxygen vacancy or Co^{2+}).

3.4. Oxygen Dependence studies

Since the microstructural features observed in the films suggest a strong presence of oxygen vacancies, we explored the role of oxygen deposition pressure on the film structure. We grew ~30 nm thick films on LAO, LSAT, and STO in 10 mTorr- 320 mTorr of O_2. Films grown in the lower oxygen pressures tend to be slightly thicker and smoother (lower RMS roughness) due to reduced scattering of the plume with oxygen background gas during growth. However, the crystallinity does not appear to change significantly with oxygen pressure. Figure 19 shows the normalized $\Delta\omega$ rocking curve scans for films grown on LSAT in 20 mTorr, 70 mTorr, and 200 mTorr of oxygen taken for the 002 film diffraction peak. Despite the changes in oxygen growth pressure, the crystallinity remains high ($\Delta\omega < 0.1^{\circ}$) and similar to the other films of comparable thickness. Similar trends were observed for films on STO and LAO.

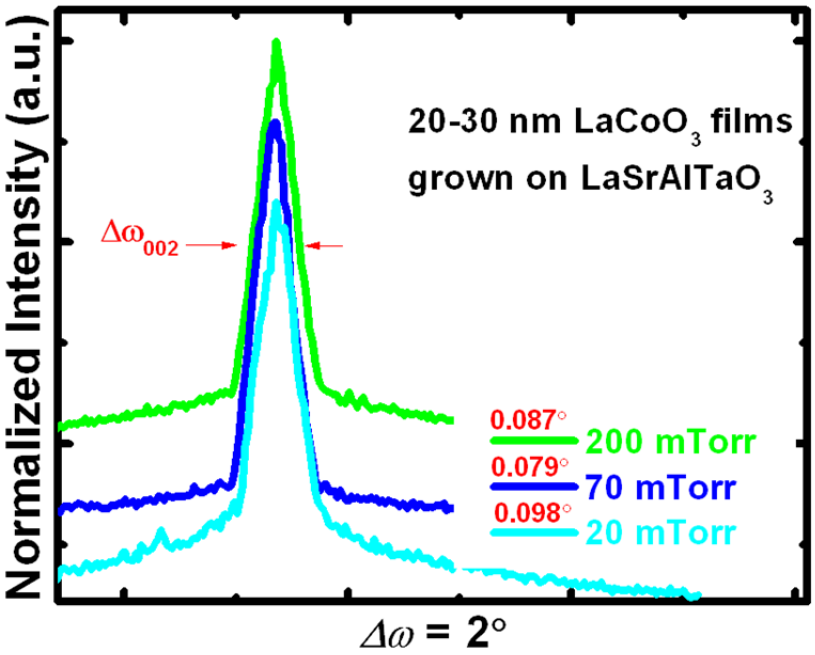

Figure 19 $\Delta\omega$ for ~30 nm thick $LaCoO_3$ films grown on LSAT. No change in the FWHM is observed over the oxygen pressure range studied.

The out-of-plane lattice parameter was found to be significantly increased in all films grown at 10 mTorr compared to films grown in 320 mTorr. Figure 20 shows the out-of-plane lattice parameter changes measured for the films grown on

all three substrates. Above 100 mTorr the out-of-plane lattice parameter changed only slightly showing the smallest values at 320 mTorr. Under epitaxial strain conditions for a stoichiometric film, we expect the out-of-plane lattice parameters for film in tension (LSAT and STO) to be less than LCO bulk (~3.81 Å) and for films in compression (LAO) to be greater than LCO bulk. The structure of films well above 75 mTorr changes as we might expect for stoichiometric films under epitaxial strain. The small changes to structure under increasing pressure beyond 75 mTorr suggest that even with 320 mTorr of O_2 the films may not be fully stoichiometric, although the lattice parameter appears to level off in this range. Despite these differences, the similar $\Delta\omega$ suggests that the structural changes are accommodated without loss in the overall crystalline quality of the film.

The in-plane lattice parameters did not change between the 10mTorr and 320mTorr 30 nm thick film samples, indicating that all structural changes resulting from O_2 pressure changes occur in the out-of-plane direction. Figure 21 shows the RSMs for strained 30 nm films on STO grown in 10 mTorr and 320 mTorr. Apart from the change in the out-of-plane lattice parameter, no change is observed in the structure of the film. Relaxed films on LAO show a similar expansion exclusively in the out-of-plane lattice parameter with decreasing oxygen growth pressure.

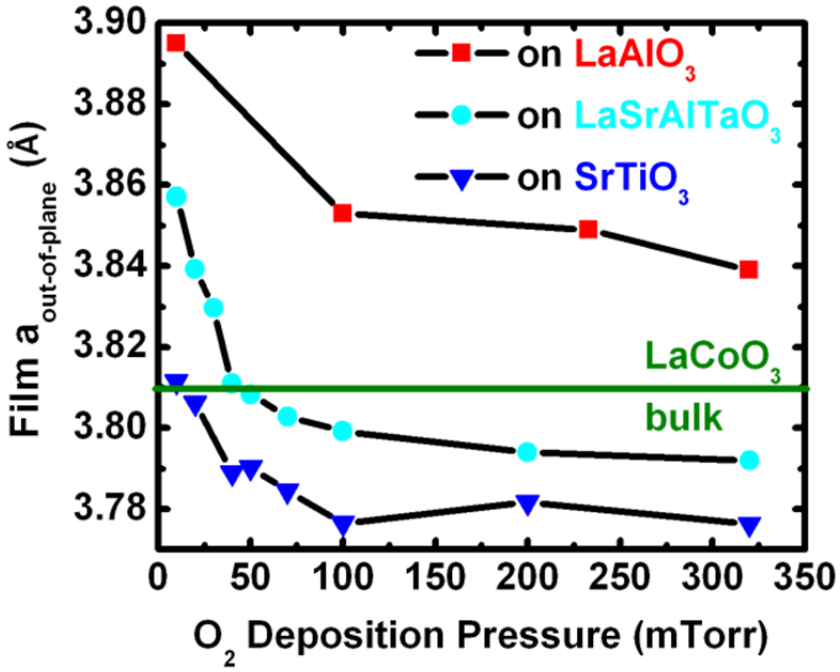

Figure 20 Change in out-of-plane lattice parameter with changes in oxygen growth pressure. The out-of-plane lattice parameter is lowest in the 320 mTorr samples.

The LCO unit cell volume increases as a function of decreasing oxygen deposition pressure, which may be explained by the presence of oxygen vacancies at lower oxygen deposition pressures [8, 9]. Oxygen vacancies may arise to preserve equilibrium during the deposition process; the loss of the neutral oxygen atom

leaves extra electrons that may hop to nearby Co^{3+}, forming larger Co^{2+} cations which in turn expand the lattice. Additional lattice expansion can occur from displacements of nearby atoms to accommodate the oxygen vacancy site, with cations displacing away from the site and oxygen ions displacing towards the vacancy site [8]. These lattice expansions and atomic displacements have significant implications in the magnetic ordering due to their effect on the Co-O-Co magnetic exchange mechanism.

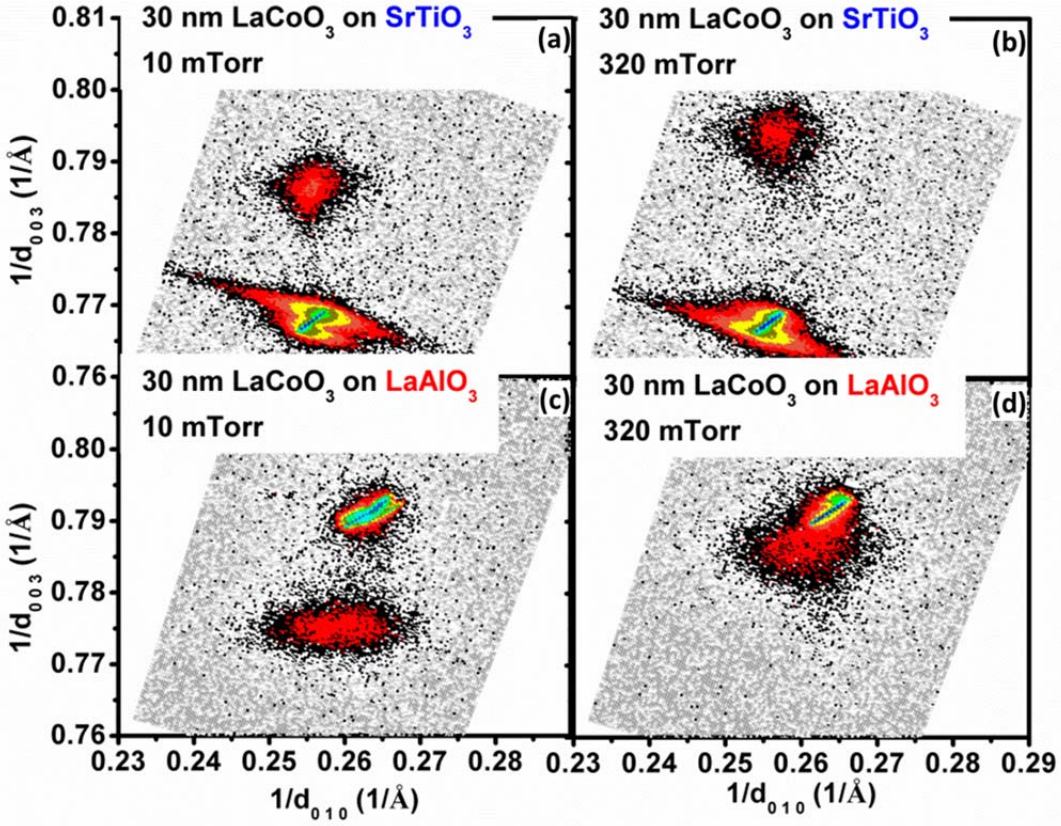

Figure 21 Reciprocal space maps for films grown on STO and LAO in 10 mTorr and 320 mTorr of oxygen. LAO 30 nm films are relaxed and STO 30 nm films appear to be strained at these thicknesses.

3.5. Summary

In this chapter we have shown that the choice of a lattice mismatched substrate is effective in altering the structure of thin LCO films. At thicknesses of ~35 nm and beyond the film structure appears to show evidence of lattice relaxation towards bulk LCO values ~3.81 Å in both in-plane and out-of-plane directions. While XRD suggests that bond lengths and octahedral rotations may be responsible for the changes in structure in LCO, STEM suggests that the substrate induced tensile stresses and strains may be accommodated by nucleation of ordered defect planes along the elongation direction in the film. On the other hand, attempts to introduce oxygen-related defects in the film through changes in oxygen growth pressure show that the defects cause changes in the out-of-plane lattice parameter

only, even in relaxed films on LAO. This is surprising since in STEM we have observed oxygen vacancies can be accommodated in both in-plane (STO and LSAT) and out-of-plane (LAO) directions, but defects from oxygen induced growth may only be occurring in the out-of-plane directions. In the next chapter these structural changes are related to trends in the magnetic behavior of LCO films. Detailed analysis of the electronic structure of the LCO films will be presented in the next chapter to better illustrate the connection between strain and ferromagnetism.

Chapter 4: Inducing ferromagnetic exchange in epitaxial $LaCoO_3$

Abstract

In this chapter the surprising observation of ferromagnetism in epitaxial $LaCoO_3$ thin films not present in bulk $LaCoO_3$ is demonstrated. In order to understand the possible origins of long-range order in LCO films, magnetism is correlated with (i) epitaxial strain, (ii) stoichiometry, and (iii) microstructure. A simple model is developed to help explain how the modifications of electronic structure in the films, caused by epitaxial strain and non-stoichiometry can give rise to spin state transitions and in turn stabilize a ferromagnetic ground state. I find that coherently strained films in tension have the highest moment while coherently strained films in compression are not magnetic. Analysis of the microstructure reveals that a greater number of oxygen defects are found in films with a higher magnetic moment. XA reveals that the differences between films grown under different conditions are associated with various fractions of HS Co^{2+}, HS Co^{3+}, and LS Co^{3+}. XMCD and XNLD show that the features in the electronic structure are associated with the magnetism and the growth under different conditions. Films grown in lower oxygen growth pressures have suppressed magnetic order.

Chapter 4: Inducing ferromagnetic exchange in epitaxial $LaCoO_3$

Our efforts to manipulate the spin state through heteroepitaxial strain (Chapter 3) have resulted in ferromagnetic films of LCO. This result suggests that epitaxial strain is indeed a viable tool for controlling the spin state in LCO; however, the possible role of defects induced during growth cannot be neglected. In fact, determining the precise source of ferromagnetism is still an open question in cobaltite thin films [1, 2]. Many groups cite the importance of epitaxial strain [3, 4, 5], while others have implicated the role of chemical inhomogeneity [1, 2, 6]. In all instances, a cohesive explanation of the precise exchange mechanism underlying the ferromagnetism between high spin and low spin cobalt or cobalt in different valence states, has yet to be presented. In particular, scientists currently have little understanding regarding the specific differences between films grown under different conditions that explain the differences in magnetic moment. More work needs to be done to firmly establish whether the Co spin state or the valence state is more closely involved in the ferromagnetism. To accomplish this, we carry out a more thorough determination of the structural and stoichiometric make-up of the different magnetic and nonmagnetic LCO films. By exploring the relationship between magnetism, strain, and stoichiometry in detail using microstructure and electronic structure characterization, we uncover the crucial building blocks needed to explain the long-range magnetic order in this system.

4.1. Substrate and strain dependence studies

Due to some of the confusion in the literature regarding the magnetism dependence found for films grown on different substrates [3, 4, 7], it is necessary to properly establish the relationship between magnetism and strain. The trends related to the thin and thick LCO films grown on different substrates indicate that the ferromagnetism is a result of epitaxial strain in tension. However, a closer look at the growth on the different substrates and to different thicknesses show that increasing the strain does not necessarily equate to higher magnetic moments. Figure 22 shows the SQUID magnetometry results for films grown ~15 nm thick (labeled as "strained") and 75 nm thick (labeled as "relaxed") on STO, LSAT and LAO substrates. Recalling the structural information from Chapter 3, we know the structure of these films shows varying amounts of tetragonal distortion and volume change dependent on the thickness and the lattice mismatch of the substrate used to induce epitaxial strain. The presence of ferromagnetism is consistently found in films strained in tension. Figure 22 shows that coherently strained films in tension on LSAT and STO both show evidence of ferromagnetic order. However, it is interesting that 15nm films on LSAT, which are less strained in tension (compared to films on STO), have the highest saturated moment of ~2.15 μ_B/Co (Figure 22(b)). By increasing the tetragonal distortion and epitaxial strain by growth on STO, we find a lower saturated moment of ~0.85 μ_B/Co (Figure 22(a)). On the other hand, 15 nm thick films strained on LAO do not show obvious indications of ferromagnetic hysteresis (Figure 22(c)) or Curie temperature (Figure 22(d)) indicating that

strained films grown in compression on LAO do not show signs of long-range ferromagnetic order and that epitaxial strain in tension does play a role in the ferromagnetism.

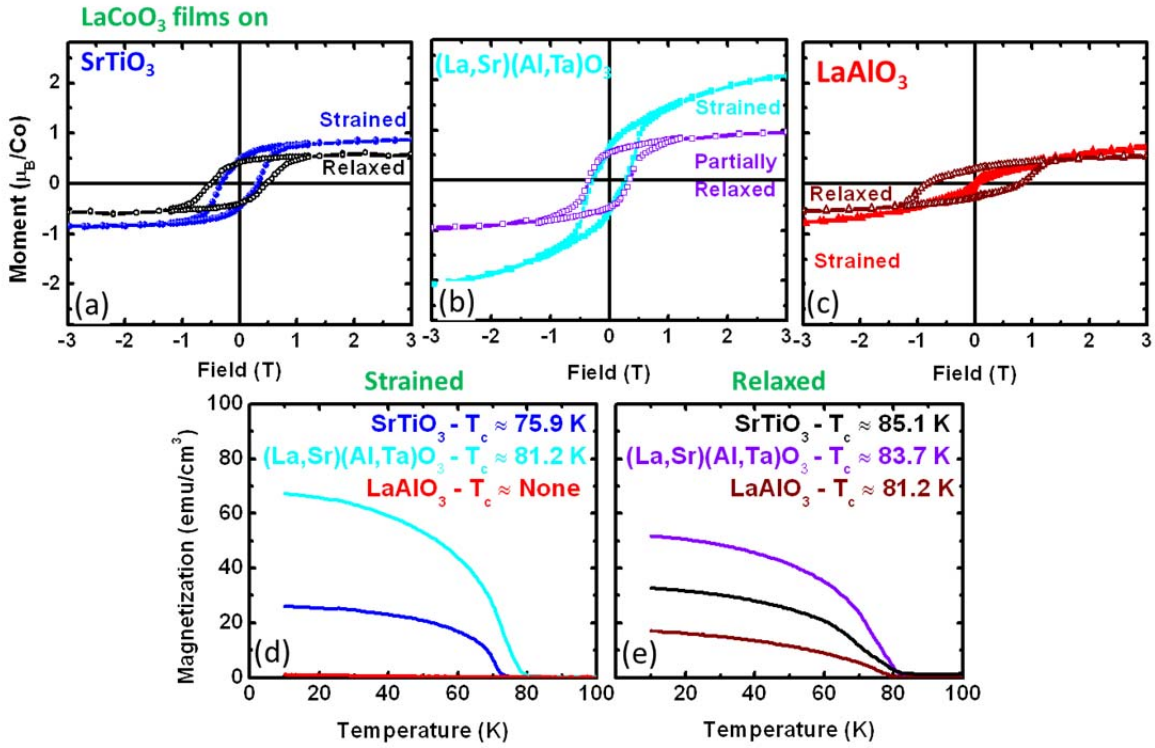

Figure 22 Magnetization vs field measurements at 5 K for thin (dark) and thick (light) LCO films grown on (a) STO, (b) LSAT, and (c) LAO substrates showing a range of saturated moments. The magnetization vs temperature measurements under H=5 mT (FC) for (d) strained and (e) relaxed films show a Curie temperature below ~85 K for all films except strained films on LAO.

In contrast, all ~75 nm thick films show ferromagnetic behavior below ~85 K. For the films on LAO and STO at these thicknesses, the relaxation in the coherently strained 15 nm film structure results in a comparatively lower net moment. However, just as we observed in the trends for 15 nm thick films, even in these 75 nm thick samples, LCO on STO has a lower moment (~0.6 μ_B/Co) compared to LCO films on LSAT (~0.95 μ_B/Co). Figure 23(a) shows how the saturated moment on STO decreases as a function of increasing thickness. Surprisingly, while the coherently strained films in compression on LAO did not show any magnetism, relaxation of the epitaxial strain on thicker films resulted in ferromagnetic ordering. In these thicker films, although the strain and tetragonal distortion is presumably much smaller, the magnetism is greater. This suggests that additional factors besides strain need to be considered in explaining all the details of the ferromagnetism. The trend of increasing remanent moment with increasing thickness is plotted in Figure 23(b) for LCO films on LAO. The remanent moment is plotted instead of saturated moment to thickness, due to the difficulty in determining the saturated moment for very thin nonmagnetic films.

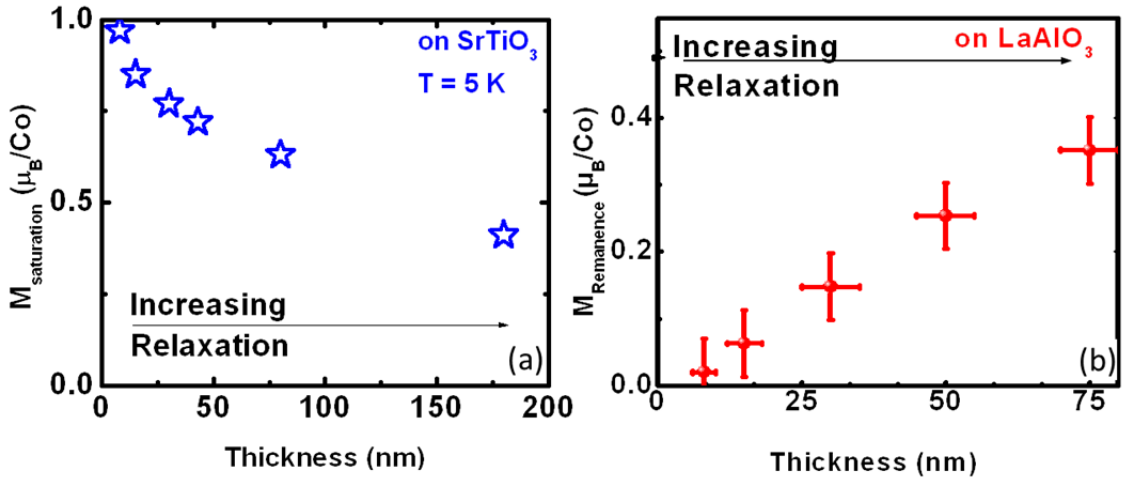

Figure 23 Magnetism trends as a function of thickness showing that films on STO and films on LAO display an opposite trend. For films on (a) STO the saturated moment is plotted as a function of thickness. For films on (b) LAO the remanent moment is plotted as a function of thickness instead.

These results show that films grown coherently strained in tension clearly result in long-range ferromagnetic order below ~85 K. However, the details of the relationship between magnetism and growth on different substrates suggest that more film properties need to be investigated to explain all the trends. The decrease in overall magnetic behavior in thick films on STO and LSAT might be expected due to the structural relaxation towards bulk lattice parameter values. This leads us to believe that strain gives rise to ferromagnetic order in LCO films. In the 75 nm thick films on STO and LSAT the lower net moment can be attributed to some mixture of relaxed film and film still strained to the substrate. However, if we consider that bulk LCO at these temperatures is mostly composed of diamagnetic LS Co, the evidence of ferromagnetism in the relaxed films on LAO is surprising. This suggests that though the lattice parameters in the relaxed LCO film on LAO appear to be similar to bulk LCO, the defects and stoichiometry are not similar and give rise to long-range ferromagnetic order. Also surprising is the presence of higher moment in coherently strained films grown on LSAT compared to more tensily strained films grown on STO. If the magnetism were purely strain related, more highly strained films on the larger lattice-mismatched substrate, STO, would have the highest moment. Since LSAT has the highest magnetic moment, additional sources must contribute to the magnetism.

4.2. Micro-structure / Electronic structure

The discussion so far suggests that multiple factors contribute to the generation of ferromagnetism. However, from chapter 3 we also know that the microstructure of films grown on STO, LSAT, and LAO show intriguing differences which may be related to the changes in magnetism. For greater understanding of the

role of epitaxial strain and defects, we explore the connection among the electronic structure and the microstructure using STEM and EELS measurements, (as described in Chapter 3) and the magnetism. By examining the electronic structure in detail using XAS, XMCD and XNLD measurements, we can explore the specific elemental contributions to the electronic structure and gain more insight into the sources of magnetism in these samples.

4.2.1. STEM/EELS

The presence of ferromagnetism in tensilely strained LCO films, and not in compressively strained ones less than 15 nm thick, indicates that epitaxial strain induces lattice distortions which play some role in stabilizing ferromagnetism. However, the presence of defects observed in STEM and EELS also associated with growth on different substrates suggests that a careful consideration of the role of the microstructure is in order. The STEM images from chapter 3 show that in 15 nm thick films there are a large number of oxygen vacancies and likely a considerable number of Co^{2+} ions distributed throughout the films. Their magnitude (as suggested by their orientation) is related to the substrate induced strain in the films and may also have effects on the magnetic ordering. We have assumed that films with defects oriented parallel to the film plane have a fewer total number of defects since they only occur up to the thickness of the film. Films with defects perpendicular to the substrate-film interface likely occur in much greater numbers since they extend across the entire lateral length of the sample. For example, 15 nm films on LSAT which have the highest magnetic moment also show the most defects, as indicated by their occurrence every 2-3 unit cells perpendicular to the film plane. 15 nm films on STO which have slightly fewer oxygen defect planes (every 3-4 unit cells perpendicular to the film plane) have a lower moment compared to films on LSAT. Finally, 15 nm films on LAO which have the fewest oxygen defect planes occurring along the film plane every 3-4 unit cells do not show ferromagnetic order. The correlation between the number of oxygen defect planes and the magnitude of magnetism in the 15 nm thick films suggests that their presence plays a role in the magnetism.

Supporting this trend, we observe that the changes in abundance of defect planes with thickness may also be related to the changes in moment with increasing film thickness for the films in compression and tension. For example, while in 15 nm films on LAO only defect planes parallel to the substrate-film interface are observed, in 75 nm films the planes appear both parallel and perpendicular to this interface, suggesting an overall increase in the total number of defects, in the thicker LAO films. The increased magnetism in thicker LAO film, suggests that there is a connection between magnetism and the greater number of defects oriented perpendicular to the film plane. The trends observed with increasing thickness in films on LSAT and STO also support this view. The 75 nm film on STO show fewer defect planes perpendicular to the film plane and more defect planes parallel to the film plane, representing a net decrease in the number of defects. In the 75 nm film on LSAT, we do not observe any defect planes. Thus, in contrast to films on LAO,

thicker films on STO and LSAT show a decrease in defect planes perpendicular to the film plane, and a net decrease in the number of defects. The increase in the number of defect planes in thicker films on LAO and the decrease in the number of defect planes in thicker films on STO and LSAT is consistent with the increased moment in thicker films on LAO and the decreased moment in thicker films on STO and LSAT.

On the one hand, the connection between the observation of defect planes in STEM and EELS and the trends observed in magnetism suggests that the presence of Co^{2+} ions or oxygen vacancies play an important role in the magnetism. However, we cannot rule out the possibility that the presence of defect planes is merely an indicator of greater local bond-length and bond-angle changes in the film which could also be equally important to the magnetism. For example, the lack of obvious defects in the thick ferromagnetic film on LSAT indicates that the defects are not necessarily required to stabilizing long-range ferromagnetic order, though their presence may enhance it in the 15 nm films. It is also noteworthy that in images of films on LAO and LSAT the defect planes often only appear after considerable electron beam exposure (see Chapter 3). While it is possible that the electron beam can generate oxygen vacancies in some rare cases [8, 9, 10], it is highly possible that beam irradiation induces migration of oxygen vacancies throughout the sample [11]. In such instances, it would seem that the location to which these defects migrate are most likely regions with stress induced bond-length changes in the film, thus the parallel orientation in 15 nm films on LAO and perpendicular orientation in 15 nm films on LSAT and STO.

4.2.2. Spectroscopic Characterization

Although we have found some intriguing correlations between the number of defects and the magnetism of these films, we have still not addressed how these properties may influence the magnetic behavior. In order to more precisely understand the role of oxygen vacancies and in turn the role of Co^{2+} versus HS and LS Co^{3+} in the magnetism, the distribution of these ions must be determined. Using XA spectroscopy techniques, we assess the relative number of holes in the *d*-orbitals, the spin state, the valence state, and the element-specific source of the magnetism as a function of the strain.

4.2.2.1. XA Spectroscopy

For this characterization films were grown on Nb-doped STO to prevent the insulating films from charging at low temperatures during total electron yield mode measurements. Measurement of the films on all other substrates at low temperatures resulted in significant sample charging due to their insulating nature, preventing credible analyses of the spectra. In fact, our attempts to measure the transport properties of the film using a 4-point Van der Pauw [18] method show insulating resistance versus temperature behavior above 200 K, and are too

insulating for credible measurement using our measurement set-up. In any case, film growth on Nb-doped STO, circumvented our sample charging problem and provided a sufficient electron source for the total electron yield XA spectroscopy measurements.

We compare the XA spectra of a thin and thick film to explore the electronic structure changes associated with the epitaxial strain relaxation in the film. Figure 24 shows XA spectra for 15 nm and 70 nm thick films. The intensities in the figure are the sum of spectra taken under +0.5 T and -0.5 T with circularly polarized X-rays incident at a 60˚ angle from the sample surface normal. In this geometry, the applied field and X-ray polarization E-vector are pointed (mostly) along the in-plane direction of the film. After normalizing the spectra to the peak Co L_3 edge intensity (black arrow), obvious spectral differences between the strained (15 nm) and relaxed (70 nm) thick film can be discerned (orange and green arrows). Specifically, the 15 nm film shows a higher intensity ratio of pre-edge shoulder intensity (long orange arrow) to post-edge shoulder intensity (shorter orange arrow) at the L_3 peak compared to the 75 nm thick film. A similar change is also observed in the intensity and ratio of peaks at the L_2 edge of the spectra.

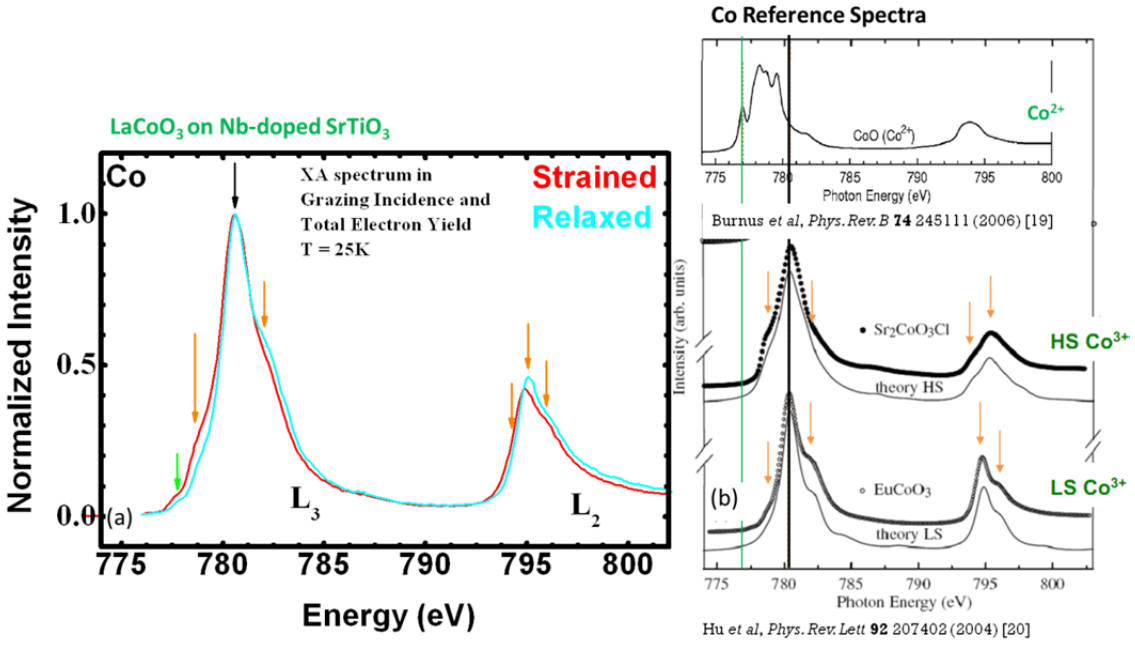

Figure 24 (a) XA spectra for films grown 15 nm (red) and 70 nm (blue) thick on Nb-doped STO. Arrows indicate relevant features described in the text. (b) A set of reference spectra for HS Co^{2+} [19], HS Co^{3+} [20], and LS Co^{3+} [20] are provided to analyze the film spectra.

In order to interpret the differences in features between the samples, we compare the sample spectra to reference spectra of Co in various valences and spin state configurations (Figure 24(b)). The reference spectrum from CoO represents HS Co^{2+} in an octahedral coordination [19], while the Sr_2CoO_3Cl and $EuCoO_3$ spectra represent pyramidal HS Co^{3+} and octahedral LS Co^{3+}, respectively [20]. The pre-edge L_3 feature at ~777 eV (green line) in the reference CoO spectrum [19] is not

reproduced in either of the reference Co^{3+} spectra from Hu *et al.* [20] which suggests that any intensity at this energy can only be associated with some presence of Co^{2+} in the sample [21]. Thus, the strained and relaxed films of LCO on STO show an indication of some amount of HS Co^{2+} present in the film as suggested by the small intensity shoulder near ~777 eV (Figure 24(a), green arrow). The intensity difference at this energy between the two films indicates that the strained film shows an increased presence of HS Co^{2+} compared to the relaxed LCO film. This result is consistent with the accommodation of strain by the presence of oxygen vacancies in the film (see Chapter 3).

We also took a closer a look at the spectra of the 15 nm and 75 nm LCO films with reference to HS and LS Co^{3+} spectra. Since these two spectra in Figure 24(b) represent 100% HS Co^{3+} (Sr_2CoO_3Cl) and 100% LS Co^{3+} ($EuCoO_3$), they serve as effective unique "fingerprints" of the different spin states in the XA spectra. Although the spectra show Co^{3+} in two different coordinations (pyramidal versus octahedral), we can still use them to get an indication of the features associated with HS and LS Co^{3+} spin configurations [20]. The reference spectra indicate that LS Co^{3+} has a higher post-edge shoulder intensity at the L_3 edge and higher pre-edge shoulder intensity at the L_2 edge. In contrast, HS Co^{3+} shows the opposite trend with relatively higher pre-edge shoulder intensity at the L_3 edge and relatively higher post-edge shoulder intensity at the L_2 edge. In the relaxed LCO film the relative ratios near the L_3 and L_2 edges are similar to the LS Co^{3+}. The strained films show an increased intensity at the pre-edge shoulder feature of the L_3 edge and a decreased intensity at the post-edge shoulder feature of the L_3 edge, thus indicating some HS Co^{3+}. The L_2 edge features of the strained films show intensity ratios that suggest some presence of HS Co^{3+}.

According to the reference spectra, the HS Co^{2+} and HS Co^{3+} have features that overlap in the pre-edge region of the L_3 peak (778 eV-779 eV). One might naively believe it is possible for the spectral features in strained films to arise from HS Co^{2+} and LS Co^{3+} contributions only. However, the decreased intensity at the post-edge shoulder feature of the L_3 edge, also associated with HS Co^{3+}, suggests that at least some of the XA intensity for the strained films must arise from contributions of HS Co^{3+}. Thus, when comparing strained and relaxed films grown on Nb-doped STO we conclude that: (i) in both films at least some amount of Co^{2+} exists (strained films may have more), (ii) in relaxed films we find mostly LS Co^{3+}; and (iii) in strained films, LS Co^{3+} and at least some amount of HS Co^{3+} exist.

4.2.2.2. XMCD

Having established the presence of Co ions in various spin states via XA spectra, we now directly correlate the presence of these Co spin states with the ferromagnetism using XMCD. This technique probes the spectral changes associated with the changes in applied magnetic field. Thus, we can qualitatively assess the role of these constituent Co ions in the long-range magnetic order. Figure 25 shows the XMCD at 25 K from an 8 nm strained film and a 75 nm relaxed film grown on Nb-doped STO measured below the magnetic ordering temperature. The largest

dichroism intensity appears near the peak labeled (b) in the corresponding XA spectrum. However, all the HS Co^{3+} and LS Co^{3+} features discussed so far in the XA spectrum can be associated with features in the magnetic dichroism. The small HS Co^{2+} feature does not show a strong contribution to the magnetic dichroism intensity. This suggests that the HS Co^{3+} and LS Co^{3+} contributions are the primary source for magnetism in the strained LCO films on STO. In the 75 nm film the dichroism intensity is lower compared to the 8 nm film, consistent with the finding that the net moment per Co ion from the 75 nm film is lower than that of the 8 nm film from SQUID magnetometry. Since the XA measurement is highly surface sensitive, the lower net moment measured from SQUID magnetometry cannot be associated with a few strained layers closest to the substrate-film interface, but must arise from (partially relaxed) layers at the surface of the film as well.

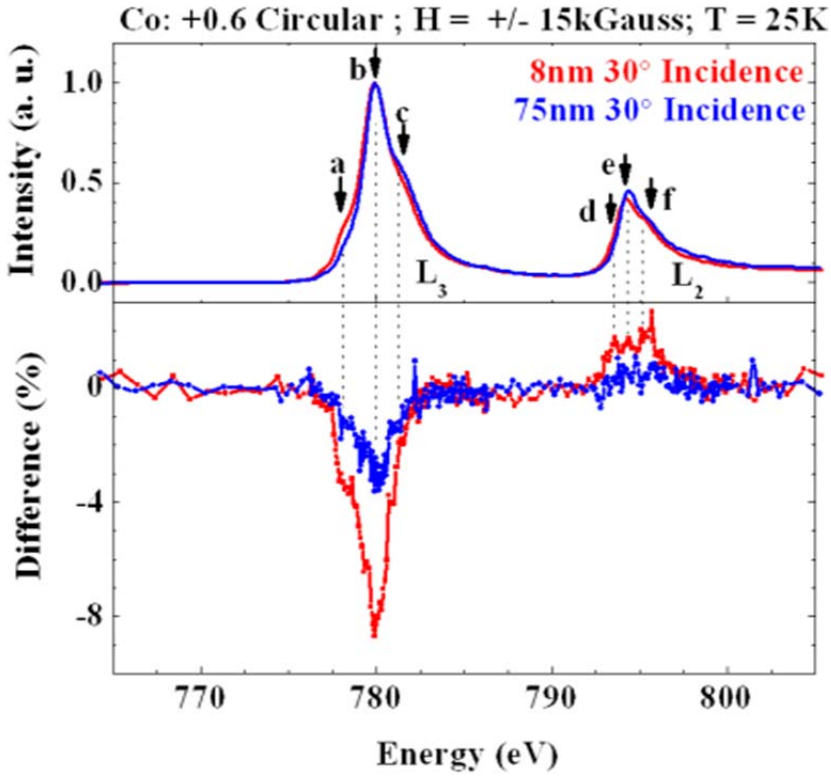

Figure 25 XA (top panel) and corresponding XMCD (bottom panel) spectra for 8 nm and 75 nm films grown on Nb-doped STO.

4.2.2.3. XNLD

Room temperature XNLD was used to compare differences in electronic occupation of the Co *d*-orbitals for strained films on STO, LSAT, and LAO, and a relaxed film on LAO. By measuring the linear dichroism at room temperature, we are able to minimize charging effects from the insulating samples, and we ensure that the observed linear dichroism is from bonding anisotropies and not magnetic

anisotropy in the film. With the sample at 30˚ grazing incidence, vertical and horizontal linearly polarized X-rays can be used to probe in-plane and (predominantly) out-of-plane hole density of the Co ion electron configuration.

Figure 26 shows the orientation-averaged XA spectra and corresponding XNLD intensity. The XA spectra (Figure 26(a)) for films grown on different substrates show subtle intensity differences at the L_3 and L_2 edges associated with HS Co^{2+}, HS Co^{3+}, and LS Co^{3+} features discussed previously. In particular, LSAT films have the highest intensity at the pre-edge shoulder associated with HS Co^{2+}, followed by STO, relaxed LAO, and, finally, strained LAO. This trend is consistent with findings of increased oxygen vacancies for LSAT films from STEM and EELS studies. The relative presence of HS Co^{3+} ions follows this same trend, with films on LSAT having the largest intensity at the pre-edge L_3 feature.

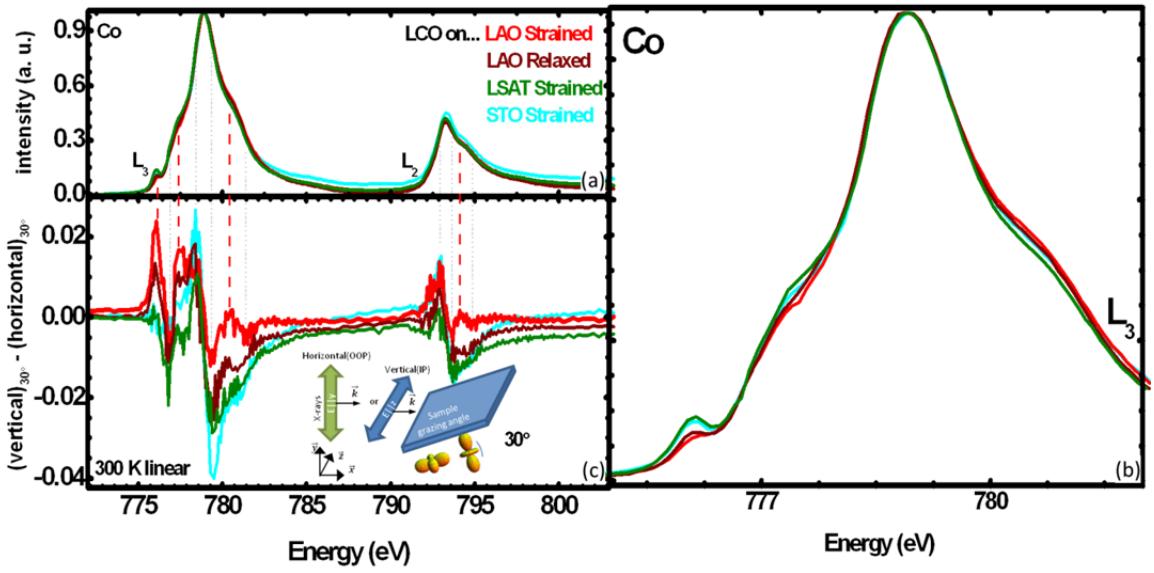

Figure 26 (a) XA and XNLD (c) spectra for films grown on LAO (red), LSAT (green), and STO (blue). The figure on the right (b) is an enlarged region of the Co - L_3 edge showing the spectral changes from growth on different substrates.

The XNLD also shows unique substrate-dependent differences. The most significant differences are indicated by the dashed red lines in Figure 26(c). We find these differences between films grown in tension on STO and LSAT and films in compression on LAO. Films relaxed on LAO show similarities in the linear dichroism to both strained films on LAO and strained films on LSAT and STO. While many of these dichroism differences may be due to different contributions from HS Co^{2+}, HS Co^{3+}, and LS Co^{3+} [21], lattice distortions may also influence the anisotropies in charge density [22]. From chapter 3 we know that films grown on LAO have c/a >1 and films grown on LSAT and STO have c/a <1. Thus, we might expect that the constituent Co ions in the film adopt an additional anisotropic charge density due to the distortions of the Co-O octahedral cage under epitaxial strain. For example, the strong linear dichroism feature near the L_2 edge in all samples can only be accounted for by a contribution from tetragonally-distorted LS Co^{3+}, since linear

dichroism from HS Co^{2+}, HS Co^{3+}, and undistorted LS Co^{3+} in this energy range is not significant [21].

Together, XA spectroscopy, XMCD, and XNLD indicate that the ferromagnetism is primarily associated with increased presence of HS Co^{2+} and HS Co^{3+} in epitaxial films. XMCD shows that more HS Co^{3+} is associated with ferromagnetic order. XNLD shows that there is a clear difference in the anisotropic hole density in the strained (and relaxed) films indicating that lattice distortions have a significant impact on the electronic structure. While more simulation work is needed to properly fit the spectra to determine quantitatively the amount of each ion in the various films, these studies suggest that a change in the relative quantity of HS Co^{2+}, HS Co^{3+}, and LS Co^{3+} results in a change in the magnitude of the moment.

4.3. Oxygen growth pressure effects on ferromagnetism

While STEM and EELS results have suggested that the density of oxygen defects are related to the magnitude of long-range magnetic order, we have also found an overall suppression of the ferromagnetism in LCO films with decreasing ambient oxygen pressure during deposition. Figure 27 shows the change in Curie temperature for films grown on STO substrates in different oxygen pressures. As growth pressure is decreased the Curie temperature decreases. Similar decreases are observed in the remanence and saturation magnetization of the films with decreasing oxygen growth pressure. This trend suggests that the presence of defects caused by growing the films in a lower background oxygen pressure results in suppression of long-range magnetic behavior. As we found in chapter 3, the lower oxygen pressures also result in an expansion of the out-of-plane lattice parameter. In Figure 27, we see the magnetism (Curie temperature and saturated moment) decreases as the structure increases in size with decreasing oxygen growth pressure.

To better gauge the electronic structure effects associated with growth in high and low growth pressures, we performed surface sensitive XMCD measurements on samples grown in 10 mTorr and 200 mTorr of O_2. Figure 28 shows the differences in XA lineshape and XMCD intensity between a sample grown in 10 mTorr and 200 mTorr on Nb-doped STO. Intriguingly, the L_3 pre-edge shoulder feature associated with Co^{2+} ions and the pre-edge feature associated with HS Co^{3+} ions in the film have increased intensity in the 10 mTorr sample, suggesting a greater presence of Co^{2+} ions and possibly HS Co^{3+} ions in the film. Recalling the reference data from Figure 24(b), we know these two ions have spectral features that overlap, so determining the relative increase of these ions in the film grown in 10 mTorr of O_2 is difficult. Surprisingly, the increase in HS Co^{2+} and HS Co^{3+} ions is not associated with an increase in magnetism from the Co ion in this film. On the contrary, the largest magnetic dichroism intensity is observed in films grown in the highest oxygen pressures, confirming trends observed in SQUID magnetometry. This suggests that either, (i) there are some inherent shortcomings in using this fingerprinting method to qualitatively interpret the relative number of Co ions in the film; or (ii) that despite the increased presence of HS Co^{2+} and (possibly) HS Co^{3+}

(i.e. ions with moment) the mechanism of long range ferromagnetic ordering is disrupted by the presence of oxygen growth related defects. For example, the increased presence of defects could cause a suppression of the exchange mechanism in certain directions or an incomplete percolation of magnetic mixed Co ion clusters throughout the film.

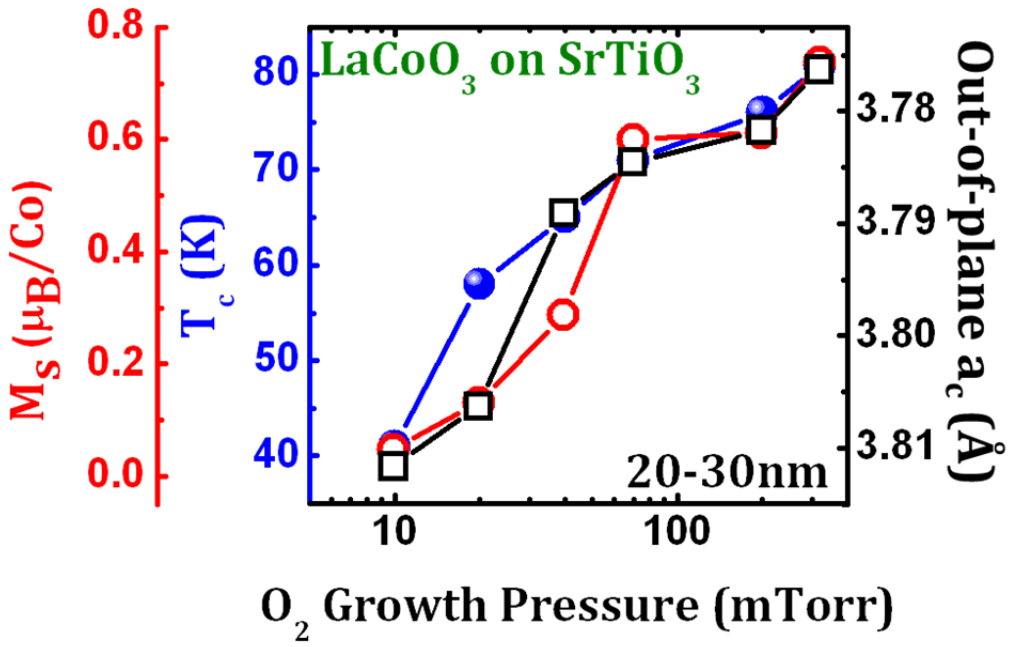

Figure 27 Curie temperature and saturated moment (left axes) as a function of oxygen growth pressure for films on STO. The out-of-plane lattice parameter decreases with increasing oxygen pressure (right axis).

The decrease in magnetism with lower oxygen pressure suggests that the overlap of Co and O orbitals involved in the indirect exchange mechanism may be disrupted in the films grown in lower oxygen pressures due to the location of vacant oxygen sites in the film. Despite the increased HS Co^{3+} and HS Co^{2+} presence in these films grown in lower oxygen pressure, the magnetic moment and Curie temperature are reduced. These findings are in apparent contradiction to the results from STEM and EELS which show that the highest moment in films grown on LSAT and STO are associated with increased oxygen vacancy planes. However it appears that it is not the mere presence of oxygen defects but the elongation of the out-of-plane lattice parameter that can be correlated with ferromagnetism. Coherent nonmagnetic films on LAO and films grown in lower oxygen pressure on any substrate have an elongated out-of-plane lattice parameter.

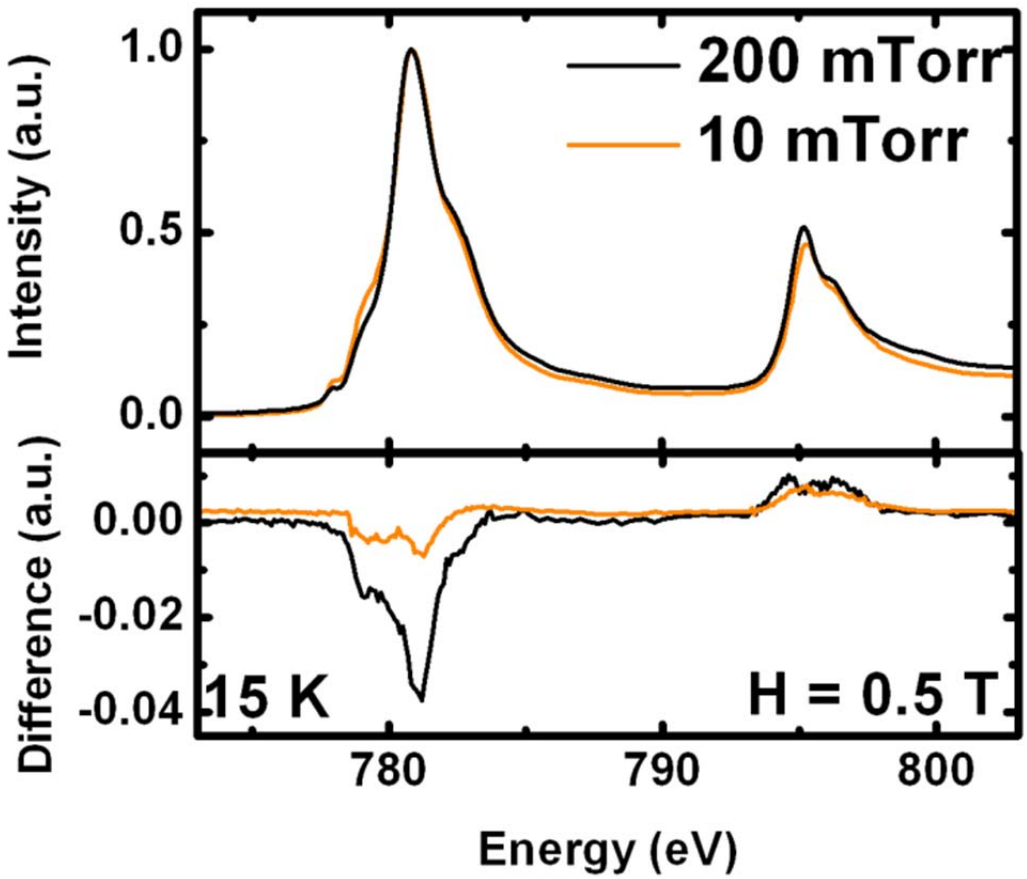

Figure 28 XA and XMCD spectra for films grown on Nb-doped STO in 10 mTorr (orange) and 200 mTorr (black) of oxygen.

4.4. Co spin states and valence states in $LaCoO_3$ films

The application of epitaxial strain appears to have many different effects on the films, all of which may play an important role in suppressing or giving rise to long-range magnetic order. At the very least, we can conclude that the epitaxial strain results in a tetragonal distortion of the lattice. The strain in the film appears to be correlated to the presence of oxygen vacancy defects and changes in the amount of HS Co^{3+} ions in the film.

Together the stoichiometric, structural, and magnetic trends of LCO films in these two chapters (3 and 4) allows us to construct a qualitative picture of the exchange mechanism that may be responsible for the ferromagnetism observed in these LCO films. There are four key trends to consider. (1) Films strained with expanded in-plane lattice parameters have a moment of ~2 μ_B/Co on LSAT and ~1 μ_B/Co on STO. Films strained with contracted in-plane lattice parameters do not show long-range magnetic order. (2) The highest moment we observe (strained LCO films on LSAT) is associated with the greatest number of oxygen vacancy planes (every 2-3 unit cell perpendicular to the film plane). Nonmagnetic films (on LAO)

are associated with the fewest oxygen vacancy ordering planes (every 3-4 unit cells oriented parallel to the film plane). (3) Inducing defects that result in an elongation of the out-of-plane direction using lower oxygen growth pressures suppresses the ferromagnetism in this system. (4) Despite the variations in saturated moment, all magnetic films are insulating and have a Curie temperature <85 K.

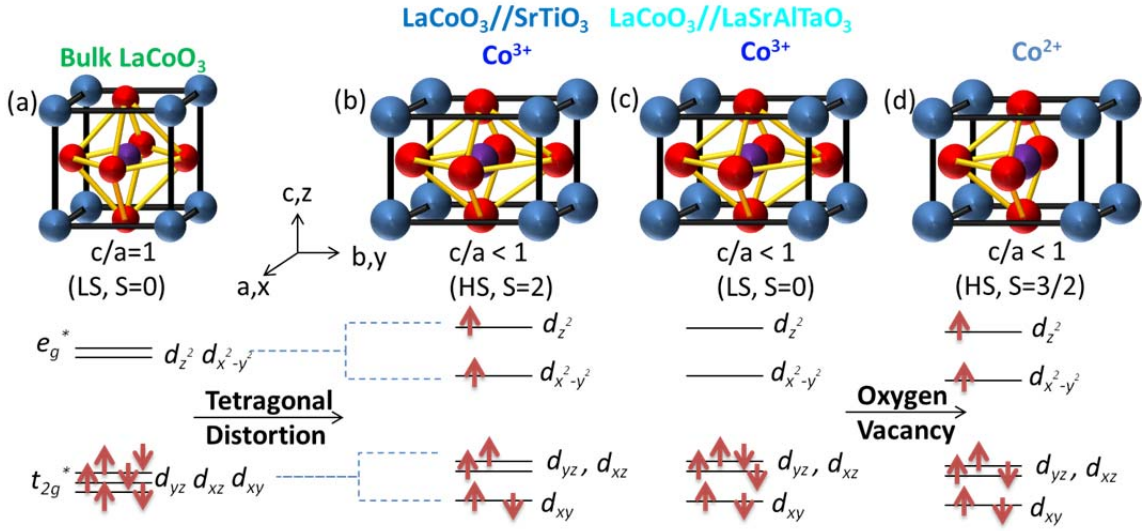

Figure 29 Schematic representation of Co unit cells and corresponding electron configurations associated with growth on STO and LSAT substrates showing (a) bulk LS Co^{3+}, (b) tetragonally-distorted HS Co^{3+}, (c) tetragonally-distorted LS Co^{3+}, and (c) tetragonally-distorted, oxygen-deficient HS Co^{2+}.

Figures 29 and 30 show a set of qualitative electron configuration models based on some likely effects of the lattice distortions and oxygen vacancies on the Co energy levels. The figures show illustrative schematic representations for: unstrained pseudocubic LCO in a LS state; HS Co^{3+} under a strain-induced tetragonal distortion; and HS Co^{2+} also in a tetragonally-distorted octahedral crystal field. This does not include all possible spin and valence state configurations possible for the Co ion under these strain conditions, but addresses the most likely scenarios suggested from the results. These scenarios are to serve as rudimentary building blocks for envisioning a ferromagnetic exchange mechanism between the mixtures of Co spin and valence states in the films. These diagrams neglect the fact that in a crystal with a mixture of ionic and covalent bonding, these energy levels would be better visualized as electron bands than discrete isolated energy levels. We have assumed a pseudocubic octahedral ligand field where the Co-O molecular orbitals are split into the three-fold degenerate nonbonding t_{2g} and two-fold degenerate antibonding e_g^* shells. For simplicity, in the HS and LS schematics, the exchange-split spin-up and spin-down levels have been drawn on a redundant energy scale for all e_g^* and t_{2g} orbitals, while in a more accurate depiction we might expect the minority-spin (spin-down) electron levels in HS states to be higher in energy than the majority-spin (spin-up) e_g^* levels.

Figure 29(a) shows the electronic configuration for undistorted bulk-like LS Co^{3+} in pseudocubic LCO which has no net spin moment (S=0) and behaves as a diamagnetic insulator at low temperatures in the bulk. Figures 29(b-d) show the schematic change in symmetry of the LCO unit cell due to presumed bond-length distortions induced by epitaxial tensile strain. As a result of the decreased z-axis length and increased x,y-axis length, the e_g^* and t_{2g} orbital degeneracy is further reduced and the octahedral O_h symmetry is reduced to D_{4h} symmetry. The antibonding and nonbonding molecular orbitals, which have mostly transition metal-like *d*-orbital character, shift in relative energy position. Due to the presumed bond length distortions from the epitaxial strain, *d*-orbitals with x,y-axis components have decreased overlap with neighboring oxygen orbitals. The decreased overlap results in a relative decrease in energy of these antibonding and nonbonding molecular orbitals. Another electron configuration possibility introduced in these investigations is the HS Co^{2+} ion, which may be present due to the observed oxygen vacancies in the film (Figure 29(d)). XNLD suggests that a distorted lattice from epitaxial growth is also likely to be found for the Co^{2+} ions. The electron configuration for Co^{2+} in a HS state is very similar to Co^{3+} in HS state with one more electron in the t_{2g} subband.

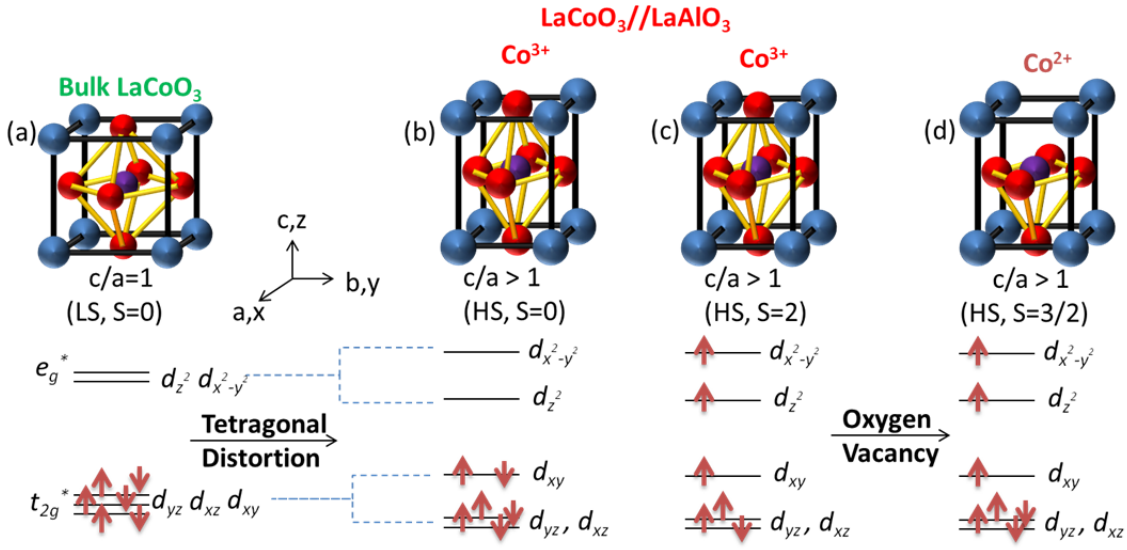

Figure 30 Schematic representation of Co unit cells and corresponding electron configurations associated with growth on LAO substrates showing (a) bulk LS Co^{3+}, (b) tetragonally-distorted LS Co^{3+}, (c) tetragonally-distorted HS Co^{3+}, and (c) tetragonally-distorted, oxygen-deficient HS Co^{2+}.

The model that explains the ferromagnetic exchange mechanism in this mixed spin/mixed valence system must also account for the absence of a ferromagnetic moment in strained films on LAO. Figure 30 shows the set of possible Co spin and valence states for tetragonally-distorted films of LCO on LAO. The key difference between these possibilities and the ones for films on LSAT and STO is the shift in energy position of the different d-orbitals due to the different lattice strain. In films on LAO the pure in-plane orbitals d_{xy} and d_{x2-y2} orbitals are higher in energy

due to the shorter in-plane bond lengths. This change would cause only a subtle difference in the e_g^* electron filling between the films on LAO and films on LSAT and STO. However, in the t_{2g} orbitals this results in a lower energy for the degenerate set of orbitals, the d_{xz} and d_{yz} orbitals, compared to films on LSAT and STO. This may play a role in the differences in magnetic behavior, since the holes in the t_{2g} shell in the film on LAO occupy the non-degenerate d_{xy} level, while in contrast the holes in films on LSAT and STO exist exclusively in the degenerate t_{2g} subband,

4.5. The ongoing exploration of the ferromagnetic exchange mechanism

The ferromagnetic exchange mechanism in the films on LSAT couples a mixture of HS Co^{3+} (S=2, ~4 μ_B/Co), LS Co^{3+} (S=0, ~0 μ_B/Co), and HS Co^{2+} (S=3/2, ~3 μ_B/Co) to result in a net moment in the film of ~2 μ_B/Co. Films on STO show ferromagnetism most likely through a similar exchange mechanism, but in the case of STO the net moment is only ~1 μ_B/Co. STEM and EELS have shown that the oxygen vacancy contents of these LSAT and STO films are different, most likely due to the changes in strain and lattice distortions between these two films. Thus, it is likely that the mixture of Co ions in these various spin and valence states is also different, accounting for the difference in the net moment. In a similar way, films grown on LAO also contain a unique distribution of Co ions as revealed by the XA spectra and STEM and EELS measurements. In strained films on LAO, the exchange is suppressed among the different Co ions and long-range magnetic ordering does not occur. It is still unclear whether the suppression of long-range order is caused by this different mixture of Co ions or through some other means such as the lattice distortions felt by these ions. However, in thicker more relaxed films on LAO, the mixture, distortion, and organization of Co ions in the film changes to allow for long-range ordering to occur.

Thus, the future for LCO film studies still holds some interesting challenges and open questions. The understanding of oxygen vacancy formation and migration in perovskite oxides is a field heavily studied by the fuel cell community [23] in the context of ion transport and oxidation-reduction reactions, but its importance in the study of thin film ferromagnetism is only beginning. Until we can accurately measure oxygen content and oxygen-related effects, the role of these defects in correlated electron systems will always be a challenge. To understand the complex interactions between the numerous Co spin states in LCO films, we must pursue theoretical work. Simulation of multiplet effects to deconvolute the Co contributions to different XA features is a problem that can be tackled easily in the future. The greater underlying challenge is to develop a picture that can account for (i) the presence of long-range ferromagnetism with a robust T_c, (ii) a variable saturated moment, and (iii) insulating behavior in LCO films. This will require considerably more work from both theoretical [24, 25, 26, 27] and experimental perspectives.

In conclusion, LCO is a fascinating system for epitaxial studies due to the delicate balance between crystal field and Hund's energy that is easily perturbed through external forces. In this work we have demonstrated some of the interesting nuances associated with the use of epitaxial strain to change the spin state of the

system at low temperatures. We have shown that the films display lattice distortions, strain-correlated oxygen vacancies, and changes in valence and spin state, and, as a result, show differences in magnetic moment and long-range ordering. The results presented here also show the difficulty in succinctly attributing the cause of ferromagnetism in thin films of LCO to a Jahn-Teller-distorted superexchange effect [3] or a mixed-valent defect effect [2, 6]. Despite the lack of a conclusive exchange mechanism to explain all of the phenomena observed in these various films, it is clear that epitaxial strain of LCO can be tuned to give rise to unique structural and magnetic properties.

Chapter 5: Extensions to Pr-based Cobaltite: inducing A-site ordering

5.1. Motivation for exploring other cobaltites

5.2. Growth and structural characterization of epitaxially strained $PrCoO_3$ films

5.3. Exploring long-range magnetic order in $PrCoO_3$ films on $SrTiO_3$

5.3.1. Magnetism and epitaxial strain

5.3.2. Element-specific magnetic order

5.4. Novel and emergent Pr-sublattice ordering

5.5. Conclusions

Abstract

In this chapter, I find that heteroepitaxial strain of $PrCoO_3$ films grown on $SrTiO_3$ and $LaSrAlTaO_3$ is found to induce long-range ordering of the Co ions. $PrCoO_3$ films grown on $SrLaAlO_4$ and $LaAlO_3$ do not show any long-range order. By specifically exploring epitaxial films of $PrCoO_3$ grown on $SrTiO_3$ 001 substrates, we show that this order is the result of a stabilization of a *ferri*magnetic ground state, in stark contrast to paramagnetic insulating behavior of observed in bulk. The ferromagnetic ordering of the CoO_6 array, which is deduced to be partially in a high spin state, is accompanied by ordering of the Pr sub-lattice in an antiparallel orientation to the Co. This ordering of the Pr sub-lattice provides evidence for significant Co-Pr exchange, apparently facilitated by the presence of high spin Co. The long-range magnetic order in epitaxial $PrCoO_3$ is thus fundamentally different from the ferromagnetism found in alkaline earth doped $PrCoO_3$, as evidenced by the very different electronic properties, tendencies to rare-earth magnetic ordering, and spin-state.

Chapter 5: Extensions to Pr-based Cobaltite: inducing A-site ordering

5.1. Motivation for exploring other cobaltites

The spin state of cobaltites can clearly be manipulated by coherent heteroepitaxial strain. Scientists have also used hydrostatic pressure [1] and chemical pressure in the form of substitution of La with a smaller rare earth cation [2] to alter the stability of the low spin state. Hydrostatic pressure increases the spin gap by decreasing the Co-O bond lengths (which increases the crystal field splitting [3, 4] and decreasing the Co-O-Co bond angle (which decreases the e_g^* bandwidth [5]. Unlike hydrostatic pressure, chemical pressure stabilizes the low spin state by doing little to significantly alter the Co-O bond length, but only causes a reduction in the Co-O-Co bond angle [2]. The net result of replacing the A-site with a smaller cation, as discussed in chapter 1, is the increase in the spin state transition temperature with decreasing cation size.

Epitaxial films of $PrCoO_3$, with Pr^{3+} in a $4f^2$ state, serve as a model system in which we can explore the competing effects of chemical pressure and also modify the magnitude of the spin gap. Bulk PCO is paramagnetic and does not exhibit long-range magnetic ordering. It has a smaller, orthorhombically-distorted perovskite structure ($a_{pseudocubic(pc)} \sim 3.789$ Å) compared to bulk LCO (rhombohedrally-distorted, $a_{pc} \sim 3.81$ Å) due to the smaller ionic size of Pr^{3+} and adopts lower Co-O-Co bond angles. The chemical pressure thus decreases Co-O-Co bond angles, leading to a narrower e_g^*-derived bandwidth and a larger "spin gap" in bulk. This pressure enhances the stability of the low spin state relative to LCO, resulting in a shift of the onset of the spin state transition from about 30 K in LCO to above 200 K in PCO [2]. Epitaxially strained films in tension may oppose this stabilization and instead promote the HS state, as the observation of ferromagnetism in LCO thin films would suggest [6, 7, 8, 9, 10, 11, 12, 13]. Studies of PCO thin films could provide a first step in the direction of understanding the influence of the spin gap on ferromagnetic ordering in epitaxial films.

This system also presents a unique opportunity to explore Pr ion ordering in cobaltites. In undoped bulk perovskites, the Pr ion and the Co ions do not show long-range magnetic order. As mentioned above, the Co ions are in low spin state and are diamagnetic. Any magnetic exchange between these Co ions with the Pr ions is too weak to order the Pr sublattice, and at best only a weak paramagnetism is observed for the Pr ion at low temperatures [14, 15]. In partially doped Pr-cobaltites, where the Pr-site is substituted with an aliovalent alkaline earth cation, such as Sr, Ca, or Ba, the Co magnetic moment is modified through a change in its valence and spin state. In these compounds, the Co ions order ferromagnetically and are in intermediate spin and intermediate valence states with an itinerant e_g^* electron mediating a double exchange interaction [16]. While the Pr ions show strong hybridization with the O ions [16], no long-range magnetic order in the Pr sublattice is observed. These films present a new scenario in which Pr ions are possibly put in proximity to HS Co^{3+} ions, and by using XMCD we can probe their alignment with respect to the Co sublattice.

5.2. Growth and structural characterization of epitaxially strained $PrCoO_3$ films

To probe the role of epitaxy on the spin state transition in PCO, we grew films on (001) LSAT (a_{pc} = 3.868 Å), LAO (rhombohedral, a_{pc} = 3.79 Å), and SLAO (tetragonal, a_{pc} = 3.75 Å) substrates 25 nm thick and on (001) STO (a_{cubic} = 3.905 Å, mismatch=) substrates 8 nm, 25 nm, and 110 nm thick, by pulsed-laser deposition (248 nm KrF excimer laser, ~1 J/cm^2). All films were grown at a laser pulse rate of 3Hz in 320 mTorr of O_2 at 650-700˚C. After cooling in 10 Torr, structural characterization was performed on a Philips Panalytical 4-circle diffractometer using a $Cu_{K\alpha}$ line source. Magnetometry was performed using a 5 T Quantum Design superconducting quantum interference device (SQUID) magnetometer. X-ray absorption (XA) and X-ray magnetic circular dichroism (XMCD) measurements were performed in total electron yield mode at the Advanced Light Source (beamlines 4.0.2 and 6.3.1). Total electron yield mode limits the probe depth of XA and XMCD to the electron escape depth (~5 nm below the surface).

Substrates impart different amounts of in-plane strain on the film depending on the degree of lattice mismatch between in-plane lattice parameter of the substrate and film. Figure 31 shows the reciprocal space maps for partially strained 25 nm thick films grown on STO (~3.1% mismatch), LSAT (~2.1% mismatch), LAO (~0% mismatch), and SLAO (~-1.0% mismatch) substrates. Films on STO and LSAT are strained in tension and show lattice parameters that deviate significantly from the bulk value of 3.79 Å. The film peak for the film grown on STO is broadened (Figure 31(a)), suggesting that with a 25 nm thickness the film is partially relaxed. On the other hand, film peaks for films grown on LSAT (Figure 31(b)) and LAO (Figure 31(c)) appear sharp suggesting that these films are nominally strained to the substrate at these thicknesses. The film on SLAO (Figure 31(d)) is mostly relaxed at this thickness taking on values similar to bulk PCO in both in-plane and out-of-plane directions.

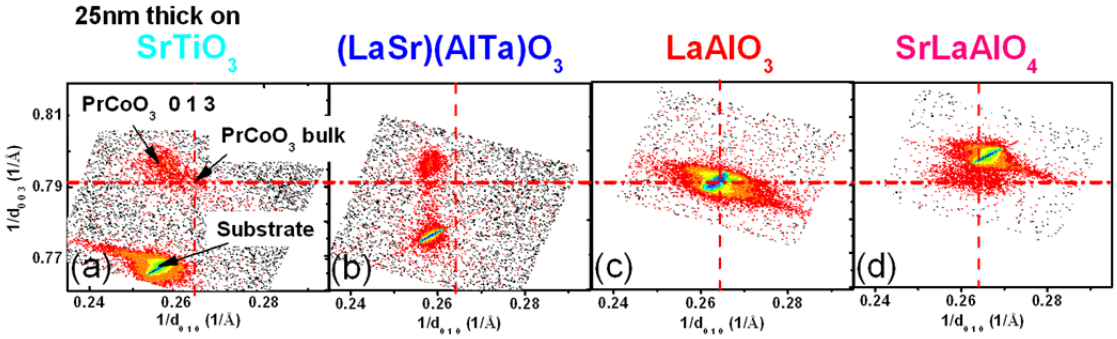

Figure 31 Reciprocal space maps around the 013 peak for 25 nm thick PCO films on (a) STO, (b) LSAT, (c) LAO, and (d) SLAO.

Only the films grown on STO and LSAT show long-range magnetic order, while films on LAO and SLAO do not show clear evidence of magnetic order. Figure 32(a) shows the moment versus applied field measurements for these 25 nm thick films, and Figure 32(b) is an enlarged region of the same measurement to show the hysteresis for films on LSAT and STO. Films on LSAT have a higher saturated moment of ~0.95 $\mu_B/PrCoO_3$ compared to ~0.17 $\mu_B/PrCoO_3$ for films on STO. The films on LSAT and STO also show a clear magnetic ordering temperature of ~53 K and 62 K, respectively (Figure 32c). Films on LAO and SLAO do not show indications of long-range magnetic order but exhibit large paramagnetic signal. In fact, these films have a larger magnetic signal than any of the other films at 5T (the signal from the film on SLAO is largest); however, it is clear that the remanent moment is zero in these two samples.

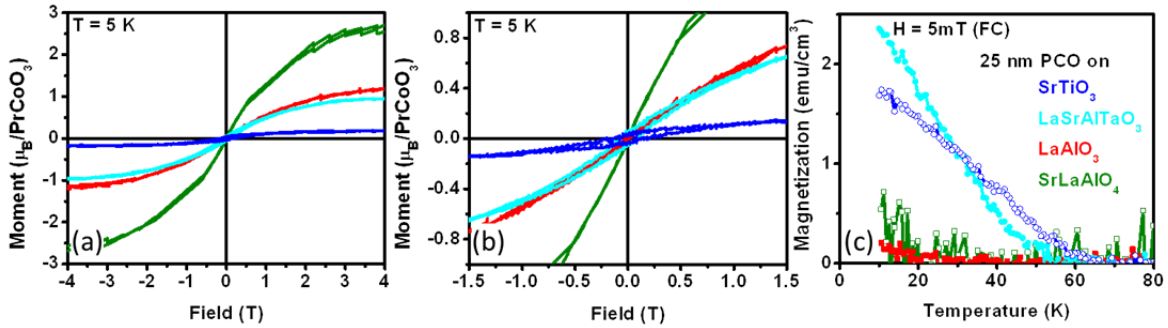

Figure 32 (a) Magnetization vs field measurements taken at 5 K for films on SLAO, LAO, LSAT, and STO. (b) Zoomed-in region of magnetization vs field measurement showing hysteresis for films on LSAT and STO. (c) Magnetization vs temperature measured in 5 mT after FC.

The larger moment and lower Curie temperature in PCO films on LSAT compared to STO is intriguing and suggests that lattice distortions affect the strength of the exchange (lower T_c) and the density of high and low spin Co ions (higher moment). In LCO films higher moment is also found in films grown on LSAT compared to films grown on STO. In both cases the lattice mismatch is larger for films on STO than on LSAT [8, 10]. In the case of LCO, we correlate the higher moment with the greater presence of HS Co^{3+}, as well as LS Co^{3+} and HS Co^{2+} ions (See Chapter 3, and 4). The 25 nm thick PCO films on STO may be slightly more relaxed than films on LSAT, due to the enormous (~3%) lattice mismatch. However, this does not fully account for the lower the net moment in films on STO, since even in a more fully strained 8 nm film on STO (discussed in detail below, Figure 34) the moment is lower than the moment for 25 nm thick films on LSAT. The lower Curie temperature for films on LSAT can be explained by a decrease in Co-O-Co bond angle in LSAT films compared to STO films. A decrease in bond angle is known to decrease the Curie temperature in mixed-valent rare-earth/alkaline-earth cobaltites [15], so it appears that despite the partial relaxation in STO films, the bond angles are still larger than films on LSAT.

Finally, the strain dependence of the magnetism in these films appears more distinct for PCO compared to LCO. PCO films strained in compression or fully

relaxed do not show long-range magnetic order, unlike LCO films which show magnetic order in relaxed films on LAO and SLAO [8, 10]. It has been suggested that relaxed LCO films are magnetic due to point defects and chemical inhomogeneities in the film [12, 13, 17]. In relaxed and unstrained PCO films, however, these defects may not exist, or may be unsuccessful in promoting long-range magnetic order.

5.3. Exploring long-range magnetic order in $PrCoO_3$ films on $SrTiO_3$

5.3.1. Magnetism and epitaxial strain

In the remaining sections, we focus specifically on PCO films grown on STO substrates to explore the evolution of the magnetic properties and the electronic structure as a function of thickness using element specific techniques. Films were grown to thicknesses of 8 nm, 25 nm, and 105 nm in 320 mTorr of O_2. PCO films 25 nm and thinner grown on STO substrates exhibit good crystallinity with a FWHM of the rocking curves (ω scans) of the 002 Bragg peaks of $\Delta\omega < 0.3°$. Thicker films show larger mosaic spread with $\Delta\omega$ up to 0.7° due to cracking during cooling, possibly from the thermal expansion mismatch between STO and PCO. All PCO films also exhibit low surface roughness with typical RMS ranging from 2.5 Å to 5 Å on a lateral length scale of 5 microns. Atomic steps from the substrate can be observed in the thinner films. Reciprocal space maps of the (013) film and substrate peaks show that the 8 nm film is coherently strained to the STO substrate (Figure 33(a)). As the PCO film thickness is increased to 25 nm (Figure 33(b)), the in-plane film lattice parameter shifts from the STO substrate values towards the bulk value of 3.79 Å, indicating film relaxation. At 105 nm thickness (Figure 31(c)) this relaxation becomes extensive.

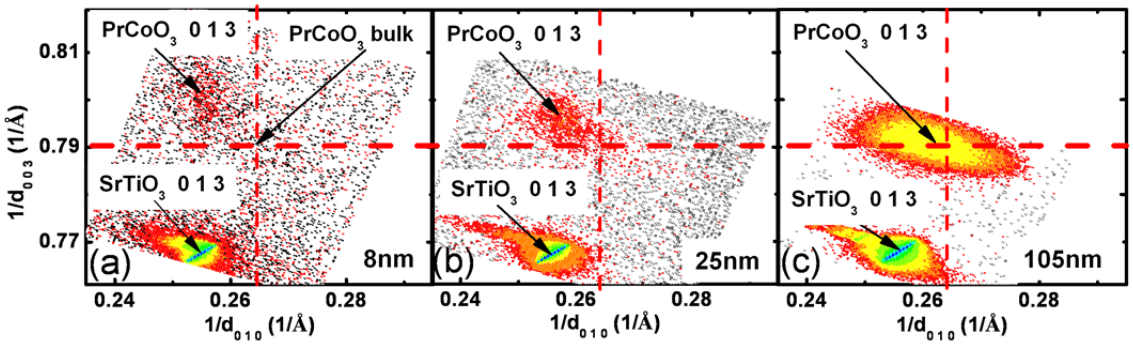

Figure 33 Reciprocal space maps of a series of $PrCoO_3$ films grown on $SrTiO_3$ substrates showing increasing relaxation of in-plane and out-of-plane lattice parameters to the pseudocubic bulk value of $PrCoO_3$ with increasing thickness for (a) 8 nm, (b) 25 nm and (c) 105 nm thick films.

All PCO films on STO exhibited magnetic order based on the temperature and field dependence of the magnetization (Figure 34). In order to obtain accurate

magnetization values, a high field negative slope background was subtracted from the data to eliminate diamagnetic and paramagnetic substrate contributions to the overall magnetic signal. The magnetization versus field loops show hysteresis, characteristic of magnetic order. Figure 34(a) shows that the saturated moments do not scale with thickness. We find the highest saturated moment (~0.4 μ_B/$PrCoO_3$ formula unit) on the thinnest films and observe a rapid drop in the moment with increasing thickness, eventually falling below 0.1 μ_B/$PrCoO_3$. Figure 34(b) shows the magnetization dependence on temperature. The plots have been normalized to their low temperature values to compare differences in Curie temperature. The 8 nm and 25 nm thick films have comparable Curie temperatures of ~60 K, while the 105 nm thick film shows a significant decrease in the Curie temperature to around 40 K. As might be expected from strain relaxation arguments, the thickest films show some evidence of broadened transition to the paramagnetic state. All films show a monotonic decrease in magnetization as a function of increasing temperature, indicative of a single magnetic ordering temperature for the moments in the film.

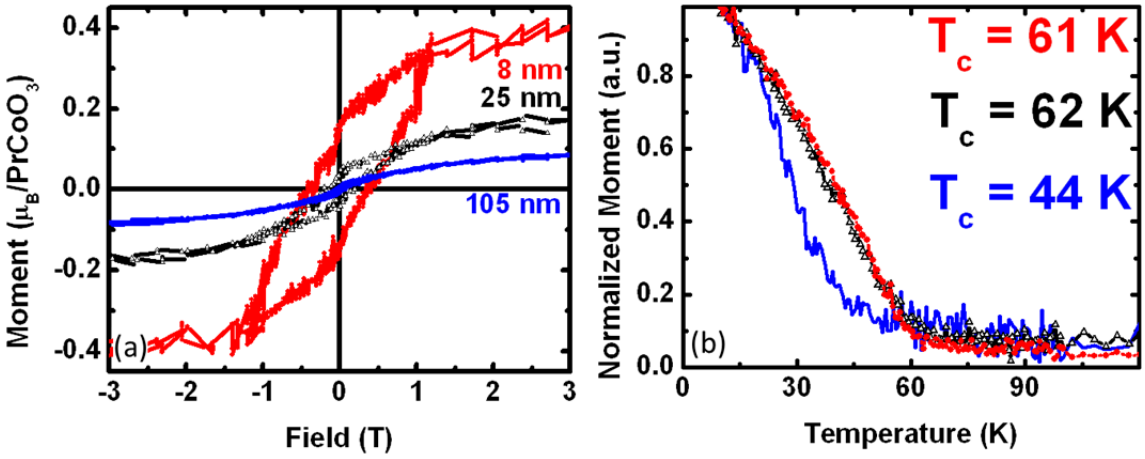

Figure 34 (a) Magnetization versus magnetic field at 5 K of PCO films with variable thickness. (b) Magnetization versus temperature after field cooling and applying a static field of 5 mT indicates the varying T_c as a function of film thickness.

5.3.2. Element-specific magnetic order

The ferromagnetism was probed by element-specific X-ray magnetic circular dichroism (XMCD) at 15 K in alternating 0.5 T field. Since transport measurements revealed PCO film samples to be insulating, similar to films on LCO [12], XMCD samples were grown 8 nm and 110 nm thick on conductive Nb-doped STO substrates to prevent charging. Films were measured at grazing incidence with the magnetic field applied in-plane and moment probed along this same direction to enable comparison with in-plane SQUID measurements. While the Co and Pr XA spectra of the 8 nm and 110 nm PCO films were fairly similar (Figure 35(a) and 5(c)), there were considerable differences in the XMCD spectra. In any case, XMCD

signals are found at *both* Co $L_{2,3}$ (*2p* to *3d*) and Pr $M_{4,5}$ (*3d* to *4f*) absorption edges, suggesting that the ferromagnetism comes from both Co *and* Pr.

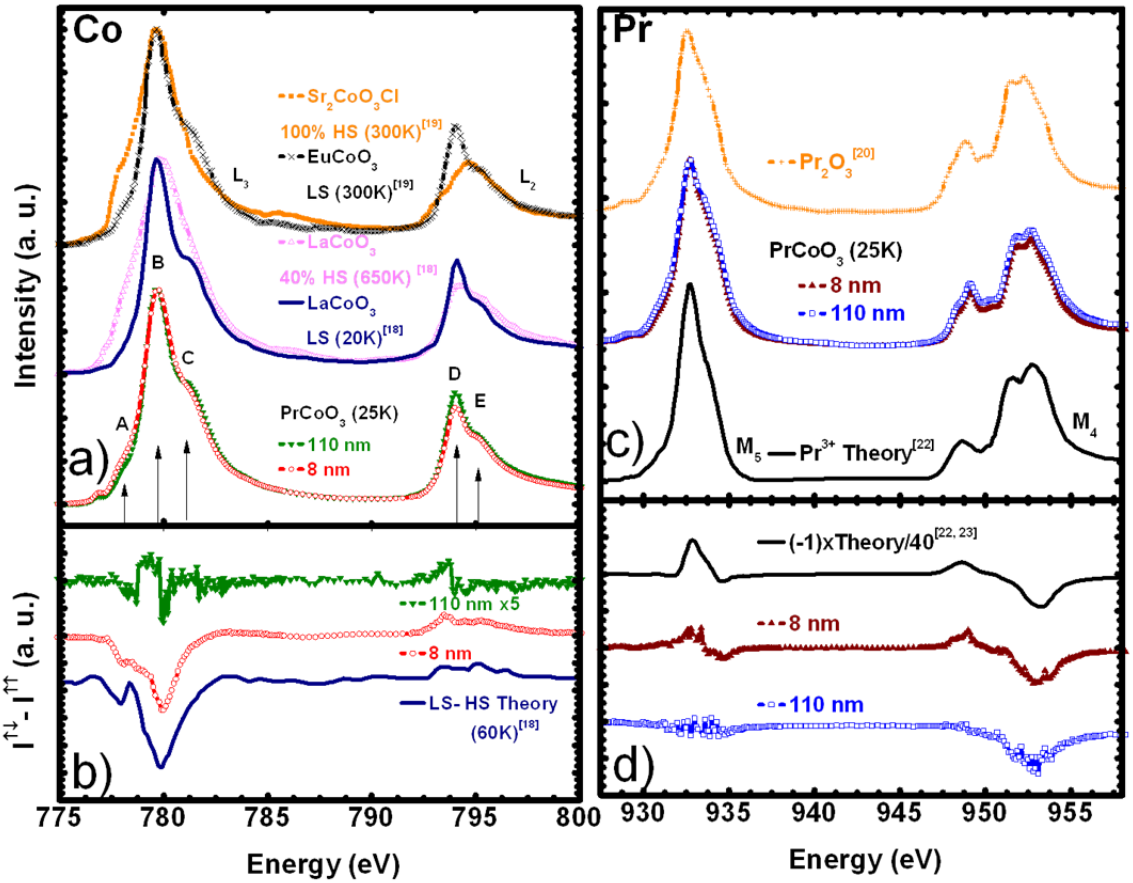

Figure 35 XA spectra (a,c) and XMCD (b,d) measured using circularly polarized X-rays and applied magnetic fields up to 0.5 T taken at the Co $L_{2,3}$ edge (a,b) and the Pr $M_{4,5}$ edge (c,d) shown alongside reference and calculated spectra from [18, 19, 20, 22, 23].

The XA line shapes in Figure 35(a) for the Co edge of the 8 nm (red open circles) and 110 nm (green solid down triangles) PCO sample indicate that there is a greater presence of HS Co^{3+} in the thinner films. For comparison, we show spectra from Haverkort *et al.* [18] for LS low temperature LCO (Figure 35(a) dark blue line) and 40% HS- 60% LS LCO at high temperatures (Figure 35(a) pink open triangles). Despite thermal phonon broadening effects of the line shape and the convolution of HS and LS features in the 650 K LCO spectrum, this spectrum suggests that (i) a slight shift (~0.2 eV) in the peak position of the L_3 edge (B) to higher energy and (ii) a change in the relative ratio of the L_3 (B) and L_2 (D) peak intensity are indicative of greater fraction of HS state Co. The 8 nm PCO film spectrum has features similar to (i) and (ii) suggesting the presence of some HS Co. Since these effects are subtle, we also compare the PCO film spectra with the Co $L_{2,3}$ spectra of Sr_2CoO_3Cl and $EuCoO_3$ (Figure 35(a) orange solid squares and black exes) which have 100% HS and 100% LS respectively [19]. Although these two compounds have different Co coordination

(i.e., pyramidal Sr_2CoO_3Cl and octahedral $EuCoO_3$), there is a clear difference in the ratio of the pre-(A) and post-(C) L_3 edge intensities with HS Co having a higher pre-edge (A) and lower post-edge (C) intensity compared to LS Co. In the 8 nm PCO sample, there is an increased intensity at region A and a decreased intensity at region C compared to the 110 nm sample, consistent with the presence of more HS Co. In addition, we see a dramatic change in the ratio of the L_2 peak (D) and L_2 post-edge (E) feature in the LS and HS Co reference samples. The LS Co has a higher D/E intensity ratio than HS Co. We observe a similar higher D/E intensity ratio in the 110 nm thick PCO film sample. These comparisons suggest that the spectral differences between 8 nm and 110 nm PCO film samples in these specific energy regions is consistent with more HS Co in the 8 nm sample compared to the 110 nm film.

The magnetic dichroism associated with the Co in PCO from the 8 nm (Figure 35(b) red open circles) film is significantly stronger than the dichroism from the 110 nm (Figure 35(b) green solid down triangles) film. The paramagnetic dichroism [18] associated with a small population of HS Co from applying 6 T on a single crystal sample of LCO at 60 K (Figure 35(b) dark blue line) shows similar features (though not identical) to the dichroism of our samples. The dichroism signal from the thick sample is significantly lower, consistent with SQUID magnetometry data, and as a result has a lower signal to noise ratio. However, since both dichroism signals from the films, using the convention $I^{\uparrow\downarrow} - I^{\uparrow\uparrow}$, match the dichroism sign changes in the paramagnetic $LaCoO_3$ reference, we can conclude that the Co moment is aligned to the applied magnetic field.

Our XMCD spectra of the Pr M edge (Figure 35(c)) are characteristic of Pr^{3+}, similar to the experimental data for Pr_2O_3 [20]. We do not observe any evidence of charge transfer or Pr^{4+} features associated with bond-length changes and strong 4*f*-2*p* hybridization, as has been observed for bulk $Pr_{0.5}Ca_{0.5}CoO_3$ in its insulating state [21]. Calculated dichroism features at the M_5 and M_4 edges [22, 23] match the features in the experimental spectrum in both relative magnitude and energy position, but not in sign, confirming the magnetism arising from the Pr^{3+} ions and their antiparallel orientation to the Co^{3+} moment and the applied field. The Pr dichroism signal is much stronger for the 8 nm film (Figure 35(d) dark red solid triangles) than for the 110 nm PCO film (Figure 35(d) blue open squares). This difference is consistent with a larger overall magnetization from the 8 nm film obtained from SQUID magnetometry.

A closer look at the magnetic field dependence of the XMCD signals at the Co and Pr edges provides insight into the switching behavior of Co and Pr. Figures 36(a) and 36(b) show element specific hysteresis loops taken at 779.9 eV for Co (region B at L_3 peak) and at 953.1 eV for Pr (M_4 peak) as a function of field. The dichroism for the 8 nm (Figure 36(a)) shows clear hysteresis indicating that both the Co and Pr are ferromagnetic. The 110 nm film (Figure 36(b)) shows no clear hysteresis and a reduced dichroism in both the Co and the Pr, thus indicating a much weaker ferromagnetism, if any, in the thicker sample.

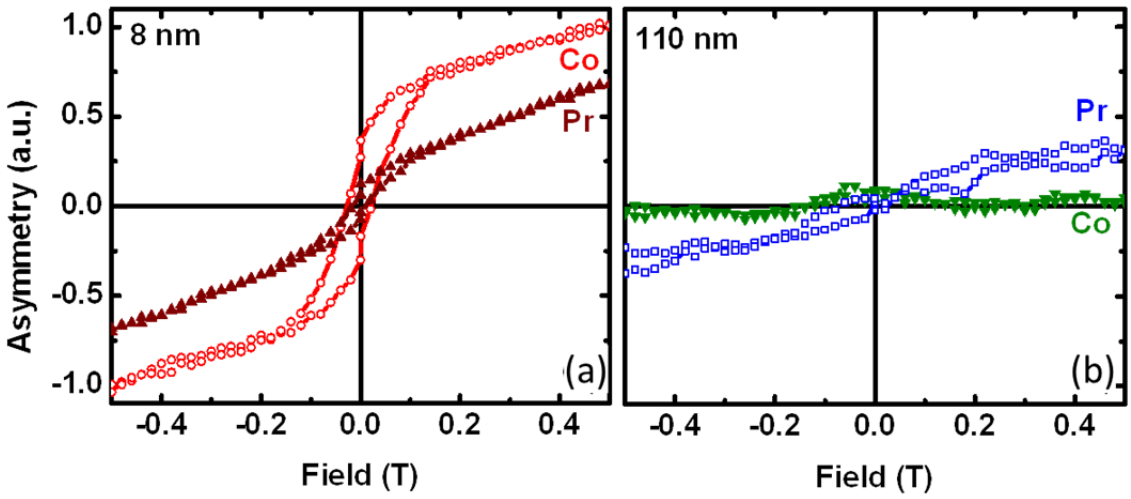

Figure 36 By holding the incident photon energy to 780 eV for Co and to 952.5 eV for Pr and sweeping the magnetic field from 0.5 T to -0.5 T, element specific hysteresis loops were taken for thin (a) and thick (b) films of $PrCoO_3$ on $SrTiO_3$ substrates.

5.4. Novel and emergent Pr-sublattice ordering

From the structural and magnetization data, it is clear that there is a strong correlation between tensile strain and ferromagnetism in the films. PCO films under coherent tensile strain have tetragonal crystal symmetry and show ferromagnetic behavior with Curie temperatures ~60 K. As the film thickness is increased and the structure becomes more cubic and akin to bulk PCO, the magnetic moment is diminished and the Curie temperature decreases. Combined with the XA evidence for high spin Co in the thinner PCO films, this trend in the magnetism suggests that we are able to stabilize long-range magnetic order and high spin cobalt via epitaxial tensile strain. We speculate that the lattice distortions arising from thin film epitaxy correspond to a change in the overall crystal field splitting and possibly even the sequence of electronic energy levels compared to the bulk. In bulk PCO, the low spin state of S=0 is stable up to 200 K, indicating that the decreased orbital overlap and hybridization due to the smaller Co-O-Co bond angles in this system, compared to LCO, aid the stabilization of the low spin state [2]. Distortion of the lattice in the tensile strained films may oppose this decrease in the Co-O-Co bond angles and asymmetrically alter the crystal field enough to drive the system to a higher spin ground state even at low temperatures. In the bulk, higher spin can be accessed through thermal activation above 200 K. Given the increased stability of the low spin Co state in bulk PCO compared to bulk LCO, it is surprising that we observe any long-range magnetic order in PCO films. Epitaxial tensile strain and chemical pressure from the smaller Pr cation represent competing influences on the spin state stability. Thus, the long-range order suggests that induced modifications of the electronic structure due to epitaxial strain dominate the tendency of decreasing bond-angle (from 164° in bulk LCO to ~157° [24] in bulk PCO) to stabilize the low spin Co state due to Pr chemical pressure on the Co octahedra. However, the

reduction in Curie temperature (T_c~60 K for PCO films compared to 80 K for LCO films [6] suggests that the smaller Pr cation does reduce the strength of the orbital overlap that gives rise to the ferromagnetic exchange between Co ions.

The most remarkable finding of this investigation is the demonstration of two ferromagnetic sublattices: One sublattice of Co ions aligning with the applied magnetic field and another Pr sublattice that is antiferromagnetically coupled to the Co moments. This result reveals that these films can be more appropriately described as *ferri*magnetic with the Co moment dominating the magnetization and inducing an opposing moment from the Pr ions. Moreover, the magnetization versus temperature suggests that the Pr sublattice has an ordering temperature at or near the same temperature as the Co sublattice (T_c~60 K). Pr^{3+} ions in bulk PCO do not show any ordering (spontaneous or induced) due to the absence of ferromagnetic exchange among the Co ions and the distance between neighboring Pr sites. In doped $Pr_{1-x}Sr_xCoO_3$, long-range ferromagnetism is observed for x >0.2 [16] and can be attributed to the double exchange interaction among intermediate spin (IS) Co moments in an intermediate valence, mediated by a mobile e_g^* electron. Features in the magnetism have been associated with an abrupt change in the magnetic anisotropy and a dramatic structural change [16, 25, 26), associated with strong Pr $4f$ –O $2p$ orbital hybridization below 120 K [16, 27]. However, most importantly in the context of this study, Pr ordering does not occur in these bulk systems [16]. In Pr^{3+} systems, despite the tendency for a singlet state, Pr site ordering can still occur provided the exchange in the vicinity of the ions is strong enough [28]. In antiferromagnetic [29], $PrMnO_3$ [30] and possibly $PrFeO_3$ [31], Pr^{3+} ions have shown to be weakly exchange coupled to the transition metal ions. In these systems, this weak exchange is often manifested as a lower moment than expected below the T_N for the transition metal sublattice.

In epitaxially strained films, the Pr moment appears to be coupled to the HS/LS Co moments. Unlike the $Pr_{1-x}Sr_xCoO_3$ IS Co scenario, the long-range magnetic order in PCO films is correlated with a greater presence of HS Co ions and electrons in t_{2g} orbitals (directed at Pr sites). Thus, the stabilization of ferrimagnetism and insulating behavior in PCO films presents unique behavior not observed in other Pr-based perovskite oxides. Since the films are insulating, the long-range Pr-ion magnetic ordering cannot be due to double exchange interaction mediated by intermediate spin and valence states, but perhaps can be due to exchange among Pr and high spin Co. Presumably, the larger ionic size and the higher spin moment of HS Co ions contribute to the Pr site ordering by increasing the possibility for strong Pr-Co exchange [28]. However, we do not observe any evidence for increased Pr-O hybridization from the XA spectra, unlike in the $Pr_{1-x}Ca_xCoO_3$ [21] and $Pr_{1-x}Sr_xCoO_3$ systems [16]. In any case, the ordering of Pr observed here is fundamentally different from the high T_c IS Co system (alkaline-earth doped $PrCoO_3$) where no Pr ordering is observed. Moreover, the ordering of the HS Co ions occurs in conjunction with the Pr ordering, as there is evidence for only one magnetic transition in the temperature dependence of the magnetization.

Since the Pr moment opposes the Co moment, we can assume that the two $4f$ spins of Pr^{3+} oppose the Co spins. So while in LCO the SQUID moment reflects the Co

moment only [9], in PCO the SQUID moment reflects the Co spin moment, minus the Pr spin moment, plus effects from orbital moments or canting. To explore this latter concept in greater detail, we used the XA spectra from HS Sr_2CoO_3Cl and LS $EuCoO_3^{Hu}$ to fit the XA from thin and thick films of PCO. We fit the relative ratios of shoulders and peaks in the L_3 and L_2 Co edges to correspond to a mixture of HS and LS Co to estimate the amount of HS cobalt at the surface of the films. This gives ~33% +/-10% HS Co in the 8 nm thick sample and ~100% LS Co in the 110 nm thick sample. This increase in LS Co contribution and decrease in magnetization for the thicker more relaxed sample is expected since bulk PCO is mostly LS Co (measured at or below 25 K). If we assume 33% HS Co in the thin film, spin only moment for the Co sublattice should be ~1.33 μ_B/Co. If we assume the Pr moment opposes the Co moment, we expect the overall moment to be significantly lower than this theoretical value. The observation of 0.4 $\mu_B/PrCoO_3$ for films on $SrTiO_3$ from SQUID magnetometry is consistent with this analysis. Here we have not included possible effects from orbital contributions (from both Co and Pr lattices) and effects from the canting of the sublattices.

5.5. Conclusions

In summary, we have stabilized a ferrimagnetic ground state in PCO films that are under coherent tensile strain. Films on LSAT and STO both show long-range magnetic order while unstrained films and relaxed films under compressive strain do not. Ferrimagnetic thin films on STO are composed of antiparallel Co and Pr ferromagnetic sublattices that simultaneously order at Curie temperatures of ≤60 K. The lower Tc, compared to ferromagnetic films of LCO [6], can be attributed to the relative changes in octahedral site rotations and resulting changes in orbital overlap mediating exchange among Co ions in PCO films. The ferrimagnetic insulating behavior observed in this study suggests that the long-range magnetic ordering is fundamentally different from the double exchange interaction found in doped cobaltites and can be attributed to strong exchange among HS Co ions and Pr ions. In the epitaxial PCO films, lattice strain overwhelms the competing chemical pressure effects from the smaller Pr cation to stabilize a low temperature HS ground state in the Co ion. It appears that capitalizing on the HS/LS Co-based magnetism in cobaltite films may offer a new route to higher temperature magnetic ordering of rare-earth ions.

Dissertation Summary and Outlook

In this dissertation, I have demonstrated the use of epitaxial strain to manipulate long-range magnetic order in cobaltites. In both $LaCoO_3$ and $PrCoO_3$ I have shown that epitaxial strain in tension plays an important role in (at least partially) altering the spin state of the Co ions and results in a ferromagnetic exchange mechanism that may involve HS Co^{2+}, HS Co^{3+}, and LS Co^{3+}. The films are characterized with a Curie temperature consistently below ~85 K and with a saturated moment varying from 0 to ~2 μ_B/Co. This moment appears to depend on tetragonal distortion in the film, though stoichiometry likely plays a role as well. Indeed, in $LaCoO_3$ films there is a clear indication (from the thick film growth on LAO substrates) that defects may play an important role in stabilizing long-range magnetic order. The analysis of the microstructure shows that ordering of oxygen vacancies in the films seem to be related to the sign (tension or compression) and magnitude of the epitaxial strain. It is still unclear precisely what role the oxygen vacancies observed in this study play in the magnetism of the films, but evidence of their influence is certain from the study of the electronic structure. The existence of ordered oxygen vacancies in these films and their dependence on the strain state is interesting and warrants further studies, but unfortunately access to these microscopy instruments is always in high demand and getting enough time and reliable statistics (many samples) is a slow process.

In $PrCoO_3$ films I found that the strain dependence is more obvious, and the role of defects is more nebulous. Regardless the largest moments are found in strained films in tension while relaxed films show a significantly decreased moment, and unstrained films (on LAO) and films strained in compression do not show long-range magnetic order at all. The findings suggests that the presence of an ordered HS/LS Co^{3+} sublattice induces a novel ordering of the Pr sublattice. To my knowledge, this is the first demonstration of Pr sublattice ordering in the cobaltites and an example of Pr ordering to relatively high temperatures (~60 K).

The research presented in this dissertation motivates more work in many new directions pertaining to the control of spin states in cobaltites and the precise understanding of the ferromagnetic exchange mechanism in these thin film systems. Although I have uncovered some of the necessary elements (Co ions in various spin and valence states) that are involved in the ferromagnetism of cobaltite thin films, more research is under way by numerous groups to fully explain ferromagnetic exchange mechanism. Also, the demonstration of ferrimagnetism in $PrCoO_3$ films opens up new avenues of exploration into other rare-earth cobaltites, which may show stronger or weaker ferrimagnetic ordering (compared to $PrCoO_3$ thin films) with the use of a different rare-earth element. It would be interesting to see whether these observations are uniquely related to some property of the Pr ions (Pr is well-known to hybridize strongly with O ions in these compounds), or if ordering can be found on a sublattice of any of the other later elements in the series (Nd – Tm).

References

Chapter 1 References

[1] M. Ellis, N. Jollands, L. Harrington, and A. Meier, Do energy efficient appliances cost more. In Proceedings of the ECEEE 2007 Conference (2007).

[2] Gregg, J. F., I. Petej, E. Jouguelet, and C. Dennis. Spin electronics—a review, Journal of Physics D: Applied Physics **35**, R121 2002).

[3] M. Bibes and A. Barthelemy, Oxide spintronics, IEEE Transactions on Electron Devices **54**, 1003 (2007).

[4] J. Stohr and H. C. Siegmann, H.C. *Magnetism - from fundamentals to nanoscale dynamics*, (Springer-Verlag, Berlin, 2006), 1st ed.

[5] D. Feng and G. Jin, *Introduction to condensed matter physics*, (World Scientific, 2005).

[6] J. B. Goodenough and J. –S. Zhou, Chapter 1: General considerations, in *Localized to itinerant transitions in perovskite oxides*, Structure and Bonding **98**, (Springer-Verlag, New Jersey, 2001)

[7] Goodenough, J.B. Electronic and ionic transport properties and other physical aspects of perovskites. Reports on Progress in Physics, **67**, 1915 (2004).

[8] R. L. DeKock and H. B. Gray, *Chemical structure and bonding*, (University Science Books, Sausalito, 1989). 2nd ed.

[9] F. A. Cotton, *Chemical applications of group theory*, (Wiley, 1990). 3rd ed.

[10] J. K. Burdett, *Chemical bonding in solids*, (Oxford University Press, 1995).

[11] J. K. Burdett, *Molecular orbital theory*, AccessScience, (McGraw-Hill, 2010.). <http://www.accessscience.com>, 2012.

[12] J. B. Goodenough, *Magnetism and the chemical bond*, Interscience Monographs on Chemistry **1**, F. A. Cotton, ed (Wiley, New York, 1963).

[13] J. M. Rondinelli and N. A. Spaldin, Structure and properties of functional oxide thin films: insights from electronic-structure calculations, Advanced Materials **23**, 3363 (2011).

[14] P. W. Anderson, Antiferromagnetism. theory of superexchange interaction. Physical Review **79**, 350 (1950).

[15] C. Zener, Interaction between the d-shells in the transiton metals. II. Ferromagnetic compounds of manganese with perovskite structure, Phys. Rev. **82** 403 (1951).

[16] A. Ohtomo, H. Y. Hwang, A high-mobility electron gas at the $LaAlO_3/SrTiO_3$ heterointerface, Nature **427**, 423 (2004).

[17] J. Mannhart and D. G. Schlom, Oxide interfaces--an opportunity for electronics, Science **327,** 1607 (2010).

[18] F. J. Wong, S.-H. Baek, R. V. Chopdekar, V. V. Mehta, H.-W. Jang, C.-B. Eom, and Y. Suzuki, "Metallicity in $LaTiO_3$ thin films induced by lattice deformation," Physical Review B **81**, 161101 2010.

[19] M. Imada, A. Fujimori, Y. Tokura, Metal-insulator transitions. Reviews of Modern Physics, 70, 1039 (1998).

[20] R. R. Heikes, R. C. Miller, and R. Mazelsky, Magnetic and electrical anamolies in $LaCoO_3$, Physica **30**, 1600 (1964).

[21] P. M. Raccah and J. B. Goodenough, First-order localized electron to collective electron transition in $LaCoO_3$, Physical Review **155**, 932 (1967).

[22] M. A. Korotin, S. Y. Ezhov, I. V. Solovyev, V. I. Anisimov, D. I. Khomskii, and G. A. Sawatzky, Intermediate-spin state and properties of $LaCoO_3$, Physical Review B **54**, 5309 (1996).

[23] M. Haverkort, Z. Hu, J. Cezar, T. Burnus, H. Hartmann, M. Reuther, C. Zobel, T. Lorenz, A. Tanaka, N. Brookes, H. Hsieh, H.-J. Lin, C. Chen, and L. Tjeng, Spin State Transition in $LaCoO_3$ Studied Using Soft X-ray Absorption Spectroscopy and Magnetic Circular Dichroism, Physical Review Letters **97**, 176405 (2006).

[24] T. Vogt, J. Hriljac, N. Hyatt, and P. Woodward, Pressure-induced intermediate-to-low spin state transition in $LaCoO_3$, Physical Review B **67**, 140401 (2003).

[25] G. Vankó, J.-P. Rueff, A. Mattila, Z. Németh, and A. Shukla, Temperature- and pressure-induced spin-state transitions in $LaCoO_3$, Phyical Review B **73**, 024424 (2006).

[26] D. Kozlenko, N. Golosova, Z. Jirák, L. Dubrovinsky, B. Savenko, M. Tucker, Y. Le Godec, and V. Glazkov, Temperature- and pressure-driven spin-state transitions in $LaCoO_3$, Physical Review B **75**, 064422 (2007).

[27] M. Tachibana, T. Yoshida, H. Kawaji, T. Atake, and E. Takayama-Muromachi, Evolution of electronic states in $RCoO_3$ (R=rare earth): Heat capacity measurements, Phyical Review B **77**, 094402 (2008).

[28] K. Knížek, J. Hejtmánek, Z. Jirák, P. Tomeš, P. Henry, and G. André, Neutron diffraction and heat capacity studies of $PrCoO_3$ and $NdCoO_3$, Physical Review B **79**, 134103 **(**2009).

[29] C. Leighton, D. Stauffer, Q. Huang, Y. Ren, S. El-Khatib, M. Torija, J. Wu, J. Lynn, L. Wang, N. Frey, H. Srikanth, J. Davies, K. Liu, and J. Mitchell, Coupled structural/magnetocrystalline anisotropy transitions in the doped perovskite cobaltite $Pr_{1-x}Sr_xCoO_3$, Physical Review B **79,** 214420 (2009).

[30] J. Wu and C. Leighton, Glassy ferromagnetism and magnetic phase separation in $La_{1-x}Sr_xCoO_3$, Physical Review B **67**, 174408 (2003).

[31] D. Fuchs, C. Pinta, T. Schwarz,1, P. Schweiss, P. Nagel, S. Schuppler, R. Schneider, M. Merz, G. Roth, and H. v. Löhneysen, Ferromagnetic order in epitaxially strained $LaCoO_3$ thin films, Physical Reivew B **75**, 144402 (2007).

[32] V. V. Mehta, M. Liberati, F. J. Wong, R. V. Chopdekar, E. Arenholz, and Y. Suzuki, Ferromagnetism in tetragonally distorted $LaCoO_3$ thin films," Journal of Applied Physics **105**, 07E503 (2009).

[33] A. D. Rata, A. Herklotz, L. Schultz, and K. Dörr, Lattice structure and magnetization of $LaCoO_3$ thin films, European Physical Journal B **76**, 215 (2010).

[34] A. Herklotz, A. Rata, L. Schultz, and K. Dörr, Reversible strain effect on the magnetization of $LaCoO_3$ films, Physical Review B **79**, 092409 (2009).

[35] S. Park, P. Ryan, E. Karapetrova, J. W. Kim, J. X. Ma, J. Shi, J. W. Freeland, and W. Wu, Microscopic evidence of a strain-enhanced ferromagnetic state in $LaCoO_3$ thin films, Applied Physics Letters **95,** 072508 (2009).

[36] J. W. Freeland, J. X. Ma, and J. Shi, Ferromagnetic spin-correlations in strained $LaCoO_3$ thin films, Applied Physics Letters **93**, 212501 (2008).

[37] D. Fuchs, E. Arac, C. Pinta, S. Schuppler, R. Schneider, and H. v. Löhneysen, Tuning the magnetic properties of $LaCoO_3$ thin films by epitaxial strain, Physical Review B **77**, 014434 (2008).

[38] V. Mehta and Y. Suzuki, Ferromangnetism enhanced by structural relaxation of biaxially compressed $LaCoO_3$ films, Journal of Applied Physics **109**, 07D717 (2011).

[39] R. F. Klie, T. Yuan, M. Tanase, G. Yang, and Q. Ramasse, Direct measurement of ferromagnetic ordering in biaxially strained $LaCoO_3$ thin films, Applied Physics Letters **96**, 082510 (2010).

Chapter 2 References

[1] Milton Ohring, *Materials science of thin films*, 2nd ed. (Academic Press, 2002).

[2] Chrisey, Douglas *Pulsed Laser Deposition of thin films*, 1st ed. (Wiley, 1994).

[3] R. Delmdahl and R. Paetzel, Recent developments in UV laser micromachining, in: Proceedings of SPIE, the International Society for Optical Engineering, 68740K–1 (2008).

[4] A. Mele, A. G. Guidoni, R. Kelly, A. Miotello, S. Orlando, R. Teghil, and C. Flamini, Angular distribution and expansion of laser ablation plumes measured by fast intensified charge coupled device photographs, Nuclear Instruments and Methods in Physics Research Section B: Beam Interactions with Materials and Atoms **116,** 257 (1996).

[5] B. D. Cullity and S. R. Stock, *Elements of X-ray diffraction*, 3rd ed. (Prentice-Hall, 2001).

[6] Paul Fewster, X-ray analysis of thin films and multilayers, Reports on Progress in Physics **59**, 1339 (1996).

[7] W. K. Chu, J. W. Mayer, M. A. Nicolet, T. M. Buck, G. Amsel, and F. Eisen, Principles and applications of ion beam techniques for the analysis of solids and thin films, Thin Solid Films **17**, 1 (1973).

[8] E. Rauhala, N. P. Barradas, S. Fazinic, M. Mayer, E. Szilágyi, and M. Thompson, Status of ion beam data analysis and simulation software, Nuclear Instruments and Methods in Physics Research Section B: Beam Interactions with Materials and Atoms **244**, 436 (2006).

[9] M. A. Garcia, E. F. Pinel, J. de la Venta, A. Quesada, V. Bouzas, J. F. Fernandez, J. J. Romero, M. S. Martin Gonzalez, and J. L. Costa-Kraemer, Sources of experimental errors in the observation of nanoscale magnetism, Journal of Applied Physics **105**, 013925 (2009).

[10] M. Sawicki, W. Stefanowicz, and A. Ney, Sensitive SQUID magnetometry for studying nanomagnetism, Semiconductor Science and Technology **26**, 064006 (2011).

[11] A. Ney, T, Kammermeier, V. Ney, K. Ollefs, and S. Ye, Limitations of measuring small magnetic signals of samples deposited on a diamagnetic substrate, Journal of Magnetism and Magnetic Materials **320**, 3341 (2008).

[12] R. Salzer, D. Spemann, P. Esquinazi, R. Hoehne, A. Setzer, K. Schindler, H. Schmidt, and T. Butz, Possible pitfalls in search of magnetic order in thin films deposited on single crystalline sapphire substrates, Journal of Magnetism and Magnetic Materials **317**, 53(2007).

[13] J. Stohr and H. C. Siegmann, *Magnetism-from fundamentals to nanoscale dynamics*, (Springer-Verlag, Berlin, 2006).

[14] R. Nakajima, J. Stoehr, and Y. Idzerda, Electron Yield saturation effects in L edge X-ray magnetic circular dichroism spectra of Fe, Co, and Ni, Physical Review B **59**, 6421 (1999).

[15] D. B. Williams and C. B. Carter, *Transmission Electron Microscopy III Imaging*, 1st ed. (Plenum Press, New York, 1996).

[16] Nellist, P. D. and S. J. Pennycook. The principles and interpretation of Annular Dark Field Z-contrast imaging. Advances in Imaging and Electron Physics 113. 147-203. 2000

[17] D. B. Williams and C. B. Carter, *Transmission Electron Microscopy I Basics*, 1st ed. (Plenum Press, New York, 1996).

Chapter 3 references

[1] D. Fuchs, E. Arac, C. Pinta, S. Schuppler, R. Schneider, and H. v. Loehneysen, Tuning the magnetic properties of $LaCoO_3$ thin films by epitaxial strain. Physical Review B **77**, 014434 (2008).

[2] M. A. Torija, M. Sharma, M. R. Fitzsimmons, M. Varela, and C. Leighton, "Epitaxial $La_{0.5}Sr_{0.5}CoO_3$ thin films: Structure, magnetism, and transport," *Journal of Applied Physics*, vol. 104, no. 2, p. 023901, 2008.

[3] S. Stemmer, A. J. Jacobson, X. Chen, and A. Ignatiev, "Oxygen vacancy ordering in epitaxial $La_{0.5}Sr_{0.5}CoO_{3-\partial}$ thin films on (001) $LaAlO_3$," *Journal of Applied Physics*, vol. 90, no. 7, p. 3319, 2001.

[4] D. O. Klenov, W. Donner, B. Foran, and S. Stemmer, "Impact of stress on oxygen vacancy ordering in epitaxial $La_{0.5}Sr_{0.5}CoO_{3-\partial}$ thin films," *Applied Physics Letters*, vol. 82, no. 20, p. 3427, 2003.

[5] R. Cacuiffo, D. Rinaldi, G. Barucca, J. Mira, J. Rivas, M. A. Senaris-Rodriguez, P. G. Radaelli, D. Fiorani, J. B. Goodenough, Structural details and magnetic order of $La_{1-x}Sr_xCoO_3$ ($x \leq 3$), Physical Review B **59**, 1068 (1999).

[6] P. E. Vullum, R. Holmestad, H. L. Lein, J. Mastin, M.-A. Einarsrud, and T. Grande, Monoclinic Ferroelastic Domains in $LaCoO_3$-Based Perovskites, Advanced Materials **19**, 4399 (2007).

[7]P. E. Vullum, H. L. Lein, M.-A. Einarsrud, T. Grande, and R. Holmestad, TEM observations of rhombohedral and monoclinic domains in $LaCoO_3$-based ceramics, Philosophical Magazine **88**, 1187 (2008).

[8] J. Buban, H. Iddir, and S. Öğüt, Structural and electronic properties of oxygen vacancies in cubic and antiferrodistortive phases of $SrTiO_3$, Physical Review B **69**, 180102 (2004).

[9] C. Wang, B. L. Cheng, S. Y. Wang, H. B. Lu, Y. L. Zhou, Z. H. Chen, and G. Z. Yang, Effects of oxygen pressure on lattice parameter, orientation, surface morphology and deposition rate of $(Ba_{0.02}Sr_{0.98}TiO_3$ thin films grown on MgO substrate by pulsed laser deposition, Thin solid films **485**, 82 (2005).

Chapter 4 References

[1] V. Mehta and Y. Suzuki, Ferromagnetism enhanced by structural relaxation of biaxially compressed $LaCoO_3$ films, Journal of Applied Physics **109**, 07D717 (2011).

[2] S. Park, P. Ryan, E. Karapetrova, J. W. Kim, J. X. Ma, J. Shi, J. W. Freeland, and W. Wu, Microscopic evidence of a strain-enhanced ferromagnetic state in $LaCoO_3$ thin films, Applied Physics Letters **95**, 072508 (2009).

[3] D. Fuchs, E. Arac, C. Pinta, S. Schuppler, R. Schneider, and H. v. Loehneysen, Tuning the magnetic properties of $LaCoO_3$ thin films by epitaxial strain, Physical Review B **77**, 014434 (2008).

[4] A. D. Rata, A. Herklotz. L. Schultz. And K. Doerr, Lattice structure and magnetization of $LaCoO_3$ thin films, The European Physical Journal B **76**, 215 (2010).

[5] A. Herklotz, A. D. Rata, L. Schultz, and K. Doerr, Reversible strain effect on the magnetization of $LaCoO_3$ films, Physical Review B **79**, 092409 (2009).

[6] J. W. Freeland, J. X. Ma, and J. Shi, Ferromagnetic spin-correlations in strained $LaCoO_3$ thin films, Applied Physics Letters **93**, 212501 (2008).

[7] R. F. Klie, T. Yuan, M. Tanase, G. Yang, and Q. Ramasse, Direct measurement of ferromagnetic ordering in biaxially strained $LaCoO_3$ films, Applied Physics Letters **96**, 082510 (2010).

[8] M. R. McCartney and D. J. Smith, Epitaxial relationships in electron-stimulated desorption processes at transition metal oxide surfaces, Surface science **221**, 214 (1989).

[9] S. D., Electron beam induced changes in transition metal oxides, Analytical and Bioanalytical Chemistry **374**, 732 (2002).

[10] M. R. McCartney, P. A. Crozier, J. K. Weiss, and D. J. Smith, Electron-beam-induced reactions at transition-metal oxide surfaces, Vacuum **42**, 301 (1991).

[11] D. B. Williams and C. B. Carter, *Transmission Electron Microscopy I Basics*, 1st ed. (Plenum Press, New York, 1996).

[18] L. J. van Der Pauw, A method of measuring the resistivity and hall coefficient on lamellae of arbitrary shape, Philips Technical Review **26**, 220 (1958).

[19] T. Burnus, Z. Hu, M. Haverkort, J. Cezar, D. Flahaut, V. Hardy, A. Maignan, N. Brookes, A. Tanaka, H. Hsieh, H.-J. Lin, C. Chen, and L. Tjeng, Valence, spin, and orbital state of Co ions in one-dimensional $Ca_3Co_2O_6$: An x-ray absorption and magnetic circular dichroism study, Physical Review B **74**, 245111 (2006).

[20] Z. Hu, H. Wu, M. Haverkort, H. Hsieh, H. Lin, T. Lorenz, J. Baier, A. Reichl, I. Bonn, C. Felser, A. Tanaka, C. Chen, and L. Tjeng, Different Look at the Spin State of Co^{3+} Ions in a CoO_5 Pyramidal Coordination, Physical Review Letters **92**, 207402 (2004).

[21] C. Chang, Z. Hu, H. Wu, T. Burnus, N. Hollmann, M. Benomar, T. Lorenz, A. Tanaka, H.-J. Lin, H. Hsieh, C. Chen, and L. Tjeng, Spin Blockade, Orbital Occupation, and Charge Ordering in $La_{1.5}Sr_{0.5}CoO_4$, Physical Review Letters **102**, 116401 (2009).

[22] S. Csiszar, M. Haverkort, Z. Hu, A. Tanaka, H. Hsieh, H.-J. Lin, C. Chen, T. Hibma, and L. Tjeng, Controlling Orbital Moment and Spin Orientation in CoO Layers by Strain, Physical Review Letters **95**, 187205 (2005).

[23] A. Kushima, S. Yip, and B. Yildiz, Competing strain effects in reactivity of $LaCoO_3$ with oxygen, Physical Review B **82**, 115435 (2010).

[24] K. Gupta and P. Mahadevan, Strain driven magnetism in $LaCoO_3$ thin film, Physical Review B **79**, 020406 (2009).

[25] J. Rondinelli and N. A. Spaldin, Structural effects on the spin-state transition in epitaxially strained $LaCoO_3$ films, Physical Review B **79**, 054409 (2009).

[26] H. Hsu, P. Blaha, and R. Wentzcovitch, Ferromagnetic insulating state in tensile-strained $LaCoO_3$ thin films from LDA + U calculations, Physical Review B **85**, 140404 (2012).

Chapter 5 References

[1] Vankó, György, Jean-Pascal Rueff, Aleksi Mattila, Zoltán Németh, and Abhay Shukla, Temperature- and pressure-induced spin-state transitions in $LaCoO_3$, Physical Review B **73**, 024424 (2006).

[2] Tachibana, Makoto, Takahiro Yoshida, Hitoshi Kawaji, Tooru Atake, and Eiji Takayama-Muromachi, Evolution of electronic states in $RCoO_3$ (R=rare earth): Heat capacity measurements, Physical Review B **77**, 094402 (2008).

[3] Vogt, T., J. A. Hriljac, N.C. Hyatt, and P. Woodward, Pressure induced intermediate to low spin state transition in $LaCoO_3$, Physical Review B **67**, 14041 (2003).

[4] Kozlenko, D., N. Golosova, Z. Jirák, L. Dubrovinsky, B. Savenko, M. Tucker, Y. Le Godec, and V. Glazkov, Temperature- and pressure-driven spin-state transitions in $LaCoO_3$, Physical Review B **75**, 064422 (2007).

[5] J.-S. Zhou, J.-Q. Yan, and J. Goodenough, Bulk modulus anomaly in $RCoO_3$ (R=La, Pr, and Nd), Physical Review B **71**, 220103 (2005).

[6] Fuchs, D., C. Pinta, T. Schwarz, P. Schweiss, P. Nagel, S. Schuppler, R. Schneider, M. Merz, G. Roth, and H. v. Löhneysen, Ferromagnetic order in epitaxially strained $LaCoO_3$ thin films, Physical Review B **75**, 144402 (2007).

[7] D. Fuchs, L. Dieterle, E. Arac, R. Eder, P. Adelmann, V. Eyert, T. Kopp, R. Schneider, D. Gerthsen, and H. v. Löhneysen, Suppression of the ferromagnetic state in $LaCoO_3$ films by rhombohedral distortion, Physical Review B **79**, 024424 (2009).

[8] D. Fuchs, E. Arac, C. Pinta, S. Schuppler, R. Schneider, and H. v. Loehneysen, Tuning the magnetic properties of $LaCoO_3$ thin films by epitaxial strain, Physical Review B **77**, 014434 (2008).

[9] V. V. Mehta, M. Liberati, F. J. Wong, R. V. Chopdekar, E. Arenholz, and Y. Suzuki, Ferromagnetism in tetragonally distorted $LaCoO_3$ thin films," Journal of Applied Physics **105**, 07E503 (2009).

[10] A. D. Rata, A. Herklotz, L. Schultz, and K. Doerr, Lattice structure and magnetization of $LaCoO_3$ thin films, The European Physical Journal B **76**, 215 (2010).

[11] A. Herklotz, A. D. Rata, L. Schultz, and K. Doerr, Reversible strain effect on the magnetization of $LaCoO_3$ films, Physical Review B **79**, 092409 (2009).

[12] J. W. Freeland, J. X. Ma, and J. Shi, Ferromagnetic spin-correlations in strained $LaCoO_3$ thin films, Applied Physics Letters **93**, 212501 (2008).

[13] S. Park, P. Ryan, E. Karapetrova, J. W. Kim, J. X. Ma, J. Shi, J. W. Freeland, and W. Wu, Microscopic evidence of a strain-enhanced ferromagnetic state in $LaCoO_3$ thin films, Applied Physics Letters **95**, 072508 (2009).

[14] H. W. Brinks, H. Fjellvag, A. Kjekshus, and B. C. Hauback, Structure and magnetism of $Pr_{1-x}Sr_xCoO_{3-\delta}$, Journal of Solid State Chemistry **147**, 464 (1999).

[15] M. Paraskevopoulos, J. Hemberger, A. Krimmel, and A. Loidl, Magnetic ordering and spin-state transition in $R_{0.67}Sr_{0.33}CoO_3$, Physical Review B **63**, 224416 (2001).

[16] C. Leighton, D. Stauffer, Q. Huang, Y. Ren, S. El-Khatib, M. Torija, J. Wu, J. Lynn, L. Wang, N. Frey, H. Srikanth, J. Davies, K. Liu, and J. Mitchell, Coupled structural/magnetocrystalline anisotropy transitions in the doped perovskite cobaltite $Pr_{1-x}Sr_xCoO_3$, Physical Review B **79,** 214420 (2009).

[17] V. Mehta and Y. Suzuki, Ferromagnetism enhanced by structural relaxation of biaxially compressed $LaCoO_3$ films, Journal of Applied Physics **109**, 07D717 (2011).

[18] M. Haverkort, Z. Hu, J. Cezar, T. Burnus, H. Hartmann, M. Reuther, C. Zobel, T. Lorenz, A. Tanaka, N. Brookes, H. Hsieh, H.-J. Lin, C. Chen, and L. Tjeng, Spin State Transition in $LaCoO_3$ Studied Using Soft X-ray Absorption Spectroscopy and Magnetic Circular Dichroism, Physical Review Letters **97**, 176405 (2006).

[19] Z. Hu, H. Wu, M. Haverkort, H. Hsieh, H. Lin, T. Lorenz, J. Baier, A. Reichl, I. Bonn, C. Felser, A. Tanaka, C. Chen, and L. Tjeng, Different Look at the Spin State of Co^{3+} Ions in a CoO_5 Pyramidal Coordination, Physical Review Letters **92**, 207402 (2004).

[20] Z. Hu, G. Kaindl, H. Ogasawara, A. Kotani, and I. Felner, Ln-4f/ligand-2p covalence in $BaLnO_3$ and Cs_3LnF_7 (Ln = Ce, Pr, Tb), Chemical Physics Letters **325**, 241 (2000).

[21] J. Herrero-Martin, J. Garcia-Munoz, S. Valencia, C. Frontera, J. Blasco, A. Baron-Gonzalez, G. Subias, R. Abrudan, F. Radu, E. Dudzik, R. Feyerherm, Valence change of Praseodymium in $PrCaCoO_3$ invesitigated by X-ray absorption spectroscopy, Physical Review B **84,** 115131 (2011).

[22] J. B. Goedkoop, B. T. Thole, G. van der Laan, G. A. Sawatzky, F. M. F. de Groot, and J. C. Fuggle, Calculations of magnetic x-ray dichroism in the *3d* absorption spectra of rare-earth compounds, Physical Review B **37**, 2086 (1988).

[23] G. van der Laan, A. Arenholz, Z. Hu, A. Bauer, E. Weschke, Ch. Schuessler-Langeheine, E. Navas, A. Muehlig, G. Kaindl, J. B. Goedkoop, and N. B. Brookes, Magnetic circular dichroism in Tb *3d-4f* resonant photoemission, Physical Review B **59**, 8835 (1999).

[24] Knížek, Karel, Jiří Hejtmánek, Zdeněk Jirák, Petr Tomeš, Paul Henry, and Gilles André, Neutron diffraction and heat capacity studies of $PrCoO_3$ and $NdCoO_3$, Physical Review B **79**, 134103 (2009).

[25] M. Uchida, R. Mahendiran, Y. Tomioka, Y. Matsui, K. Ishizuka, and Y. Tokura, Changes of magnetic domain structure induced by temperature-variation and electron-beam irradiation in $Pr_{0.5}Sr_{0.5}CoO_3$, Applied Physics Letters **86**, 131913 (2005).

[26] S. Hirahara, Y. Nakai, K. Miyoshi, K. Fujiwara, and J. Takeuchi, Magnetic properties, thermal expansion and magnetostriction of $Pr_{0.5}Sr_{0.5}CoO_3$ single crystal, Journal of Magnetism and Magnetic Materials **310**, 1866 (2007).

[27] I. O. Troyanchuk, D. V. Karpinskiĭ, A. N. Chobot, D. G. Voĭitsekhovich, and V. M. Dobryanskiĭ, Phase transformations in $Pr_{1-x}Sr_xCoO_3$, JETP Letters **84**, 151 (2006).

[28] Y. Wang, and B. Cooper, Collective Excitations and Magnetic ordering in materials with singlet crystal-field ground state, Physical Review **172**, 539 (1968).

[29] J. D. Gordon, R. M. Hornreich, S. Shtrikman, and B. M. Wanklyn, Magnetization studies in the rare-earth orthochromites. V. $TbCrO_3$ and $PrCrO_3$, Physical Review B **13**, 3012 (1976).

[30] A. A. Mukhin, V. Yu, V. D. Travkin, A. M. Balhashov, Magnetic anisotropy and ground state of the rare-earth ions in $PrMnO_3$ and $NdMnO_3$, Journal of Magnetism and Magnetic Materials **226-230**, 1139 (2001).

[31] X. Wang, S. Cao, Y. Wang, S. Yuan, B. Kang, A. Wu, and J. Zhang, Crystal growth and characterization of the rare earth orthoferrite $PrFeO_3$, Journal of Crystal Growth, Jan. (2012). (*in press*) DOI:10.1016/j.jcrysgro.2011.12.096